

Advances in Integrated Circuits and Systems for Wearable Biomedical Electrical Impedance Tomography

by

Yu Wu

26 July 2019

A thesis submitted to University College London for
the degree of Doctor of Philosophy



Department of Electrical and Electronic Engineering
University College London

Declaration

I, Yu Wu confirm that the work presented in this thesis is my own. Where information has been derived from other sources, I confirm that this has been indicated in the thesis.

Abstract

Electrical impedance tomography (EIT) is an impedance mapping technique that can be used to image the inner impedance distribution of the subject under test. It is non-invasive, inexpensive and radiation-free, while at the same time it can facilitate long-term and real-time dynamic monitoring. Thus, EIT lends itself particularly well to the development of a bio-signal monitoring/imaging system in the form of wearable technology.

This work focuses on EIT system hardware advancement using complementary metal oxide semiconductor (CMOS) technology. It presents the design and testing of application specific integrated circuit (ASIC) and their successful use in two bio-medical applications, namely, neonatal lung function monitoring and human-machine interface (HMI) for prosthetic hand control.

Each year fifteen million babies are born prematurely, and up to 30% suffer from lung disease. Although respiratory support, especially mechanical ventilation, can improve their survival, it also can cause injury to their vulnerable lungs resulting in severe and chronic pulmonary morbidity lasting into adulthood, thus an integrated wearable EIT system for neonatal lung function monitoring is urgently needed.

In this work, two wearable belt systems are presented. The first belt features a miniaturized active electrode module built around an analog front-end ASIC which is fabricated with 0.35- μm high-voltage process technology with $\pm 9\text{ V}$ power supplies and occupies a total die area of 3.9 mm^2 . The ASIC offers a high power active current driver capable of up to $6\text{ mA}_{\text{p-p}}$ output, and wideband active buffer for EIT recording as well as contact impedance monitoring. The belt has a bandwidth of 500 kHz, and an image frame rate of 107 frame/s. To further improve the system, the active electrode module

is integrated into one ASIC. It contains a fully differential current driver, a current feedback instrumentation amplifier (IA), a digital controller and multiplexors with a total die area of 9.6 mm^2 . Compared to the conventional active electrode architecture employed in the first EIT belt, the second belt features a new architecture. It allows programmable flexible electrode current drive and voltage sense patterns under simple digital control. It has intimate connections to the electrodes for the current drive and to the IA for direct differential voltage measurement providing superior common-mode rejection ratio (CMRR) up to 74 dB, and with active gain, the noise level can be reduced by a factor of $\sqrt{3}$ using the adjacent scan. The second belt has a wider operating bandwidth of 1 MHz and multi-frequency operation. The image frame rate is 122 frame/s, the fastest wearable EIT reported to date. It measures impedance with 98% accuracy and has less than 0.5Ω and 1° variation across all channels. In addition the ASIC facilitates several other functionalities to provide supplementary clinical information at the bedside.

With the advancement of technology and the ever-increasing fusion of computer and machine into daily life, a seamless HMI system that can recognize hand gestures and motions and allow the control of robotic machines or prostheses to perform dexterous tasks, is a target of research. Originally developed as an imaging technique, EIT can be used with a machine learning technique to track bones and muscles movement towards understanding the human user's intentions and ultimately controlling prosthetic hand applications.

For this application, an analog front-end ASIC is designed using $0.35\text{-}\mu\text{m}$ standard process technology with $\pm 1.65 \text{ V}$ power supplies. It comprises a current driver capable of differential drive and a low noise ($9\mu\text{V}_{rms}$) IA with a CMRR of 80 dB. The function modules occupy an area of 0.07 mm^2 . Using the ASIC, a complete HMI system based on the EIT principle for hand prosthesis control has been presented, and the user's forearm inner bio-impedance redistribution is assessed. Using artificial neural networks, bio-impedance redistribution can be learned so as to recognise the user's

intention in real-time for prosthesis operation. In this work, eleven hand motions are designed for prosthesis operation. Experiments with five subjects show that the system can achieve an overall recognition accuracy of 95.8%.

Impact Statement

The author considers that the research work presented in this thesis has made the following contributions and impact to the field of electrical impedance tomography (EIT) for bio-medical applications:

- Advancement of wearable EIT technology for bio-medical applications is demonstrated through several integrated, wide bandwidth, multi-functional prototypes using application specific integrated circuit (ASIC).
- An innovative active electrode EIT system architecture using active instrumentation amplifiers and summation topology has been proposed. Compared to the conventional active buffer topology, the system has the advantage of offering a higher common mode rejection ratio and better noise performance.
- With the developed EIT based human-machine interface device, the potential of using EIT for hand prosthesis control is evaluated. The merit of EIT for this application compared to existing methods is analysed, and possible future research direction is proposed for this emerging EIT application.

In addition to the research value of this work, other impacts are:

- Exploration of EIT technology in conjunction with multi-disciplinary research areas towards a clinical testable prototype and extension of the EIT technology readiness level by not only considering circuit innovation, but also taking into account the clinical needs in the design and making the prototype more compatible with clinical application.
- Presentation of the research outcomes in the form of prototype demonstrations and showcasing the prototypes in real action at conferences to raise the awareness of the practicality of EIT technology in different applications.

Acknowledgements

First and foremost, I would like to take this opportunity to express my deepest appreciation to Prof. Andreas Demosthenous for welcoming me into his group and trusting me to take on important roles in various exciting projects. Working with Andreas has been an outstanding journey. His extensive knowledge and expertise, as well as his spirit of pursuing innovations in the art of IC design not only helped, but encouraged, and motivated me constantly during the course of my Ph.D., and I could have achieved little without his guidance and support. Secondly, I would also like to express my sincere gratitude to Prof. Richard Bayford for offering his in-depth knowledge in electrical impedance tomography which inspired me and helped me to bring the technology and innovation closer to applications. It is truly an honour to have worked with and learn from both of them and I could not thank them enough for assisting me throughout this venture.

A special mention must go to Mr Peter Langlois for his countless detail-oriented help and guidance during this journey. Peter has my deep admirations for his dedications and rigorousness in science and his selfless devotion in helping the young researchers.

Last but not least, I would like to thank my senior colleague and close friend Dr Dai Jiang, who I received tremendous help from in both work and life. It is very fortunate to have him, a kind, patient, and knowledgeable senior figure in the group. I would also like to extend my thanks to my other colleagues and friends who kindly offered their suggestions and support whenever I needed. It is a pleasure to have this opportunity to work in the UCL-Abe group with all those very experienced IC designers, brilliant mind and the friendly environment we have created.

I would also like to acknowledge financial support for my Ph.D. through the CRADL project. It has been an amazing experience to have had the opportunity and privilege to work on CRADL and interact with clinicians, academics and industrial partners in Europe.

And most of all, I want to say thank you to my parents for their unconditional support care and love, and to my wife Tian who has been there with me every step of the way. No amount of words can describe the love I have for you and Thank You for everything.

Table of Contents

ABSTRACT	1
IMPACT STATEMENT	4
ACKNOWLEDGEMENTS	5
TABLE OF CONTENTS	7
LIST OF FIGURES	11
LIST OF TABLES	18
ABBREVIATIONS	19
CHAPTER 1 INTRODUCTION	21
1.1 MOTIVATION.....	21
1.1.1 <i>Thorax application with special needs – Neonate lung monitoring</i>	22
1.1.2 <i>A promising application emerging – EIT for human-machine interfaces</i>	25
1.2 AIM AND OBJECTIVES	27
1.3 THESIS OVERVIEW	28
1.4 LIST OF PUBLICATIONS.....	29
CHAPTER 2 AN OVERVIEW OF EIT	31
2.1 INTRODUCTION	31
2.2 BASIC OF EIT OPERATION.....	31
2.3 STUDY OF EIT HARDWARE SPECIFICATION.....	36
2.3.1 <i>Fundamentals in bio-impedance measurement (BIM)</i>	36
2.3.1.1 Introduction to bio-impedance	36
2.3.1.2 BIM techniques and electrode interfaces.....	38

2.3.1.3	Safety	44
2.3.2	<i>EIT analog-front-end</i>	45
2.3.2.1	Current injection in EIT	45
2.3.2.2	Voltage measurement in EIT	48
2.3.3	<i>EIT system architecture</i>	53
2.3.3.1	Passive vs active architecture	54
2.3.3.2	Serial vs parallel architecture	56
2.3.3.3	Other useful system functionalities for thorax EIT	57
2.4	SYSTEMS FOR BIOMEDICAL EIT - A REVIEW	59
2.4.1	<i>Passive EIT system for thorax EIT</i>	59
2.4.2	<i>Active EIT systems for thorax EIT</i>	62
2.4.3	<i>EIT in human-machine interface</i>	67
2.4.4	<i>Summary</i>	68
2.5	CONCLUSION	72
CHAPTER 3 ACTIVE ELECTRODE BASED EIT SYSTEM FOR LUNG RESPIRATION MONITORING		73
3.1	INTRODUCTION	73
3.2	SYSTEM DESIGN AND IMPLEMENTATION	74
3.2.1	<i>System architecture and design</i>	74
3.2.2	<i>Digital controls and signal processing¹</i>	77
3.2.2.1	Active electrode control	77
3.2.2.2	Control and signal processing in the central hub	79
3.3	ACTIVE ELECTRODE ASIC	81
3.3.1	<i>Current stimulation</i>	81
3.3.2	<i>Voltage acquisition and heart-rate recording</i>	92
3.3.3	<i>Multi-parameter sensor buffer</i>	96
3.4	MEASURED RESULTS	97

3.4.1	<i>Active electrode ASIC</i>	97
3.4.2	<i>EIT system evaluation</i>	100
3.5	SUMMARY	108
CHAPTER 4 TOWARDS THE NEXT GENERATION OF ACTIVE EIT SYSTEM		109
4.1	INTRODUCTION	109
4.2	SYSTEM DESIGN AND IMPLEMENTATION	110
4.2.1	<i>Proposed active electrode architecture</i>	110
4.2.2	<i>Central hub of EIT system¹</i>	113
4.3	ACTIVE ELECTRODE ASIC	115
4.3.1	<i>EIT current stimulation</i>	115
4.3.2	<i>EIT voltage acquisition</i>	116
4.3.3	<i>Heart rate recording and shape sensing</i>	118
4.4	MEASURED RESULTS	120
4.4.1	<i>Active electrode ASIC</i>	120
4.4.2	<i>System performance test</i>	120
4.4.3	<i>Boundary shape tracking</i>	127
4.4.4	<i>System in-vivo validation</i>	128
4.4.5	<i>Comparison with other work</i>	129
4.5	SUMMARY	131
CHAPTER 5 EIT FOR PROSTHESIS HAND CONTROL		132
5.1	INTRODUCTION	132
5.2	SYSTEM DESIGN AND IMPLEMENTATION	133
5.2.1	<i>System architecture</i>	133
5.2.2	<i>Analog front-end ASIC</i>	136
5.2.3	<i>Digital controls and I-Q demodulation¹</i>	138
5.2.4	<i>Hand prosthesis motion control</i>	139
5.3	MEASURED RESULTS	143

5.3.1	<i>Analog front-end ASIC</i>	143
5.3.2	<i>System testing and results</i>	145
5.3.3	<i>Preliminary medium-term performance</i>	151
5.3.4	<i>Discussion</i>	155
5.4	SUMMARY	157
CHAPTER 6 CONCLUSION AND FUTURE WORK		159
6.1	CONCLUSION	159
6.2	NOVEL CMOS CIRCUITS FOR FUTURE EIT SYSTEMS	161
6.2.1	<i>Power-efficient EIT current driver with PWMs</i>	161
6.2.1.1	Motivation	161
6.2.1.2	Circuit design	162
6.2.1.3	Simulation results	165
6.2.2	<i>Concept on novel demodulation approaches using time-stamps</i>	166
BIBLIOGRAPHY		169

List of Figures

FIGURE 1.1: VISION OF A WEARABLE MULTI-VITAL SIGN MONITORING EIT SYSTEM FOR NEONATAL APPLICATION.	23
FIGURE 1.2: CROSS-SECTION OF THE FOREARM WITH ELECTRODES PLACED FOR EIT.	26
FIGURE 2.1: A SIMPLIFIED EIT CONCEPT ILLUSTRATION (A) TOP VIEW OF THE MODEL WITH A CONSTANT CURRENT INJECTION. (B) THE SAME MODEL WITH CONDUCTIVE CYLINDER IMMersed. (C) THE SAME MODEL WITH INSULATIVE CYLINDER IMMersed, THE COLOUR BAR INDICATES NORMALIZED ELECTRICAL POTENTIAL.	32
FIGURE 2.2: A TYPICAL EIT ADJACENT ROTATION SCAN ILLUSTRATION WITH AN ARRAY OF 8 ELECTRODES.	33
FIGURE 2.3: THE OVERALL OPERATION FLOW OF EIT - FROM MEASUREMENT TO IMAGE.	35
FIGURE 2.4: THE STRUCTURE OF A CELL AND ITS CORRESPONDING FRICKE EQUIVALENT CIRCUIT. RE: EXTRACELLULAR RESISTANCE, RM: MEMBRANE RESISTANCE AND CM: MEMBRANE CAPACITANCE, AND RI: INTRACELLULAR RESISTANCE.	36
FIGURE 2.5: TISSUE CONDUCTIVITY AND RELATIVE PERMITTIVITY WITH RESPECT TO FREQUENCY [34].	37
FIGURE 2.6: ELECTRICAL MODEL FOR ELECTRODE-TO-SKIN INTERFACE. LEFT, GEL ELECTRODE, AND RIGHT, SIMPLIFIED MODEL FROM [37].	38
FIGURE 2.7: BIO-IMPEDANCE MEASUREMENT TECHNIQUE (A) TWO-ELECTRODE (B) FOUR-ELECTRODE.	39
FIGURE 2.8: MEASURED ELECTRODE CONTACT IMPEDANCE REPORTED IN [38].	40
FIGURE 2.9: I-Q DEMODULATION FOR BIO-IMPEDANCE MEASUREMENT.	41
FIGURE 2.10: MAGNITUDE AND PHASE DEMODULATION FOR BIO-IMPEDANCE MEASUREMENT.	43
FIGURE 2.11: THE EQUIVALENT MODEL FOR THE CURRENT DRIVER (A) WITH RESISTIVE LOAD (B) WITH IMPEDANCE CL, RL LOAD AND PARASITIC CAPACITANCE CP.	46

FIGURE 2.12: (A) SINGLE-ENDED CURRENT DRIVE; (B) FULLY DIFFERENTIAL DRIVE.	47
FIGURE 2.13: (A) GENERATION OF AN EIT DIFFERENTIAL IMAGE USING A PHYSICAL PHANTOM (B) EIT RESISTIVE PHANTOM [50] USED FOR EVOLUTION. RESISTIVE ELEMENT ⑤=100 Ω , ④=196 Ω , ③ =63.4 Ω , ②=6.34 Ω , ①=68.1 Ω	49
FIGURE 2.14: VOLTAGE DISTRIBUTION MEASURED FROM THE RESISTIVE PHANTOM USING IDEAL COMPONENTS WITH 8, 16 AND 32 ELECTRODE CONFIGURATIONS EXCLUDING VOLTAGES ON INJECTION ELECTRODES. THE DIFFERENTIAL VOLTAGE PAIR POSITION OPPOSITE THE INJECTION PAIR IS MARKED AS POSITION ZERO FOR PLOTTING PURPOSES.....	50
FIGURE 2.15: COMPARISON OF AMPLITUDE OF THE CM (COMMON-MODE) VOLTAGE AT DIFFERENT ELECTRODE RECORDING POSITIONS WHEN APPLYING SINGLE-ENDED AND DIFFERENTIAL CURRENT DRIVE METHODS WITH THE DM (DIFFERENTIAL-MODE) VOLTAGE OUTPUTS.	51
FIGURE 2.16: PASSIVE 8 ELECTRODE EIT SYSTEM ARCHITECTURE.	54
FIGURE 2.17: DIFFERENCE BETWEEN ACTIVE AND PASSIVE EIT SYSTEMS, Z_e IS THE CONTACT ELECTRODE IMPEDANCE, AND C_p IS THE CABLE PARASITIC CAPACITANCE WITH SHIELDING AND C_s IS THE FPC TRACK PARASITIC CAPACITANCE WITHOUT SHIELDING, C_{mux} IS THE SWITCH PARASITIC CAPACITANCE.	55
FIGURE 2.18: EIT SYSTEM ARCHITECTURE WITH PARALLEL VOLTAGE ACQUISITION.	57
FIGURE 2.19: RECONSTRUCTED EIT IMAGES USING THE SAME SET OF DATA BUT DIFFERENT BOUNDARY CONDITIONS TO ILLUSTRATE THAT AN ACCURATE TORSO SHAPE MODEL CAN SIGNIFICANTLY IMPROVE THE QUALITY OF LUNG EIT IMAGES [69].	59
FIGURE 2.20: (A) EIT SYSTEM KHU MARK-2 (B) SIMPLIFIED CIRCUIT SYSTEM IMPLEMENTATION [70].	60
FIGURE 2.21: HOWLAND CURRENT DRIVER.	60
FIGURE 2.22: (A) THE DRÄGER SYSTEM [74] (B) APPLY PASSIVE EIT SYSTEM IN CLINICAL NEONATAL THORAX APPLICATION [76].	62
FIGURE 2.23: (A) ACTIVE ELECTRODE ON THE WEARABLE BELT. (B) THE ACTIVE ELECTRODE SYSTEM ARCHITECTURE [67].	62
FIGURE 2.24: (A) ACTIVE BELT ASSEMBLY (B) ASIC SYSTEM ON CHIP ARCHITECTURE [79].	64

FIGURE 2.25: THE SWISSTOM BB ² SYSTEM [13].	64
FIGURE 2.26: KHU MULTI-FUNCTIONAL WEARABLE EIT DEVICE [80].	65
FIGURE 2.27 COOPERATIVE SENSORS FOR EIT WITH FREQUENCY DIVISION [81].	66
FIGURE 2.28: A WEARABLE EIT FOR HAND GESTURE RECOGNITION IN [23].	67
FIGURE 3.1: WEARABLE EIT LUNG RESPIRATION MONITORING SYSTEM WITH HEART RATE MONITORING AND OTHER FUNCTIONS USING ACTIVE ELECTRODE ASIC.	74
FIGURE 3.2: ACTIVE ELECTRODE BELT SYSTEM ARCHITECTURE. B1 IS THE MAIN BUFFER, B2 IS THE SENSOR BUFFER AND CD IS THE CURRENT DRIVER IN THE ASIC. ALL ELECTRODES SHARE COLOURED ANALOG PATHS, AND ARE CONTROLLED BY THE DIGITAL CPLD.	76
FIGURE 3.3: CONTROL LOGIC FOR ELECTRODE SELECTION.	78
FIGURE 3.4: CONTROL FLOW OF CALCULATING VECTORS V_I AND V_Q .	79
FIGURE 3.5: (A) THE PROPOSED CURRENT DRIVER TOPOLOGY, (B) THE SMALL-SIGNAL ANALYSIS CIRCUIT FOR THE CURRENT DRIVER.	81
FIGURE 3.6: 3D MESH FOR THE CURRENT DRIVER TRANSCONDUCTANCE PARAMETER SETTING AT 1MHZ OPERATING FREQUENCY.	83
FIGURE 3.7: 3D MESH FOR THE CURRENT DRIVER OUTPUT IMPEDANCE PARAMETER SETTING AT 1MHZ OPERATING FREQUENCY.	84
FIGURE 3.8: DETAILED TRANSISTOR-LEVEL SCHEMATIC OF THE CURRENT DRIVER (CD).	85
FIGURE 3.9: THE OPEN-LOOP GAIN AND PHASE RESPONSE OF THE DDTA.	88
FIGURE 3.10: THE SIMULATED TRANSCONDUCTANCE AND OUTPUT IMPEDANCE OF THE CURRENT DRIVER.	89
FIGURE 3.11: (A) CURRENT DRIVER WITHOUT CONSIDER ΔI MISMATCHED CURRENT FLOWING THROUGH THE LOAD Z_o ; (B) CURRENT DRIVER MISMATCH ΔI GENERATING COMMON-MODE SIGNALS.	90
FIGURE 3.12: COMPLETE CURRENT DRIVER TOPOLOGY IN THE EIT SYSTEM.	91
FIGURE 3.13: PROPOSED EIT VOLTAGE SIGNAL RECORDING WITH ACTIVE ELECTRODES.	93
FIGURE 3.14: MAIN BUFFER B1: (A) WORKING PRINCIPLE AND (B) TRANSISTOR-LEVEL CIRCUIT.	94

FIGURE 3.15: SIMULATED AC RESPONSE FOR THE MAIN BUFFER B1, FRONT-END OTA IN OPEN-LOOP, AND THE ERROR-AMPLIFIER OUTPUT STAGE.	95
FIGURE 3.16: ACTIVE ELECTRODE ASIC MICROGRAPH.	97
FIGURE 3.17: MEASURED TRANSCONDUCTANCE OF THE CURRENT DRIVER ACROSS EIGHT CHIP SAMPLES. THE AVERAGE VALUE IS 1.99 mA/V WITH A STANDARD DEVIATION OF 10.3 μ A/V.	98
FIGURE 3.18: CURRENT DRIVER OUTPUT IMPEDANCE MEASUREMENT CIRCUIT EQUIVALENT MODEL.	99
FIGURE 3.19: MEASURED MEAN OUTPUT IMPEDANCE OF THE CURRENT DRIVER.	100
FIGURE 3.20: (A) SYSTEM CALIBRATED MEASUREMENT RESULTS; (B) IMAGE FRAME RATE CAPTURE ON THE OSCILLOSCOPE; (C) RESISTIVE-MESH PHANTOM TEST RESULTS IN FORM OF EIT IMAGES, THE COLOUR BAR SHOWS NORMALIZED CONDUCTANCE; (D) IMPEDANCE VARIATION PLOTTED USING DATA FROM RESISTIVE-MESH PHANTOM TEST COMPARED TO THE IDEA VARIATION.	101
FIGURE 3.21: DETAILED ACTIVE EIT BELT LAYER-STACKING AND CROSS-SECTION VIEW.	104
FIGURE 3.22: EIT IN-VIVO TEST WITH THE BELT WORN BY A HEALTHY MALE VOLUNTEER; (A) THE EXHALATION AND INHALATION LUNG IMAGES WHERE THE COLOUR BAR SHOWS NORMALIZED CONDUCTANCE; (B) ECG SIGNALS CAPTURED IN 30 S SWITCHING BETWEEN THREE DIFFERENT LOCATIONS USING THE EIT SYSTEM.	105
FIGURE 4.1: PROPOSED ACTIVE ELECTRODE EIT BELT ARCHITECTURE WITH ACTIVE CURRENT DRIVER, IA AND MEMS SHAPE SENSORS.	111
FIGURE 4.2: NOISE ANALYSIS OF THE TWO ACTIVE EIT SYSTEM TOPOLOGIES (A) ACTIVE BUFFER TOPOLOGY AND (B) ACTIVE IA SUM TOPOLOGY.	113
FIGURE 4.3: INJECTION CONTROL LOGIC IN THE ACTIVE ELECTRODE (AE).	114
FIGURE 4.4: THE FULLY DIFFERENTIAL CURRENT DRIVER IMPLEMENTED IN THE ASIC DRIVING A LOAD R _L	115
FIGURE 4.5: CURRENT FEEDBACK INSTRUMENTATION AMPLIFIER CMOS LEVEL IMPLEMENTATION.	117
FIGURE 4.6: (A) BOUNDARY SHAPE DETECTION FOR EIT MODEL SELECTION USING MEMS (B) ECG MEASUREMENT FOR HEART-RATE MONITORING.	119
FIGURE 4.7: ACTIVE ELECTRODE ASIC MICROGRAPH.	120

FIGURE 4.8: SYSTEM IMPEDANCE MEASUREMENT ACCURACY WHERE THE SOLID BLACK LINES ARE THE MEASURED VALUES AND BLUE DOTTED LINES ARE IDEAL VALUES.....	121
FIGURE 4.9: SIMPLIFIED EIT MODEL WITH BOTH CURRENT DRIVE AND VOLTAGE RECORDING FOR AN EIGHT-ELECTRODE SYSTEM.	122
FIGURE 4.10: COMPARISON OF IMAGES THAT IS PRODUCED BETWEEN THREE DIFFERENT 8-ELECTORDE BASED EIT SYSTEMS TO AN IDEAL EIT IMAGE BY SIMULATION; (A) IDEAL EIT IMAGE, (B) PASSIVE EIT (C) ACTIVE BUFFER EIT SYSTEM (D) PROPOSED ACTIVE IA EIT SYSTEM, THE COLOUR BAR SHOWS NORMALIZED CONDUCTANCE.	123
FIGURE 4.11: THE 16 ELECTRODE SYSTEM PHANTOM IMAGE RESULTS AT ONLY 125 KHZ; THE TOP PHANTOM HAS TWO RESISTIVE ELEMENTS RL AND RR AT DIAGONAL POSITIONS. THE BOTTOM PHANTOM HAS ONE RESISTIVE ELEMENT RL AND AN R-C IMPEDANCE LOAD ZR AT DIAGONAL POSITIONS. THE COLOUR BAR SHOWS NORMALIZED CONDUCTANCE.	125
FIGURE 4.12: THE 16 ELECTRODE SYSTEM PHANTOM IMAGE RESULTS AT 250 KHZ, 500 KHZ AND 1 MHZ TO DISTINGUISH BETWEEN ZR AND RR , THE COLOUR BAR SHOWS NORMALIZED CONDUCTANCE.....	126
FIGURE 4.13: SHAPE MEASUREMENT (A) THE BELT IS WRAPPED ON THE CONTOUR (B) CIRCLE SHAPE (C) OVAL SHAPE (D) TORSO-LIKE SHAPE RECONSTRUCTED IN COMPARISON WITH THE SCANNED REFERENCE WHERE THE BLACK LINES ARE THE REFERENCE CONTOURS AND BLUE LINES ARE THE RECONSTRUCTED SHAPE.	127
FIGURE 4.14: THE IN-VIVO MEASUREMENT RESULTS (A) RECONSTRUCTED EIT LUNG IMAGES, THE COLOUR BAR SHOWS NORMALIZED CONDUCTANCE. (B) THE BREATHING CYCLE CORRESPONDING TO THE EIT IMAGES.....	128
FIGURE 4.15: THE ECG MEASUREMENT RESULTS FOR HEART-RATE MONITORING.....	128
FIGURE 5.1: PROPOSED EIT BASED HAND PROSTHESIS CONTROL SYSTEM WITH ASIC.	132
FIGURE 5.2: OVERALL HMI SYSTEM ARCHITECTURE.....	135
FIGURE 5.3: TRANSISTOR-LEVEL SCHEMATIC OF THE CURRENT DRIVER.	137
FIGURE 5.4: STATE MACHINE FOR CONTROLLING THE EIT OPERATION.	138

FIGURE 5.5: HAND PROSTHESIS CONTROL WITH TWO SUB-CONTROL GROUPS WITH GESTURE ENABLED SWITCHING METHOD.	139
FIGURE 5.6: SYSTEM CONTROL FLOW CHART FOR TRAINING AND PROSTHESIS OPERATION.	140
FIGURE 5.7: ASIC MICROGRAPH WITH INDIVIDUAL BLOCKS LABELLED AND THE COMPLETE EIT READER WITH THE ASIC MOUNTED ON A DAUGHTER BOARD AND A FPGA STACKED ON TOP OF THE MOTHERBOARD.	143
FIGURE 5.8: MEASURED COMMON-MODE AND DIFFERENTIAL-MODE GAINS OF THE IA.	144
FIGURE 5.9: MEASURED TRANSCONDUCTANCE AND BANDWIDTH OF THE CURRENT DRIVER WITH A 1 k Ω LOAD.	144
FIGURE 5.10: ALL GESTURES THAT HAS CORRESPONDING PROSTHESIS MOTIONS; AND 50 DATASETS OF 40 MEASURED IMPEDANCE COMBINATIONS PLOTTED. USING THE AVERAGE OF 50 DATASETS, A CORRESPONDING EIT IMAGE IS PRODUCED, THE COLOUR BAR SHOWS NORMALIZED CONDUCTANCE.....	147
FIGURE 5.11: CONFUSION MATRIXES FOR THE THREE GESTURE GROUPS.....	148
FIGURE 5.12: SINGLE-USER MULTI-SESSION ACCURACY TEST RESULTS.	152
FIGURE 5.13: MULTI-USER ACCURACY REPRODUCIBILITY TEST RESULTS.....	152
FIGURE 5.14: ADVANTAGES OF EIT AS AN ALTERNATIVE HMI METHOD FOR HAND PROSTHESIS CONTROL IN TERMS OF: (A) SIGNAL BANDWIDTH AND STRENGTH; (B) DIFFERENT MEASUREMENT SEQUENCES.	155
FIGURE 6.1: CONVENTIONAL H-BRIDGE BASED CURRENT GENERATOR WITH CURRENT MIRROR DAC.	161
FIGURE 6.2: CIRCUIT IMPLEMENTATION OF THE PROPOSED CURRENT GENERATOR.	162
FIGURE 6.3: SPECTRA OF 98 kHz PSEUDO SINEWAVE (UPPER ROW), SPWM WAVE (MIDDLE ROW) AND 50% DUTY CYCLE SQUARE WAVE (LOWER ROW), AND THEIR RESPECTIVE SPECTRA AFTER A 300 kHz SECOND-ORDER LOWPASS BUTTERWORTH FILTER.	164
FIGURE 6.4: LAYOUT OF THE CURRENT GENERATOR.....	165
FIGURE 6.5: THE PWM SINE CURRENT OUTPUT AND VOLTAGE ACROSS A RESISTIVE LOAD FURTHER FILTERED BY A FIRST-ORDER (RED) AND SECOND-ORDER (GREEN) LOW-PASS FILTERS.	166

FIGURE 6.6: TIME STAMP DEMODULATION METHOD CONCEPT.....	167
---	-----

List of Tables

TABLE 2-1: SUMMARY OF THE MAJOR EIT SYSTEMS REPORTED IN THE LITERATURE WITH SYSTEMS SPECIFICATION PROPOSED IN THIS WORK. 70

TABLE 2-2: SPECIFICATION FOR THE CURRENT INJECTION. 71

TABLE 2-3: SPECIFICATION FOR THE VOLTAGE ACQUISITION. 71

TABLE 3-1: ASIC MEASURED PERFORMANCE. 100

TABLE 3-2: COMPARISON WITH OTHER WORK. 107

TABLE 4-1: ASIC MEASURED PERFORMANCE. 125

TABLE 4-2: COMPARISON WITH OTHER WORK. 130

TABLE 5-1: ASIC MEASURED PERFORMANCE. 145

TABLE 5-2: COMPARISON WITH OTHER WORK. 150

TABLE 5-3: DETAILS OF TRAINING METHODS. 151

TABLE 5-4: COMPARISON OF MACHINE LEARNING ALGORITHMS. 154

Abbreviations

A_{ol}	Open-loop gain
ADC	Analog to digital convertor
ANN	Artificial neural network
ASIC	Application-specific integrated circuit
BIM	Bio-impedance measurement
CM	Common-mode
CMFB	Common-mode feedback
CMOS	Complementary metal oxide semiconductor
CMRR	Common-mode reject ratio
CT	Computed tomography
DAC	Digital to analog convertor
DDS	Direct digital synthesis
DDTA	Differential difference transconductance amplifier
DM	Differential-mode
DSP	Digital signal processing
ECG	Electrocardiogram
EIT	Electrical impedance tomography
FEM	Finite element model
FPC	Flexible printed circuit board
FPGA	Field-programmable gate array
FPS	Frames per second
HMI	Human-machine interface
IA	Instrumentation amplifier
IMM	Impedance measurement module
KNN	K-nearest neighbors

LPF	Low-pass filter
LPV	Lung protective ventilation
LUT	Look-up table
MACs	Multiplier accumulators
MRI	Magnetic resonance imaging
Opamp	Operational amplifier
OTA	Operational transconductance amplifier
PGA	Programmable gain amplifier
PCB	Printed circuit board
PWM	Pulse width modulation
sEMG	Surface electromyography
SFDR	Spurious-free dynamic range
SNR	Signal-to-noise ratio
SoC	System-on-chip
SpO ₂	Peripheral capillary oxygen saturation
SPWM	Sine pulse width modulation
SUT	Subject under test
SVM	Support vector machine
THD	Total harmonic distortion
VCCS	Voltage-controlled current source

Chapter 1

Introduction

1.1 Motivation

Electrical impedance tomography (EIT) is an impedance mapping technique that can be used to image the inner impedance distribution of the subject under test (SUT). Such a system uses an array of electrodes that are presented to the SUT to inject a known alternating current while measuring the resulting potentials developed on the same or other electrodes. The recorded potentials reflect the electrical properties of the SUT which can be used to map an inner impedance distribution image which permits the estimation and analysis of the inner conductivity (resistivity) distribution, or re-distribution that is occurring in the SUT. Ever since the feasibility of EIT was first reported for biological SUT in the 1980s by Barber and Brown [1], this technique has been intensively researched towards a non-invasive imaging technique for biomedical applications. As different biological tissues have different electrical properties, whose electrical properties vary due to physiological or pathological reasons [2], EIT can be used to evaluate tissue bio-impedance variations that could aid clinical evaluation. After years of research and development, EIT has proven its feasibility and potential in a number of biomedical applications including brain, breast, abdominal and prostate imaging.

This work focuses on EIT system hardware advancement using complementary metal oxide semiconductor (CMOS) technology and presents the design and testing of several application specific integrated circuits (ASICs) and their successful use in

two biomedical applications, namely, neonatal lung function monitoring and human-machine interface (HMI) for prosthetic hand control.

1.1.1 Thorax application with special needs – Neonate lung monitoring

Patients in respiratory failure often require mechanical ventilation. However, this life-saving therapy can impose other health risks to patients. Since 1995, because of better awareness of the risks, significant research has been done on ventilator-induced or associated lung injury with mechanical ventilation, and as a result lung protective ventilation (LPV) strategies have been proposed [3]. The LPV strategies call for patient specific ventilation parameter settings such as tidal volume and respiratory rate. These strategies encourage new tools for lung regional behaviour monitoring to better guide the ventilation parameters settings. During respiration, large volumes of conductivity re-distribution occur physiologically due to air flows. The use of thorax EIT can offer a non-invasive continuous image of pulmonary impedance that indicates lung behaviour during, for example, mechanical ventilation. As a result, thorax EIT is doubtless the most prominent EIT biomedical application.

Compared to adult patients, the situation is more severe for pre-term neonates. Each year fifteen million babies are born prematurely, and up to 30% suffer from lung disease [4], [5]. Although respiratory support, especially mechanical ventilation, can improve their survival, it also can cause injury to their vulnerable lungs resulting in severe and chronic pulmonary morbidity lasting into adulthood [6]. Heterogeneity of lung aeration, resulting in areas of lung over inflation and lung collapse, plays a crucial part in the risk of mortality and morbidity due to respiratory failure.

EIT is non-invasive and compared with conventional imaging techniques such as X-ray and magnetic resonance imaging (MRI), it is inexpensive and radiation-free, while at the same time it can facilitate long-term and real-time dynamic monitoring of lung aeration without the need of co-operation from the patient. EIT lends itself particularly well to the development of a neonatal lung function monitoring/imaging

system in the form of wearable technology (e.g., wearable belt) that could be used at the bedside. Driven by the promising future of neonatal thorax EIT, clinical uses of EIT for lung aeration and ventilation monitoring on neonatal and paediatric patients have been frequently reported with positive results [7]. Many potential clinical applications of neonatal thorax EIT are highlighted in [8] such as detecting end-expiratory lung volumes as the indication for lung disease progression, studying neonatal breathing patterns and detecting adverse events.

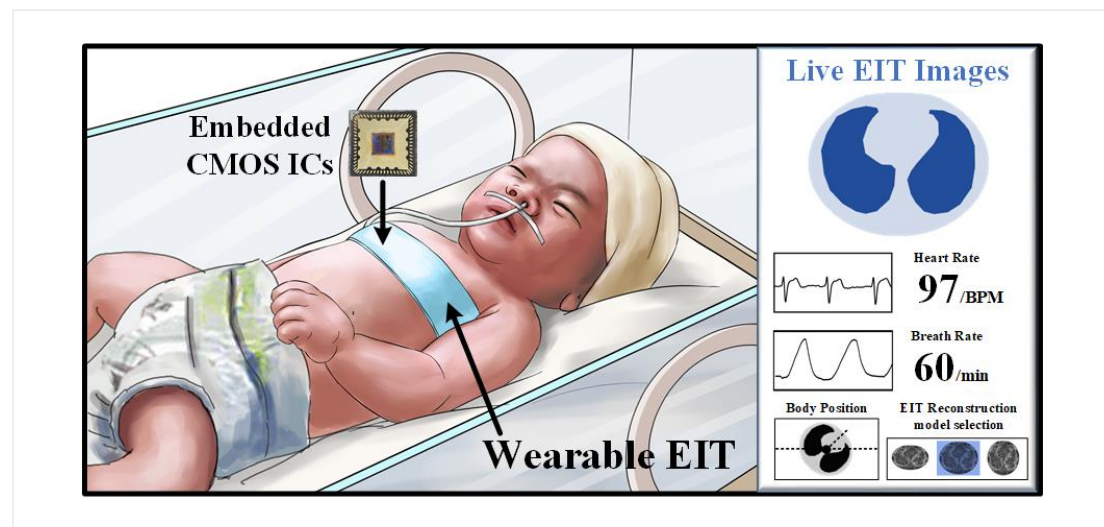


Figure 1.1: Vision of a wearable multi-vital sign monitoring EIT system for neonatal application.

Despite the promising results reported in many clinical studies, a number of challenges still remain that prevent EIT to progress from research to daily clinical use [9], [10].

In terms of clinical usability, the passive EIT systems [see Figure 2.22 (b)] are impractical to apply in the clinical environment. The multi-leads EIT electrodes also cause cluttering on the neonatal's small chest areas where other vital signs such as heart-rate, and respiratory rate monitoring devices should be attached to. This motivates the development of a compact, wearable and multi-vital sign monitoring EIT system for neonatal lung function monitoring as shown in Figure 1.1.

In terms of hardware design, the major advancements this work focuses on are the active-electrode implementation, EIT image frame-rate, EIT system bandwidth.

EIT image is sensitive to measurement error, often due to unwanted parasitic capacitance effects, noise and common-mode voltage [10]. This motivates the use of active electrodes (see section 2.3.3), as well as novel common-mode feedback techniques towards better noise-performance and high common-mode signal suppression. Also, as an impedance measurement device, the system should be able to measure impedance values with high accuracy (provide measurement results that are close to the known impedance value).

By solving the inverse problem, imaging is used to interpret measured EIT data, and due to the nature of solving an ill-posed inverse problem during image reconstruction, EIT images do not offer high spatial resolution¹ [11]. Thus, differential imaging² is widely adopted in lung monitoring application. This lead EIT to focus on providing images with a high frame-rate (also referred as temporal resolution⁴) [12]. High frame-rate allows more precise analysis of impedance variation at individual moment during a respiration cycle and allows detection of rapid physiological changes continuously at the bedside. For adult lung reparation monitoring, up to 50 fps (frame per second) is implemented in commercial EIT system [13] to follow the pattern of regional inflation of lung e.g. demonstrate areas which inflate faster than other to show tidal recruitment [14] or monitoring intrathoracic impedance caused by perfusion under apnea [15]. As neonates breathing cycle is twice as fast as adults, this motivates for a higher frame-rate of > 100 fps for the targeted application.

Finally, different bio-tissues have different electrical properties as well as frequency response that may be concealed when performing EIT measurement only

¹ spatial resolution: Number of pixels utilized in the construction of an image to identify detailed spatial information

² differential imaging: Imaging inner impedance distribution variation within the object between times intervals

³ temporal resolution: Time required for acquisition of a single frame of image

at one single excitation frequency. This motivates for wideband, multi-frequency analysis towards tissue differentiation (see section 2.3.1.1).

1.1.2 A promising application emerging – EIT for human-machine interfaces

Control of the hand to perform tasks and to communicate with others is doubtless one of human's most valuable assets. With the advancement of technology and the ever-increasing fusion of computer and machine into daily life, a seamless HMI system that can recognize hand gestures and motions and provide the control of robotic machines and prostheses to perform dexterous tasks, is a target of research. Once established, this link between humans and machines can greatly enhance the quality of life, with applications ranging from better control of robotics in, for example, surgery operations, restoring a degree of normality to amputees or safely handling hazardous materials. With such promising motivation, a variety of approaches has been reported to recognise hand gesture and motion recognition for HMI.

Hand motion capture systems can be classified into two main categories [16]. Category A - Image based: It uses a camera to 'see' the gestures and software to interpret the image. The technology has been developed since the nineties with many reported applications [17]. In addition to cameras, depth sensor, are incorporated into the system to improve sensitivity and accuracy [18]. The limitation of this HMI is the requirement for line-of-sight and may not be suitable for prosthesis-related applications. Category B - Non-image based: An alternative approach is to capture the hand motions through a glove equipped with e.g. bend sensors [19]. Glove based HMI has the benefit of being simple and robust but is limited in its range of applications. The most frequently used method is surface electromyography (sEMG). While hand motion is performed, the muscle cells are neurologically activated and generate voltage potentials. By placing electrodes on the skin surface, the voltage potentials can be measured near

these muscle groups. Because different motions activate different muscle groups, successive recorded data can be used for motion classification. This type of HMI can be applied to our daily life as a wearable gadget [20]; it has been dominantly used in active/functional prostheses. According to [21] up to 50% of upper-limb prostheses are based on sEMG, Although sEMG has been generally successful, its signal is very susceptible to noise and interference. EIT is an alternative way of recording raw bio-signals that operate independently with sEMG systems to enhance HMI system performance.

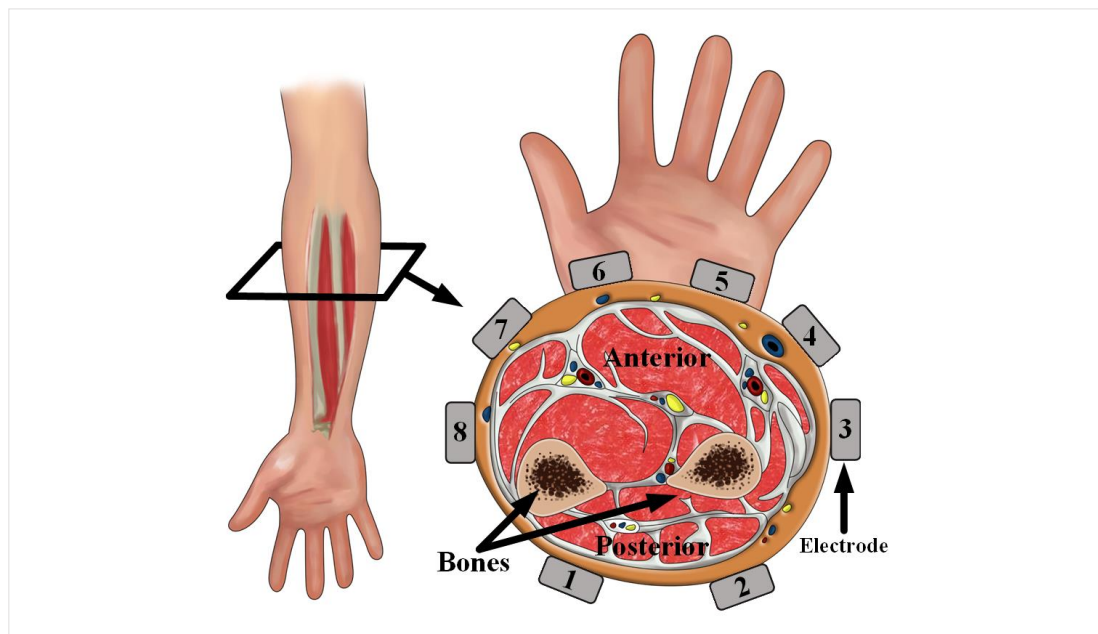


Figure 1.2: Cross-section of the forearm with electrodes placed for EIT.

A cross-section view of the forearm is shown in Figure 1.2, the muscles that control hand motions can be generally grouped into flexors in the anterior surface, and extensors in the posterior surface surrounding the radius and ulna bones, and the hand motion is heavily related to the physical movement of these muscles and bones in the forearm. As different tissues possess different electrical properties, when hand motion occurs, bones and muscles movement resulting in internal impedance re-distribution that can be recorded and ultimately related back to hand motions. These bio-impedance re-distributions can be captured using EIT with an array of electrodes that are wrapped around the forearm.

Originally developed as an imaging technique, EIT has only recently been used for HMI related applications [22], [23]. Compared to thorax applications, HMI EIT is still in its early stages, and the performance of existing systems is limited (see section 2.4.3). This motivates further hardware advancement where an ASIC can be integrated into a compact wearable hand motion recognition EIT system. Using a machine learning algorithm, the bio-impedance pattern can be learned so as to recognize the user's movement intention accurately. The system recognition accuracy is defined as 'percentage of correct predictions' after a set of measured data is classified by the machine learning algorithm.

1.2 Aim and Objectives

In this work, the scope is to develop novel CMOS circuits and wearable systems to better facilitate EIT use in biomedical applications. The aim and objectives of this work are detailed below:

- 1 The research carried out for the neonatal thorax application is part of the European Union's Horizon 2020 Continuous Regional Analysis Device for neonate Lung (CRADL) research project. CRADL aims to provide a respiratory management tool using EIT that can be practically and widely adopted in the neonatal and pediatric clinical area. The research objective is to develop active electrode EIT systems for neonate thorax applications. Systems using ASICs and novel architectures should reduce unwanted parasitic capacitance effect, and improve noise performance, common-mode suppression, as well as system bandwidth and image frame-rate. The system also incorporates other vital clinical functionalities towards achieving wider clinical acceptance.
- 2 To carry out preliminary studies on prosthesis hand control using and developing an advanced HMI EIT system in CMOS technology to further research this

important new application. The aim is to investigate the potential problems and identify possible future hardware development and research direction for this application.

- 3 To propose and implement innovative circuitry that play a crucial role in EIT hardware, such as the active current driver, instrumentation amplifier (IA) and impedance demodulation circuit to better facilitate the development of EIT system.

Some of the digital circuits presented in this thesis have been accomplished in collaboration with Dr Dai Jiang, University College London. The wearable belt fabric dressings for thorax application presented in this thesis have been designed in collaboration with, and fabricated by redLoop, Middlesex University, London.

1.3 Thesis Overview

The thesis is organised as follows. An overview of EIT is given in Chapter 2, including the principle of operation of EIT, EIT hardware specification, EIT system architectures and a review of the state-of-the-art EIT systems. Chapter 3 describes the first EIT system developed, namely the CRADLvision 1.0. It uses an ASIC to perform both current injection and voltage recording using active electrodes. In Chapter 4, a novel EIT active electrode system architecture is presented with an improved, highly integrated active electrode ASIC; this is the CRADLvision 2.0 EIT system, developed with superior system performance and functionalities. It is able to detect lung respiration, breathing cycles, heart rate and track boundary shapes. In Chapter 5, the HMI system for hand prosthesis control is presented. The system is in the form of wearable band and is able to capture hand-motions using EIT with a 98.5% accuracy. Its medium-term performance is investigated, and the merits as well as the limits of

EIT as an HMI system are identified. Finally, conclusions and ideas for future work are presented in Chapter 6.

1.4 List of publications

The work described in the thesis has resulted in the following publications.

Journal publications:

Y. Wu, D. Jiang, A. Bardill, R. Bayford and A. Demosthenous, "A 122 fps, 1 MHz Bandwidth Multi-Frequency Wearable EIT Belt Featuring Novel Active Electrode Architecture for Neonatal Thorax Vital Sign Monitoring," in IEEE Transactions on Biomedical Circuits and Systems, doi: 10.1109/TBCAS.2019.2925713.

Y. Wu, D. Jiang, X. Liu, R. Bayford and A. Demosthenous, "A Human-Machine Interface Using Electrical Impedance Tomography for Hand Prosthesis Control," in IEEE Transactions on Biomedical Circuits and Systems, vol. 12, no. 6, pp. 1322-1333, Dec. 2018.

Y. Wu, D. Jiang, A. Bardill, S. de Gelidi, R. Bayford and A. Demosthenous, "A High Frame Rate Wearable EIT System Using Active Electrode ASIC for Lung Respiration and Heart Rate Monitoring," in IEEE Transactions on Circuits and Systems I: Regular Papers, vol. 65, no. 11, pp. 3810-3820, Nov. 2018.

Conference publications:

Y. Wu, D. Jiang, Peter Langlois, R. Bayford and A. Demosthenous, "A Power-efficient Current Generator with Common-mode Signal Auto-zero Feedback for Bio-impedance Measurement Applications," 2019 IEEE International Symposium on Circuits and Systems (ISCAS), Sapporo, 2019.

Y. Wu, D. Jiang, A. Bardill, S. de Gelidi, R. Bayford and A. Demosthenous, "Live Demonstration: A Wearable Torso Shape Detection Belt for Lung Respiration Monitoring," 2019 IEEE International Symposium on Circuits and Systems (ISCAS), Sapporo, 2019.

Y. Wu, D. Jiang, J. Duan, X. Liu, R. Bayford and A. Demosthenous, "Towards a High Accuracy Wearable Hand Gesture Recognition System Using EIT," 2018 IEEE International Symposium on Circuits and Systems (ISCAS), Florence, 2018, pp. 1-4.

Y. Wu, D. Jiang, R. Bayford and A. Demosthenous, "Live Demonstration: A Wearable EIT System for Hand Prosthesis Motion Controls," 2018 IEEE International Symposium on Circuits and Systems (ISCAS), Florence, 2018, pp. 1-1.

Y. Wu, D. Jiang, P. Langlois, R. Bayford and A. Demosthenous, "A CMOS current driver with built-in common-mode signal reduction capability for EIT," ESSCIRC 2017 - 43rd IEEE European Solid-State Circuits Conference, Leuven, 2017, pp. 227-230.

Y. Wu, D. Jiang, A. Bardill, S. De Gelidi, R. Bayford and A. Demosthenous, "Live demonstration: A wearable EIT system using active electrodes for monitoring respiration," 2017 IEEE International Symposium on Circuits and Systems (ISCAS), Baltimore, MD, 2017, pp. 1-1.

Y. Wu, P. Langlois, R. Bayford and A. Demosthenous, "Design of a CMOS active electrode IC for wearable electrical impedance tomography systems," 2016 IEEE International Symposium on Circuits and Systems (ISCAS), Montreal, QC, 2016, pp. 846-849.

Chapter 2

An overview of EIT

2.1 Introduction

In the early 1920s, geologists injected currents into the earth and analysed the geological structure by measuring the voltage induced on the earth surface. By analysing the conductivity distribution of different layers, underground mineral resources can be predicted. This is an early form of EIT, and it is not until the 1980s that EIT was introduced as a medical imaging technique. Its imaging concept is similar to computed tomography (CT), but uses electrical impedance measurements from the SUT, so is described as 'Electrical Impedance Tomography'.

This chapter provides an overview of EIT technology, starting from the basic operation of EIT which is introduced in section 2.2. A study of the EIT hardware specification is given in section 2.3, specifically on the fundamentals of the bio-impedance measurement technique, and the analog front-end specification of the EIT system. Section 2.4 covers EIT system architectures with an EIT system review given, and finally the conclusion is given in section 2.5.

2.2 Basic of EIT operation

A simplified demonstration of EIT is shown in Figure 2.1. The SUT in this example is an enclosed cube model shown in Figure 2.1(a) where its boundaries are marked by the orange lines. The model has a uniformly distributed inner conductivity known as

σ_{sut} . Using two electrode plates, a constant current is injected and flows through the model from $I +$ to $I -$. The flow of the current is indicated by the red arrow. Due to this current, voltage is induced that is measurable on the model's surface. The black horizontal lines are the induced equipotential lines. By placing a voltage amplifier on the surface of this model as shown, V_{out} can be measured for analysis.

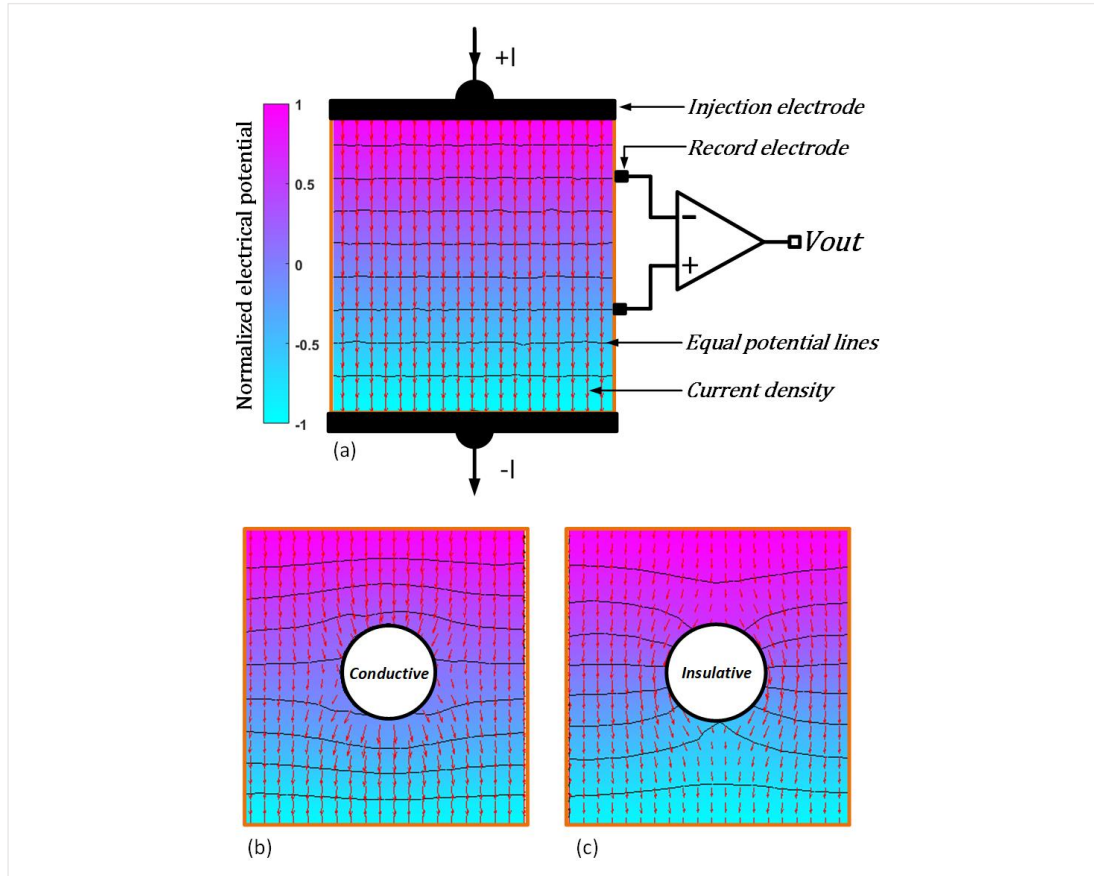


Figure 2.1: A simplified EIT concept illustration (a) Top view of the model with a constant current injection. (b) The same model with conductive cylinder immersed. (c) The same model with insulative cylinder immersed, the colour bar indicates normalized electrical potential.

As shown in Figure 2.1(b), if a circular conductive solid cylinder ($\sigma_{cylinder} > \sigma_{sut}$) is immersed inside the SUT, the uniform conductivity is then disturbed. When current is applied, the flow of the current indicated by the red arrows which were once uniformly going downwards is now deflected inward because more current flows inside the cylinder; at the same time, the equipotential lines which will always be perpendicular to the current flow are curved accordingly. If V_{out} is measured by the same amplifier

at the same position, a reduction in voltage can be detected at the cube model's surface. When $\sigma_{\text{cylinder}} < \sigma_{\text{sut}}$ as shown in Figure 2.1(c), the field lines will be parallel (tangential) to the surface of the insulated cylinder because there is little current through it, and this leads to a voltage increase for V_{out} . Effectively, the amplifier measures the equivalent impedance between its input terminals with current injection.

In this example, if the solid cylinder only moves up and down the centre vertical line, having multiple amplifiers evenly placed alongside the cube wall can measure the voltage distribution developed. One can then estimate the location and the electrical property of the immersed object by simply monitoring the changes in voltages and compare them to the original voltage values when the cube contains no solid cylinder. This is the basic concept of EIT: Measurement of changes in terms of conductivity or resistivity distribution happening within the SUT.

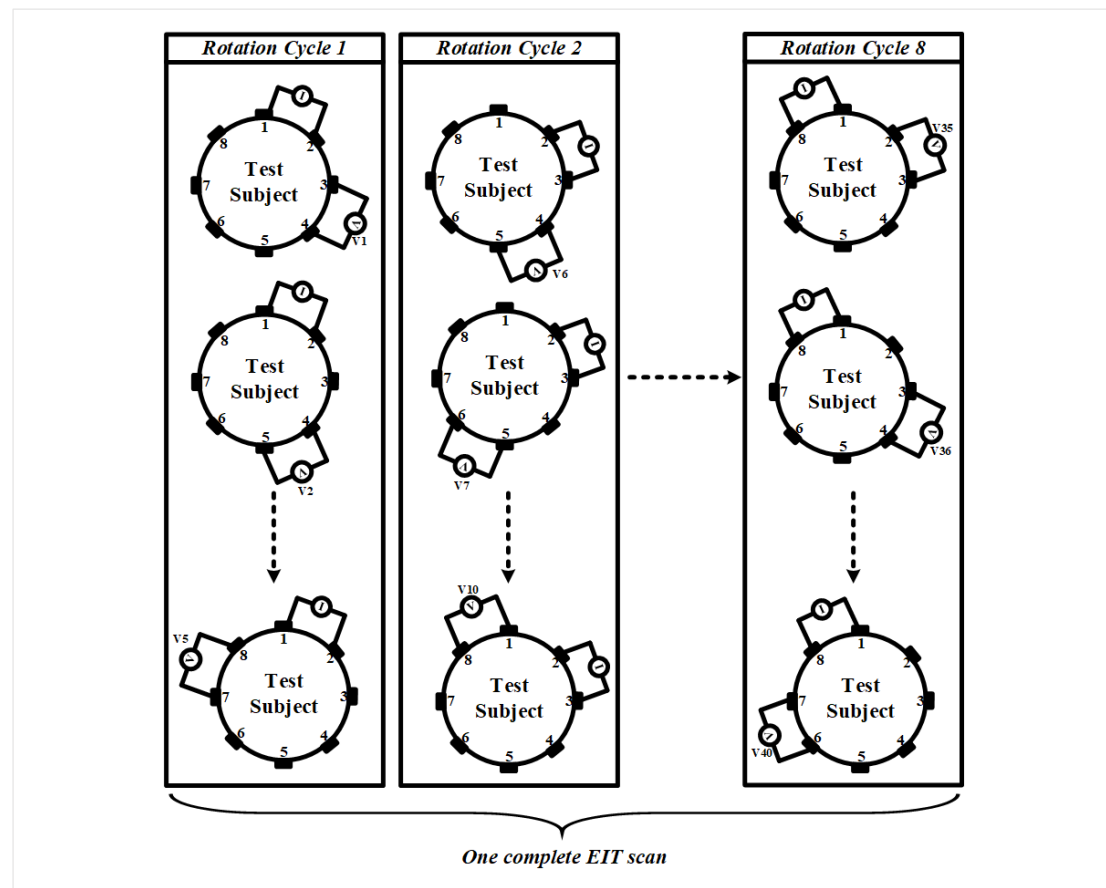


Figure 2.2: A typical EIT adjacent rotation scan illustration with an array of 8 electrodes.

In a further step, to fully obtain the inner conductivity distribution map of the SUT (now a cylinder), an array of electrodes is attached to the circumference of the SUT. The voltages developed due to rotating current injection are measured sequentially according to a pre-set scan pattern. This allows a set of data that can better represent the inner conductivity distribution of the SUT to be obtained. This pre-defined injection and measurement pattern is called EIT scan pattern or driven sequence. There are a number of different scan patterns, and each has its own merit and pitfalls [24]. The most frequently used scan pattern is called the 'adjacent scan pattern' whose operation is shown in Figure 2.2.

For eight electrode EIT as shown in Figure 2.2, there are 8 cycles of rotation. In each rotation a current is injected a selected pair of electrodes, the voltage amplifier stepwise measures the resulting differential voltage across each pair of remaining electrodes. It should be noted that the electrode combination selected for voltage measurement does not involve any of the current injection electrodes, this is due to contact impedance issues which will be explained in section 2.3.1.2. Once all the voltages are captured, a new rotation cycle begins. In the new cycle, the current is injected through the next adjacent electrode pair and a second set of voltages is recorded. This is repeated until all the electrode combinations have been used for current injection. After all available possible electrode pairs have been applied an EIT scan is fully completed. Ignoring the injecting electrodes for measurement, $(n - 3) \times n$ voltage readings are collected in an EIT scan where n is the number of electrodes used.

As explained earlier, EIT is often used, particularly in lung monitoring, to capture the changes occurring inside the SUT. Thus, to reconstruct an image, two complete EIT scans with a time-difference is normally required. This is called 'time-difference' or 'differential imaging'. The reconstructed image then shows the changes happened Δt or a number of Δt later compared to in the initial state of the SUT. With differential imaging, any static element e.g. voltage due to the sternum and rib cage while imaging

the respiration of lungs, is seen as a common-mode (CM) signal which can be cancelled out in the final image. After the data is ready, as shown in Figure 2.3, the reconstruction software creates a finite element model (FEM) using the contour of the SUT as the boundary condition. This model is also based on the specific operation conditions of EIT including the number of electrodes, the electrode placement and scan patterns etc. Using the data collected, the inverse-problem solver tries to recover the alteration in conductivity that has caused such particular voltage variations between the two data sets and presents its estimated conductivity alteration inside the FEM model.

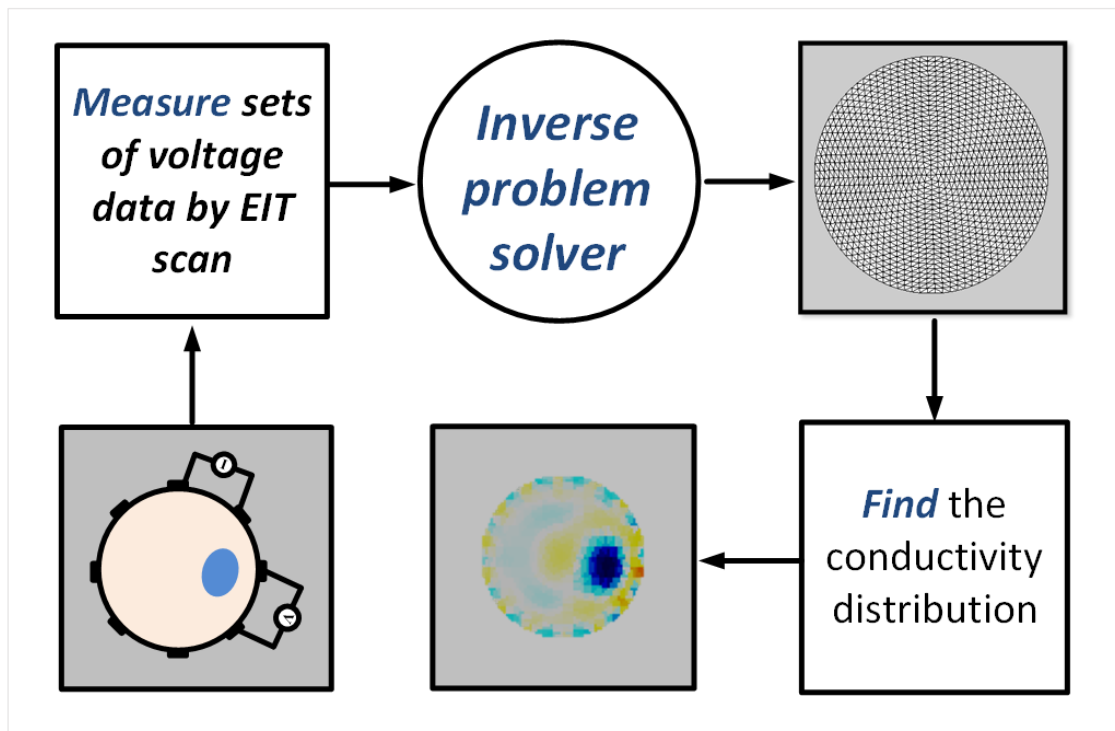


Figure 2.3: The overall operation flow of EIT - from measurement to image.

Solving the inverse-problem is an important but challenging step in EIT technique [25]. This is because with a finite number of electrodes, the number of independent measured data is often fewer than that of the conductivity elements in the FEM model. The algorithms try to solve a mathematically ill-posed equation, and a small amount of noise within the measured data can result in large errors [26]. The EIT image reconstruction software used in this work is adapted from EIDORS [27] (an open

source EIT software for image reconstruction). In-depth theory and implementation of the reconstruction algorithms is also a topic of research and is not within the scope of this work.

2.3 Study of EIT hardware specification

2.3.1 Fundamentals in bio-impedance measurement (BIM)

2.3.1.1 Introduction to bio-impedance

Biological tissue has electrical properties that can be measured and studied to provide valuable information about their physiological as well as pathological conditions [28], [29]. These properties include both electrical conductivity (σ) and relative permittivity (ϵ_r) which are attributed to the fundamental cell structure. A simplified cell structure is shown in Figure 2.4.

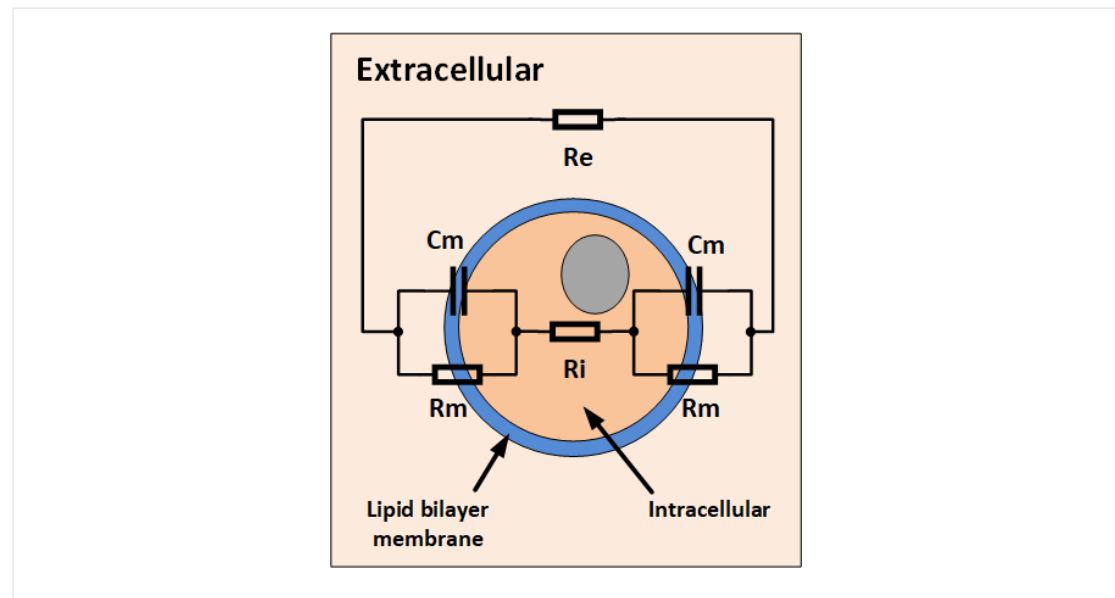


Figure 2.4: The structure of a cell and its corresponding Fricke equivalent circuit. R_e : extracellular resistance, R_m : membrane resistance and C_m : membrane capacitance, and R_i : intracellular resistance.

The cell is surrounded by the extracellular fluid containing ions and electrolyte with its intracellular fluid and other structures enclosed by a lipid bilayer membrane [30].

The extracellular as well as intracellular fluid contribute to the conductive properties whereas the lipid bilayer membrane contains two layers of glycerol lipids [31] that electrically act as a capacitor.

To better aid the circuit analysis, the equivalent circuit is proposed by Fricke [32] to model the cell electrical structure as a combination of resistors and capacitors as shown in Figure 2.4. As a result of tissue diversity, this suggests that the ac bio-impedance characteristics can be used for tissues feature identification [33].

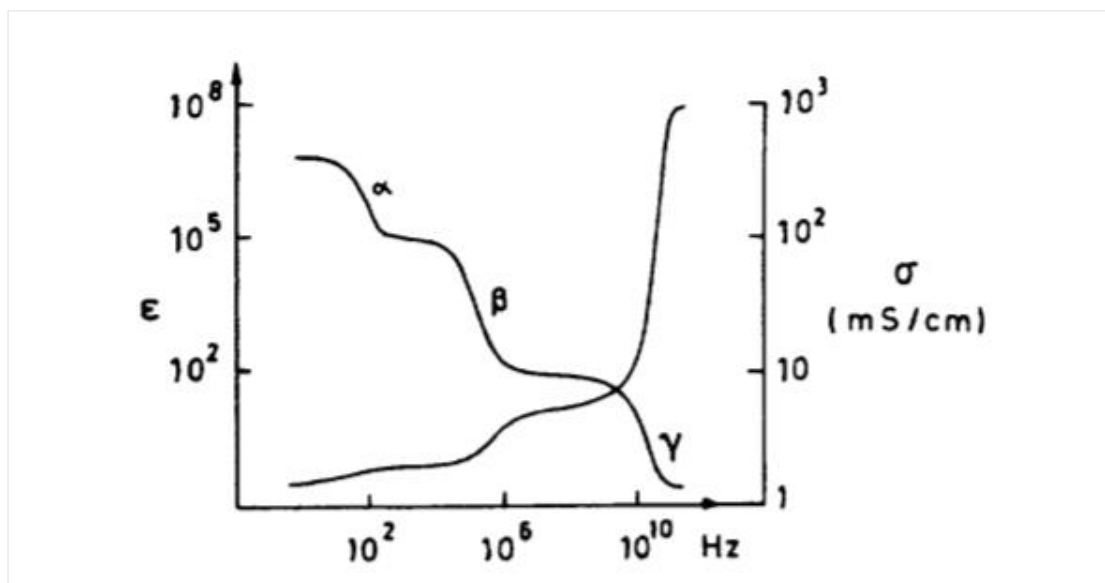


Figure 2.5: Tissue conductivity and relative permittivity with respect to frequency [34].

As shown in Figure 2.5, the relative permittivity and the conductivity of the biological tissues vary with respect to frequency and are divided into three dispersion regions [34]. The alpha (α) dispersion ranges from few Hz up to 10 kHz; it is attributed to various mechanisms as stated in [34] e.g. the existence of the sarcoplasmic reticulum in the muscle tissue. The beta (β) dispersion starts from 100 kHz up to 10 MHz, but levels off around 1 MHz. This dispersion region is related to the cellular structure of tissues which reflect structural changes and indicate pathological status that is of interest to the clinical applications [35]. The gamma (γ) dispersion is due to water contained within the tissues and cells, and it takes place from GHz which is beyond the bandwidth of concern.

2.3.1.2 BIM techniques and electrode interfaces

Hydrated ions such as Na^+ , H^+ and Cl^- are the charge carriers inside the tissues, whereas, in the electronic system, the charge carriers are the free moving electrons. When the electrode is in contact with the electrolyte (e.g. skin), it acts as the medium to make the charge transfer. The transfer can be done through Faradaic or non-Faradaic processes [36].

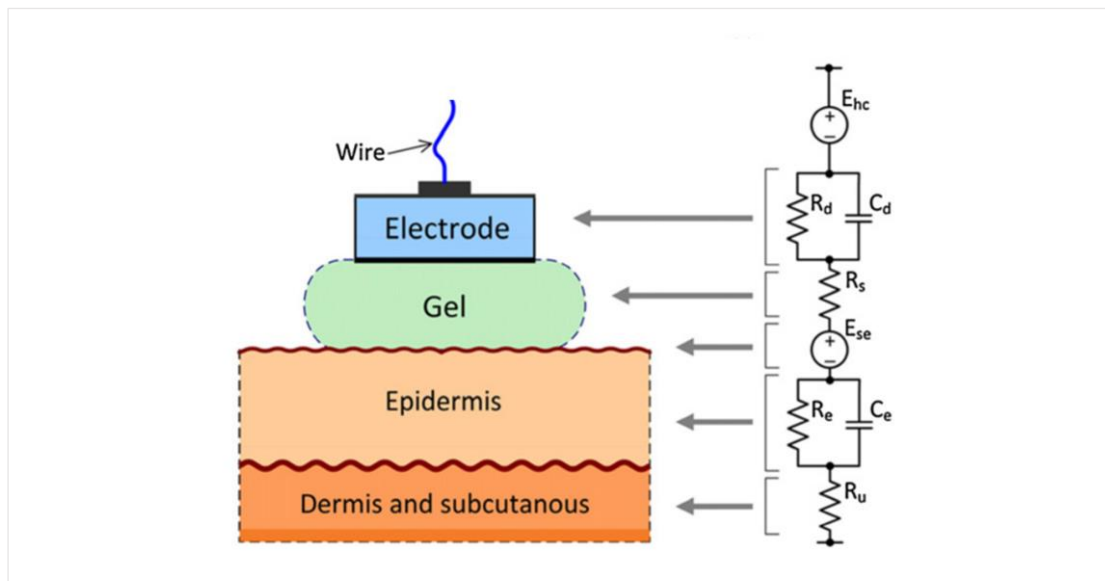


Figure 2.6: Electrical model for electrode-to-skin interface. Left, gel electrode, and right, simplified model from [37].

For the non-Faradaic process, the electrode-electrolyte interface can be modelled as a capacitor C_d due to a double layer structure formed between the interfaces. The type of electrode in the non-Faradaic process is called a polarisable electrode. Whereas for the Faradaic process, oxidation or reduction reaction occurs depending on the direction of current flow. In this process, the interface is modelled as a Faradaic resistor and this type of electrode is known as a non-polarizable electrode. As there is no perfect polarizable or non-polarizable electrode, both Faradaic and non-Faradaic processes can occur in parallel, and as a result, the equivalent model of the electrode-skin interface is shown in Figure 2.6. Detailed electrochemical processes are not considered in this work.

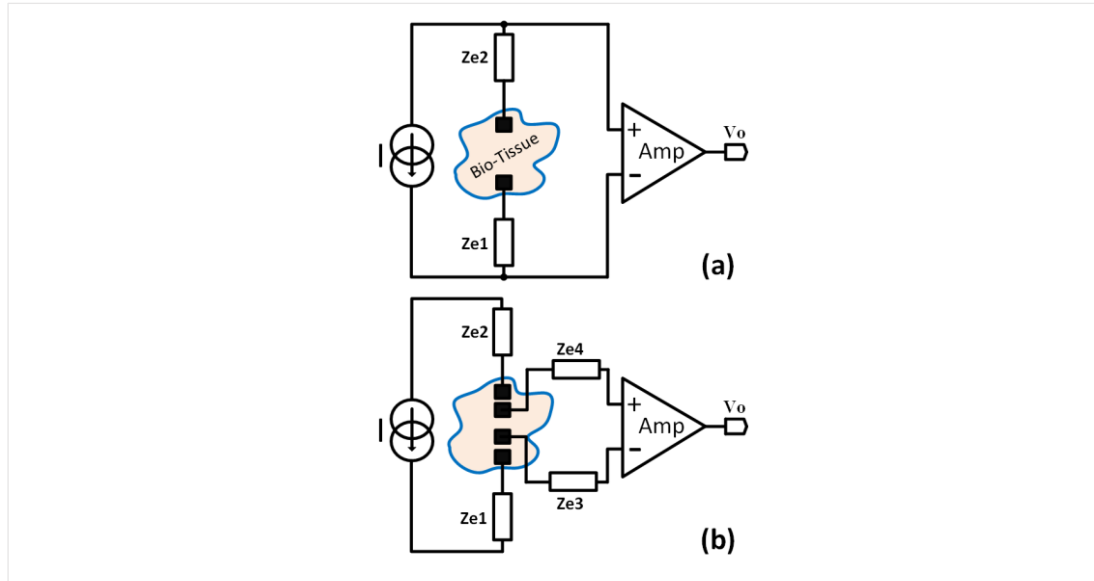


Figure 2.7: Bio-impedance measurement technique (a) two-electrode (b) four-electrode.

As shown, E_{hc} is the equilibrium potential from the electrode-electrolyte interface, C_d and R_d are the electrode-electrolyte interface impedance and R_s is the electrolyte resistance. E_{se} is the equilibrium potential for the electrolyte-skin interface, and C_e , R_e are the epidermis layer impedance and R_u is the dermis layer resistance [37]. This combination of impedances is considered to be the electrode impedance Z_e . Z_e is usually much larger than the body tissue impedance Z_{sut} but the value of electrode impedance varies depends on the size, material and how the electrode is applied, e.g. gel/dry electrode where $Z_{dry} \gg Z_{gel}$.

A comprehensive study of electrode characteristics for EIT is reported in [38]. The contact impedance of different types of electrodes is measured using the two-electrode measurement technique as shown in Figure 2.7(a), and the results are shown in Figure 2.8. It can be seen that at 1 kHz, the contact impedance could be much higher than 10 k Ω but drops to 1 k Ω when the signal frequency increases above 100 kHz. In addition, more information relating to tissue characteristics can be collected with wideband excitation (according to β -dispersion). Thus it suggests that the EIT system should have a wide bandwidth from 100 kHz up to 1 MHz. However, conventional passive EIT systems have limited bandwidth due to the parasitic capacitance effect [39]. As a

result, many clinical EIT studies for thorax EIT were carried out at one fixed frequency e.g. 50 kHz and this has limited the potential of bio-impedance analysis [40].

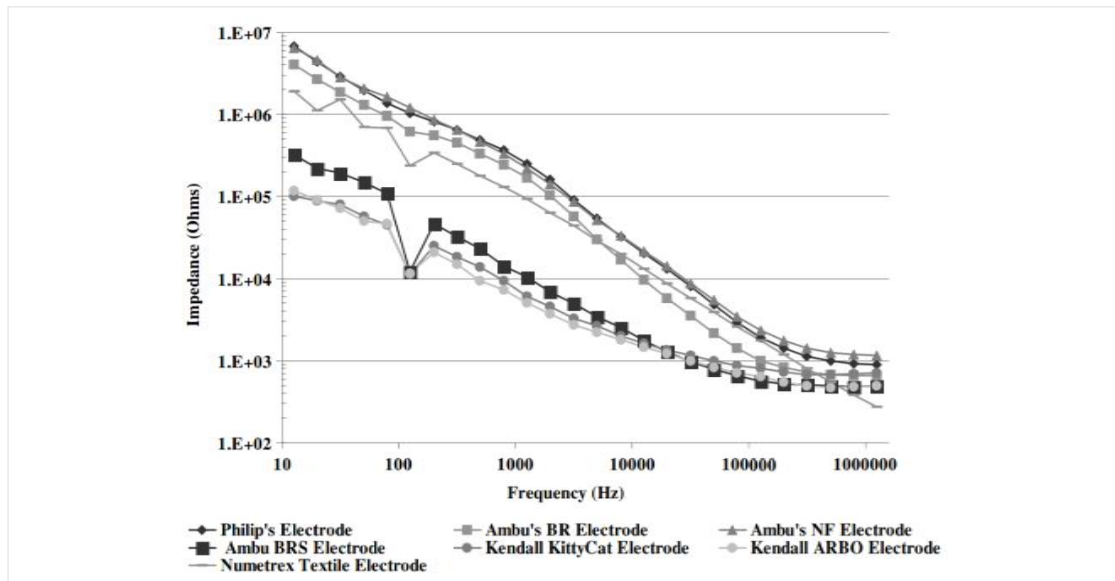


Figure 2.8: Measured electrode contact impedance reported in [38].

As shown in Figure 2.7(a), the two-electrode measurement technique gives the contact impedance $Z_c = 2 \times Z_e + Z_{sut}$, where $Z_e \gg Z_{sut}$. To obtain only tissue impedance Z_{sut} , the standard bio-impedance measurement technique used is the four-electrode technique as shown in Figure 2.7(b). When taking a voltage measurement, the electrode impedance Z_{e3} and Z_{e4} is in series with the high input impedances of the voltage amplifier, so that the voltage measured is only attributed to the tissue impedance. Furthermore, during EIT, when the voltage scan overlaps with the current injecting electrode, it measures full or part of the electrode impedance Z_e . Not only do the resulting high voltages saturate the amplifier but also are unrelated to inner impedance changes thus is considered unreliable for image reconstruction. As a result, as shown in Figure 2.2, the EIT scan data does not include any combinations that involves current injection electrodes.

The electrodes also have noise characteristics which depend on a number of factors. It is reported in [41] that skin preparation (e.g. cleaned with alcohol) can reduce the electrode noise by up to 80%, [41] also shows that the noise increases from less

than $2.5 \mu V_{rms}$ to almost $200 \mu V_{rms}$ in a 500 Hz bandwidth due to muscle activity. The noise is also related to skin-electrode contact condition (gel wet or dry), and electrode size. In [42], it is shown that the noise in a dry electrode can be up to 10 times higher compared to a wet/gel electrode, also it reported that smaller size electrodes tend to be more noisy than larger ones. Finally, the noise of the electrode is highly dependent on the electrode material as shown in [43], the Cu-Ni fabric electrode has a noise density measured up to $1 mV/\sqrt{Hz}$ whereas a Cu-Ni-Au electrode has only $93 \mu V/\sqrt{Hz}$.

The circuit shown in Figure 2.7(b) is considered as the analog-front-end of a BIM system. To extract the bio-impedance value, namely the real and imaginary part of the impedance component, demodulation is required. There are two well-known demodulation techniques, the first is I-Q demodulation or coherence detection. Its operation principle is shown in Figure 2.9.

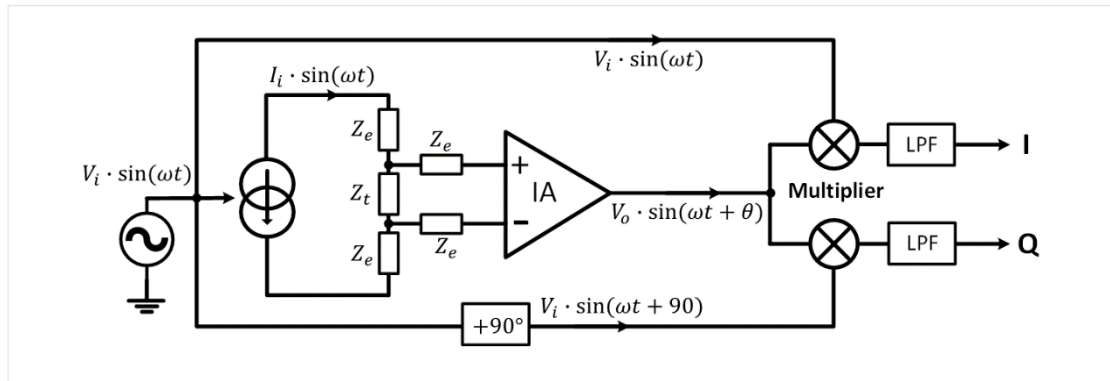


Figure 2.9: I-Q demodulation for bio-impedance measurement.

First an excitation voltage $V_i \cdot \sin(\omega t)$ is generated. This voltage is sent to the current driver which converts the V_i to a current $I_i \cdot \sin(\omega t)$. The current passes through the tissue with a bio-impedance of Z_t and using an IA, the voltage developed on Z_t is measured as V_o which is equal to:

$$V_o = I_i \cdot Z_t \cdot A \cdot \sin(\omega t + \theta) \quad (2.1)$$

where θ is the phase delay due to the Z_t with respect to V_i , and A is the gain of IA

The original excitation voltage V_i is sent on two paths namely I (in phase), and Q (quadrature phase). In the Q path, a 90-degree phase shift is added to the V_i and in

both paths, the in phase and quadrature phase signal is multiplied by the output voltage V_o . This yields the following multiplication equation:

For the in-phase part:

$$\begin{aligned} V_i \times V_o &= I_i Z_t A \cdot \sin(\omega t + \theta) \cdot V_i \cdot \sin(\omega t) \\ &= \frac{I_i Z_t A \cdot V_i}{2} \cdot [\cos(\theta) - \cos(2\omega t + \theta)] \end{aligned} \quad (2.2)$$

For the quadrature-phase part:

$$\begin{aligned} V_{i_quadrature\ phase} \times V_o &= I_i Z_t A \cdot \sin(\omega t + \theta) \cdot V_i \cdot \sin(\omega t + 90) \\ &= \frac{I_i Z_t A \cdot V_i}{2} \cdot [\cos(\theta - 90) - \cos(2\omega t + \theta + 90)] \end{aligned} \quad (2.3)$$

The low-pass filter (LPF) after the multipliers removes the high-frequency component from equation (2.2) and (2.3), and gives the following dc component:

$$I_{demo} = \frac{I_i Z_t A \cdot V_i}{2} \cdot \cos(\theta) \quad (2.4)$$

$$Q_{demo} = \frac{I_i Z_t A \cdot V_i}{2} \cdot \cos(\theta - 90) = \frac{I_i Z_t A \cdot V_i}{2} \cdot \sin(\theta) \quad (2.5)$$

By dividing a known factor $\frac{I_i \cdot A \cdot V_i}{2}$, the above can be converted back to the corresponding impedance component:

$$Re\{Z_t(\omega)\} = Z_t \cdot \cos(\theta) = \frac{2 \times I_{demo}}{I_i \cdot A \cdot V_i} \quad (2.6)$$

$$Im\{Z_t(\omega)\} = Z_t \cdot \sin(\theta) = \frac{2 \times Q_{demo}}{I_i \cdot A \cdot V_i} \quad (2.7)$$

The I-Q demodulation can be performed based on either analog or digital implementations. For example, with analog implementation, the in-phase and quadrature signal can be generated by e.g. a quadrature oscillator [44] whereas for digital implementation, a digital to analog converter (DAC) based direct digital synthesis (DDS) can be used. Each implementation has its own merits and pitfalls [45]. For the analog approach, the circuit may require less power and as the final signal is dc, the requirement for the analog to digital converter (ADC) is much relaxed. However, the challenge may lie in producing precise and wideband I-Q signals, and good performance analog multipliers.

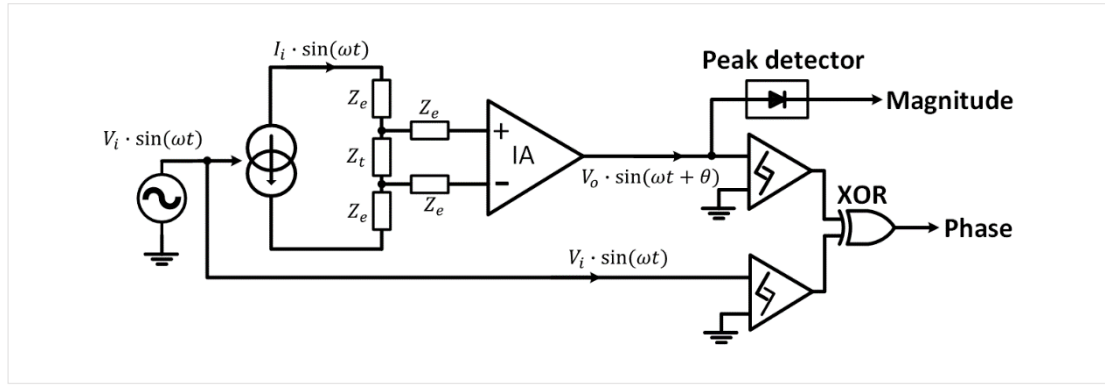


Figure 2.10: Magnitude and phase demodulation for bio-impedance measurement.

Furthermore, to obtain the dc signal, the LPF may require a large time constant. This leads to long settling time and reduces overall EIT scanning speed. For the digital implementation, as all the signal processing is done in the digital domain using e.g. Field-programmable gate array (FPGA), it offers more precise control, high-speed operation. More importantly, the digital approach offers more flexibility and room for modification and upgrade. However, the digital processing may require more power, also high precision, and high speed converters are considered necessary.

The alternative demodulation method is magnitude and phase demodulation. It is based on the fact that, other than real and imaginary component, it gives identical information when the impedance magnitude Z_t and phase θ is obtained as shown in equation (2.6) and (2.7). When current is injected into the tissue, the voltage measured V_o as shown in equation (2.1) already contains these two components in the time-domain output sine wave. The principle of the magnitude and phase demodulation method is to extract the amplitude of V_o for impedance magnitude and the time delay between V_i and V_o for the phase θ extraction. The circuit implementation is shown in Figure 2.10. For magnitude detection, a peak detector can be implemented to capture the peak value that is equal to $I_i \cdot Z_t \cdot A$ in which the I_i and A is known. For the phase, two comparators are used to detect the zero crossings of V_i and V_o , and through an XOR gate, the phase can be extracted by measuring the time difference between the zero crossing points of the two signals. This method is much simpler than the I-Q demodulation. However, it maybe be more susceptible to noise. Any dc offset

or noise in the signal could lead to error in the peak value detection. Also, due to input offsets, and the propagation delays of the comparators, accurate phase measurement maybe very difficult to obtain.

For wideband operation, other sources of errors in demodulation methods could be due to the limited bandwidth of the analog hardware. For example the current driver which converts the input voltage V_i to a output current according to a defined transconductance G_m , however, as frequency increases, the nominal value of the transconductance decays, together with added phase delay with respect to the V_i as shown below:

$$I_i\{\omega\} = \frac{V_i \cdot G_m \cdot \sin(\omega t + \Delta\phi\{\omega\})}{\sigma\{\omega\}} \quad (2.8)$$

where $\sigma\{\omega\}$ is the percentage decay in current driver's transconductance, and $\Delta\phi\{\omega\}$ is the phase delay as a function of frequency.

2.3.1.3 Safety

For bio-impedance measurement, the main safety concerns are in respect of current injection. The current injection must comply with the IEC 60601-1 standard [46] which refers to the current injected by electrodes as 'the patient auxiliary current'. At dc or low frequency, injection of current can lead to electrolysis at the electrode-tissue interface. The electrolysis at low frequency is irreversible and can cause damage to the tissue. At frequencies higher than 10 Hz, when oxidation or reduction reaction occurs it is reversible when the applied potential is reversed [47]. At higher frequencies, the safety concern is associated with stimulations which cause the sensation of pain and undesired muscle contractions. Moreover, excessive current injection generates heat that can lead to injury. This is one of the important reasons that voltage injection for bio-impedance measurement is not preferred, because changes within the SUT could result in lower impedances that lead to an excessive current drawn if not monitored.

The patient auxiliary current I_i permissible by IEC60601-1 for bio-impedance measurement is frequency dependent as shown below:

$$I_i = \begin{cases} 100 \mu A_{rms} & @ 0.1 \text{ Hz} < f < 1 \text{ kHz} \\ 100 \times f / 1 \text{ kHz} \mu A_{rms} & @ 1 \text{ kHz} < f < 100 \text{ kHz} \\ 10 \text{ mA}_{rms} & @ 100 \text{ kHz} < f \end{cases} \quad (2.9)$$

Other medical device safety considerations may include device failure, protective earth return path, ESD protection and mains isolation.

2.3.2 EIT analog-front-end

2.3.2.1 Current injection in EIT

The current driver is used to inject a load independent current into the tissue during bio-impedance measurement. As its performance significantly influences the measurement result in any EIT system, the following details must be considered when designing a current driver.

- *Bandwidth and output impedance:*

When designing a current driver, the goal is to output a load-independent current within the frequency band of interest. Thus, the dominant pole should be located at high frequency to avoid transconductance roll-offs and output phase delays. At the same time, the current driver output impedance Z_o should be maintained large enough to ensure that most of the current is delivered to the load. An ideal circuit model for the current driver is shown in Figure 2.11(a), where the current driver is a constant transconductance G_m with an infinite output resistance R_o regardless of the frequency of operation, so that all the current is delivered to the load R_L .

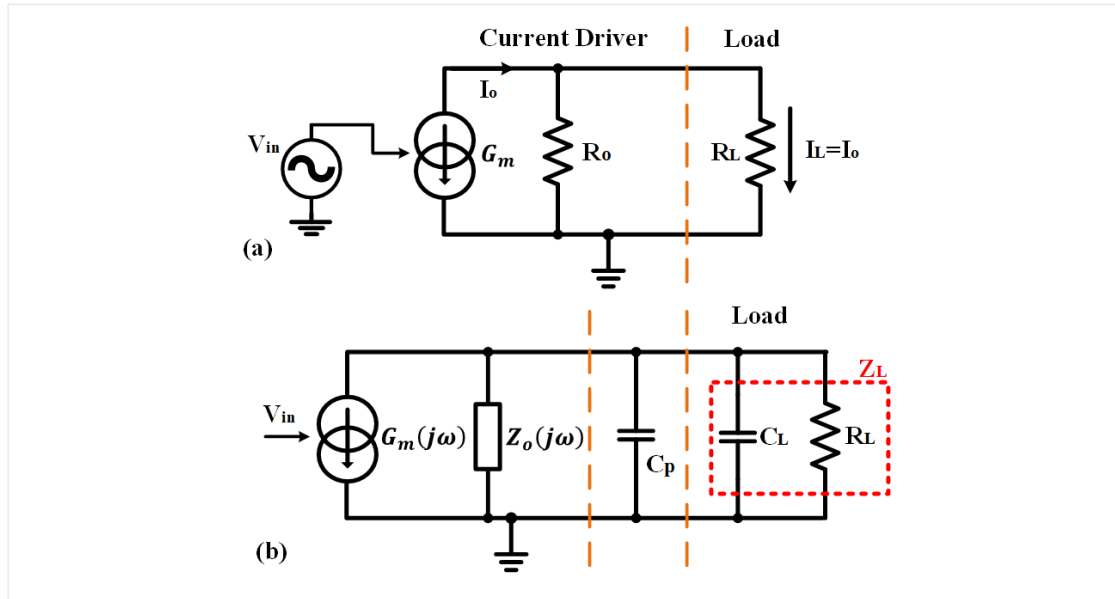


Figure 2.11: The equivalent model for the current driver (a) with resistive load (b) with impedance CL , RL load and parasitic capacitance Cp .

However, the more realistic situation is shown in Figure 2.11(b). Due to limited bandwidth of the circuit, the Gm of the current driver and its output impedance Zo varies with respect to frequency. As the frequency increases, the output current drops from its nominal value due to Gm roll-off, together with increased phase delay. At the same time, the output impedance decreases, and the output current becomes less load-independent. It is reported in [48] that the current driver such as [49] employs a closed-loop feedback which measures the output current to keep it load independent, can achieve a wider bandwidth with a output impedance higher by a factor of the feedback loop gain.

Despite having a closed-loop feedback, because parasitic capacitance Cp is not a part of the current driver feedback loop, the Cp is inseparable from the load Z_L . It shunts away some output current and it appears that the current driver has an even lower output impedance. In addition, the parasitic capacitance introduces additional phase delay that does not originate from the bio-impedance load. For BIM, as current flows through Z_L as shown in Figure 2.11(b), the system demodulates the amplitude and phase of the voltage developed on Z_L with respect to the input voltage as

described in section 2.3.1.2 to extract the value of R_L and C_L . In this process, the parasitic capacitance introduces unwanted effect that leads to errors.

- *Current amplitude and differential injection:*

As mentioned in section 2.3.1.3, over 100 kHz, up to 10 mA_{rms} can be injected into the SUT.

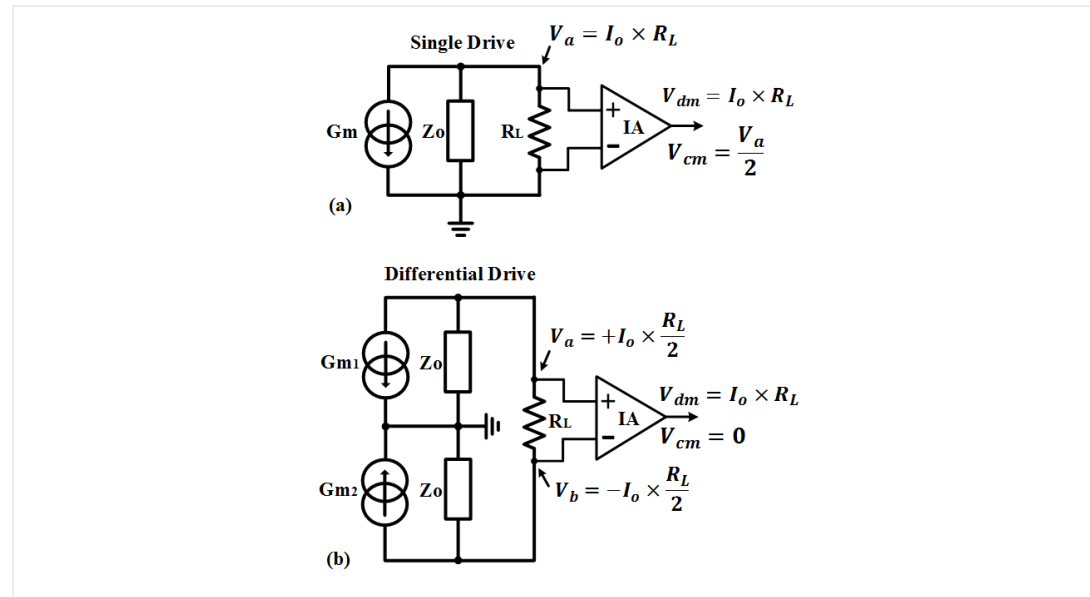


Figure 2.12: (a) Single-ended current drive; (b) Fully differential drive.

Because the amplitude of the induced voltage is proportional to the current amplitude, within the maximum safe limit, bearing in mind power consumption concerns, higher current injection results in better measurement signal-to-noise ratio (SNR). To avoid output saturation when driving high impedance load, the current driver should also have a large voltage compliance.

An important design specification for EIT current injection is the use of fully differential drive as shown in Figure 2.12(b) compared to the single-ended drive shown in Figure 2.12(a). It uses two identical current drivers where the upper one sources current into the R_L while the lower one sinks current to form a complete current path. As shown, in this drive mode, the load becomes floating, and this has several advantages. Firstly, the output impedance that the load sees is effectively doubled. Secondly, as the load is floating, the voltage compliance is also doubled under the

same supply compared to single-ended drive. Most importantly, compared to single-ended drive, even though the measured differential voltage is the same, the common-mode voltage seen by the IA is reduced from $\frac{V_a}{2}$ to zero in the ideal case as shown in Figure 2.12.

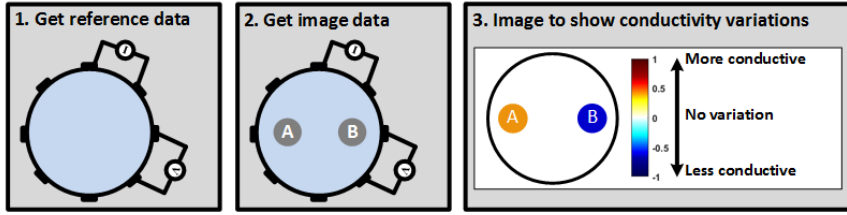
In summary, the design of the current driver should employ a feedback mechanism with a loop that has large gain-bandwidth to achieve a constant transconductance with a sufficient output impedance Z_o . Efforts should be taken to reduce any unwanted parasitic capacitance effect which reduces the output impedance and leads to more phase error.

2.3.2.2 Voltage measurement in EIT

In the previous sections, the analysis was primarily based on a two-port load, however, for EIT measurement, as shown in Figure 2.2, several voltages are measured at different locations providing different voltage patterns. To this end, an alternative load model (an EIT phantom) is required for EIT system design, testing and calibration prior to any *in-vivo* test.

In general, there are two types of EIT phantom model, the physical and resistive phantom. The physical phantom consists of a liquid (saline solution) or gel inside a circular container with surface electrodes as shown in Figure 2.13 (a). When the phantom contains only the saline solution, a set of EIT voltages are measured and used as reference data to represent this initial state Figure 2.13 (a-1). Then other objects feature different conductivity can be inserted into the phantom. This causes an inner conductivity re-distribution which is also captured through EIT measurement Figure 2.13 (a-2). Using the data, a differential EIT image (see section 2.2) is produced as shown in Figure 2.13 (a-3). This image shows the regions where conductivity re-distribution occurred compared to the initial stage. Colour mapping method uses red to indicate higher conductivity and blue for lower conductivity as shown in Figure 2.13 (a-3).

(a) Differential imaging using a physical phantom



(b) EIT 32-electrode resistive phantom

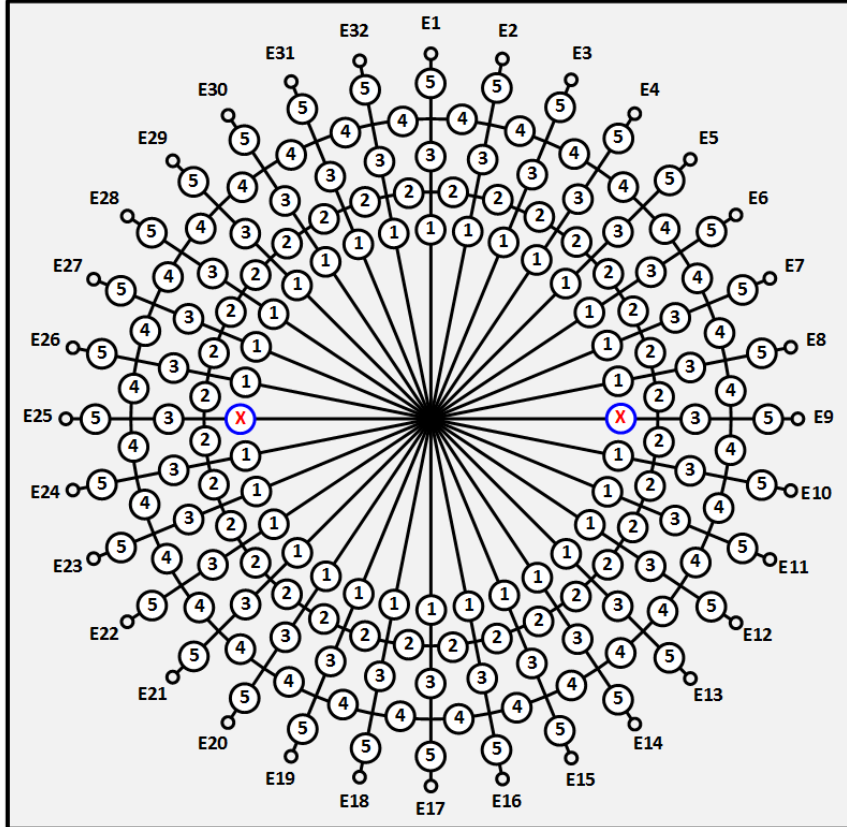


Figure 2.13: (a) Generation of an EIT differential image using a physical phantom (b) EIT resistive phantom [50] used for evolution. Resistive element ⑤=100 Ω , ④=196 Ω , ③=63.4 Ω , ②=6.34 Ω , ①=68.1 Ω .

The resistive phantom serves the same purpose as a physical phantom only is made of a network of resistive (or possibly capacitive) elements to approximate a continuous homogeneous medium. The generation of such phantom models is based on the analogy between FEM and the matrix method for solving electrical circuits [51]. On applying a current through a pair of electrodes the resistive phantom can provide stable and reproducible voltage signals at other electrodes with realistic frequency content and amplitude ranges [52] and the inner impedance re-distribution is caused

by making changes to specific variable elements during differential imaging. In terms of physical representation, it can be seen as impedance variation due to e.g. lung respiration.

A 32-electrode resistive phantom for general thorax EIT application [50] as shown in Figure 2.13 (b) is used for evaluation in this work. The phantom has electrodes evenly distributed around its circumference. Each numbered small circle represent a single resistive element, with five different resistances used. The resistive element marked by an X is the variable element.

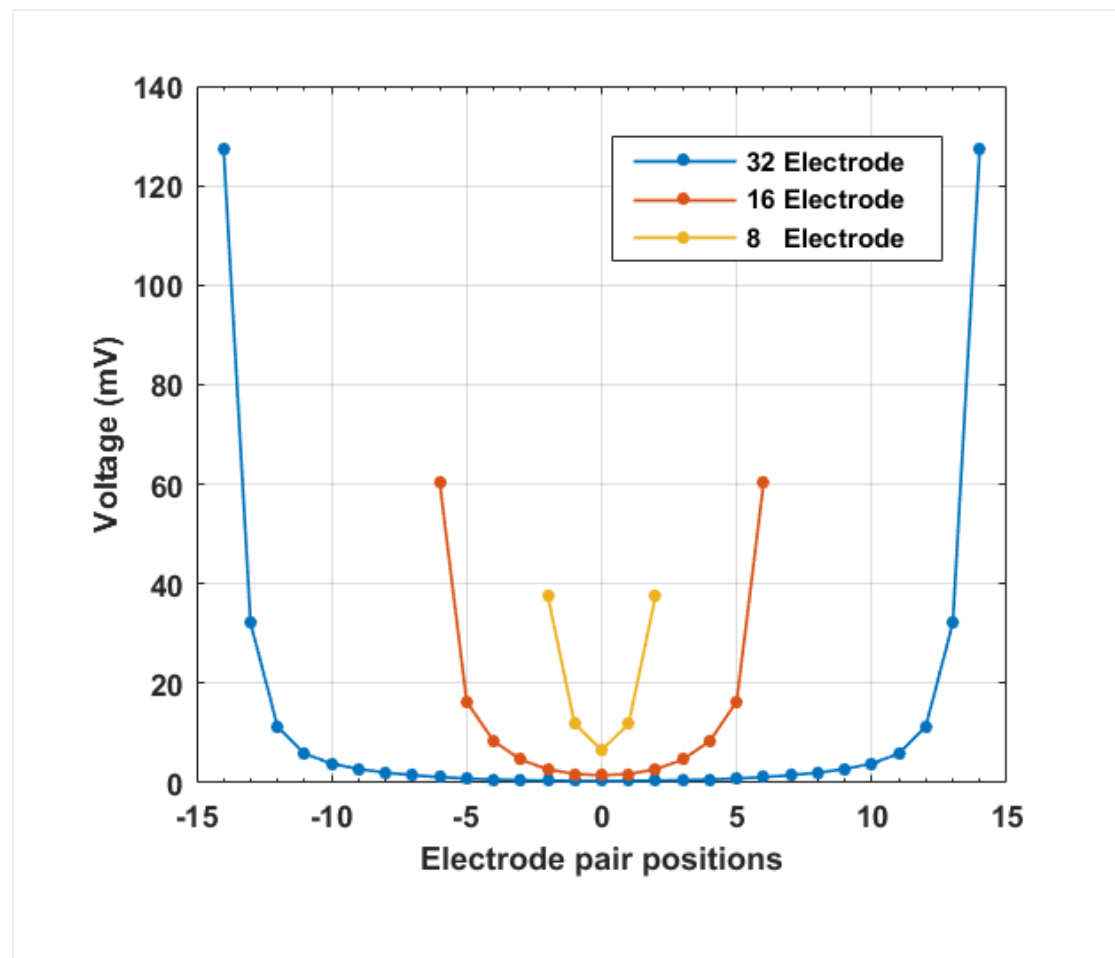


Figure 2.14: Voltage distribution measured from the resistive phantom using ideal components with 8, 16 and 32 electrode configurations excluding voltages on injection electrodes. The differential voltage pair position opposite the injection pair is marked as position zero for plotting purposes.

When $R_x = R_1 = 68.1 \Omega$, the phantom is homogeneous which is the condition often used to demonstrate EIT voltage patterns. To better illustrate the unique EIT

voltage patterns, the phantom is tested with a current of 8 mA_{rms} injected between E1 and E2 at 100 kHz , and because the phantom is only resistive, frequency selection is irrelevant to the results. The differential voltage measurements start from E3-E4 and ends at E31-32 excluding injection electrodes according to adjacent EIT scanning system (see Figure 2.2). With two or four electrode steps, 16 or 8 electrode voltage patterns can also be recorded for comparison. The voltage patterns are plotted in Figure 2.14.

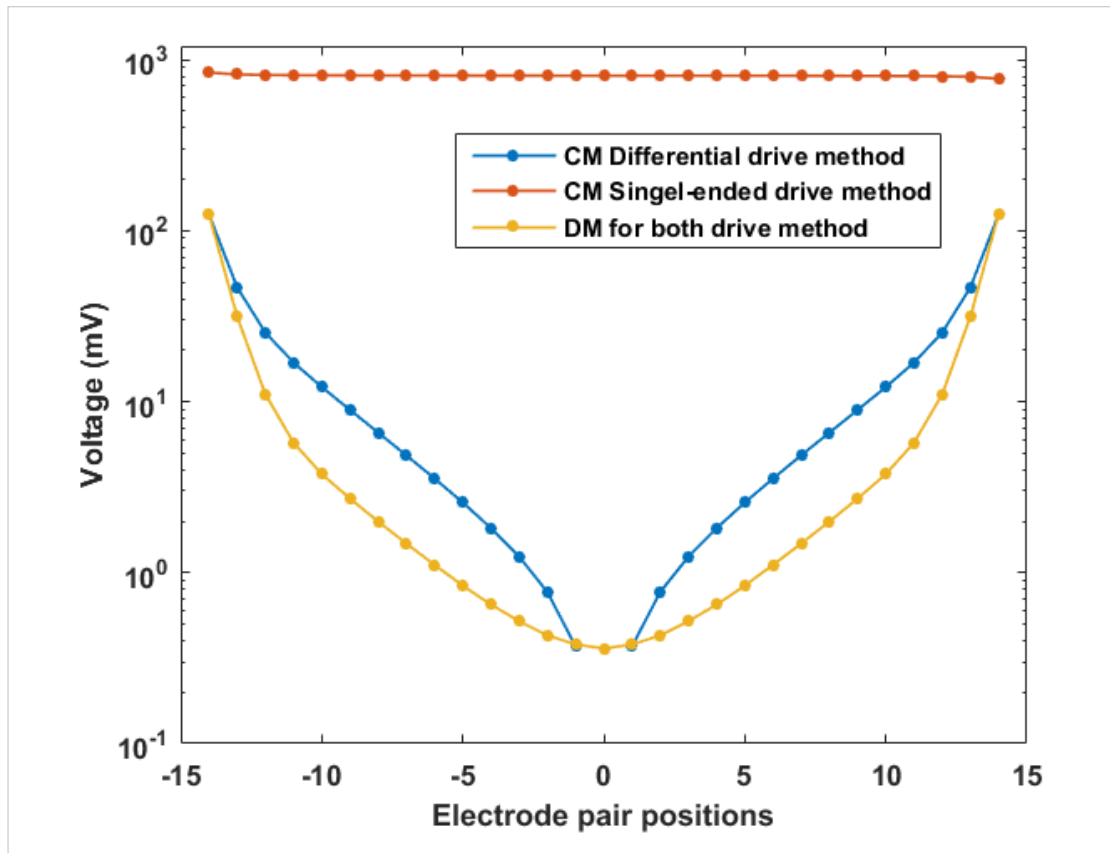


Figure 2.15: Comparison of amplitude of the CM (common-mode) voltage at different electrode recording positions when applying single-ended and differential current drive methods with the DM (differential-mode) voltage outputs.

Because most of the current injected into the SUT concentrates around its injecting location, the voltage amplitude drops as the electrode moves away from the injection point. As a result, a 'U' shaped voltage pattern is recorded. The dynamic changes in the voltage amplitude becomes larger as the number of electrode increase. For comparison, one can measure the dynamic range as $20 \cdot \log_{10} \frac{V_{max}}{V_{min}}$, and it results in

15 dB, 32 dB and 51 dB for 8 to 32 electrodes respectively. Thus, although higher electrode counts give more information, more stringent hardware specifications such as a lower noise, wider input linear-range, and wider dynamic gain are required.

The other critical specification for the voltage measurement is the CMRR. As shown in Figure 2.13, the IA measures the voltage difference between two electrodes. Therefore, any existing CM should be rejected by the IA CMRR. As mentioned in the section 2.3.2.1, the CM amplitude depends on how the current drive is managed (single or differential injection).

Considering the 32-electrode case, the common-mode and differential-mode voltages are plotted in Figure 2.15. The Y-axis is plotted in logarithmic scale to better illustrate the difference. As shown with single-ended current injection, the CM voltage remains at around 800 mV while the DM voltage drops to below 500 μ V. As a result, the IA would require a CMRR of at least 107 dB to maintain $< 1\%$ measurement error (which is also suggested as in [53], [54]). When ideal differential current injection is implemented, the CM shown in blue in Figure 2.15, it follows a similar decreasing pattern as the DM voltage, and more importantly, the CM is zero while the DM is at its lowest value and significantly relaxes the CMRR requirement. However, non-ideal differential current driver [55], unbalanced electrode impedance and the neither well-defined nor homogeneous characteristic of the bio-SUT [56] continues to raise the demand of IA CMRR and 80 dB is often targeted in many literatures [57]–[60].

In summary, a larger number of electrodes provides more independent voltages and leads to increased EIT measurement quality, but often poses hardware challenges. It also increases the time taken to complete a full EIT scan which limits the available rate of change in real-time imaging. Other issues such as the size and cost of the hardware set a limit on the maximum number of electrodes that can be used in an EIT system. The commonly used number of electrodes is from 8 to 32 depending on the application. Also the design of a voltage measurement front-end should not only consider CMRR, low noise, and wide measurement dynamic range, but also take

system architecture into consideration such as the number of electrodes required and the current drive arrangement.

2.3.3 EIT system architecture

A typical an EIT system can be divided into three parts, the electrode-SUT interface, the central hub and the back-end processing unit. The electrode-SUT interface is the array of electrodes for connecting the hardware to the SUT. The central hub usually contains most of the electronics for EIT operational control. The back-end e.g. a laptop computer or dedicated digital signal processing (DSP) unit is responsible for data processing. In thorax or other imaging EIT systems, the back-end collects the data and applies the image reconstruction software to produce and display the image. For the HMI EIT, the back-end can be a data classifier e.g. an artificial network which firstly learns the features and pattern in the data sets and then is able to classify hand gestures.

The electronics consists of two functional blocks, the current injection and the voltage acquisition. Depending on how the electronics is arranged between the electrode-SUT interface and the central hub, the system architecture is classified as using passive or active electrode systems.

2.3.3.1 Passive vs active architecture

In passive EIT systems, the hub to electrode-SUT interface only contains cable links. All the electronic is implemented in the central hub some distance away from the electrodes. The circuit connection to electrodes are made through complex cables and switching networks.

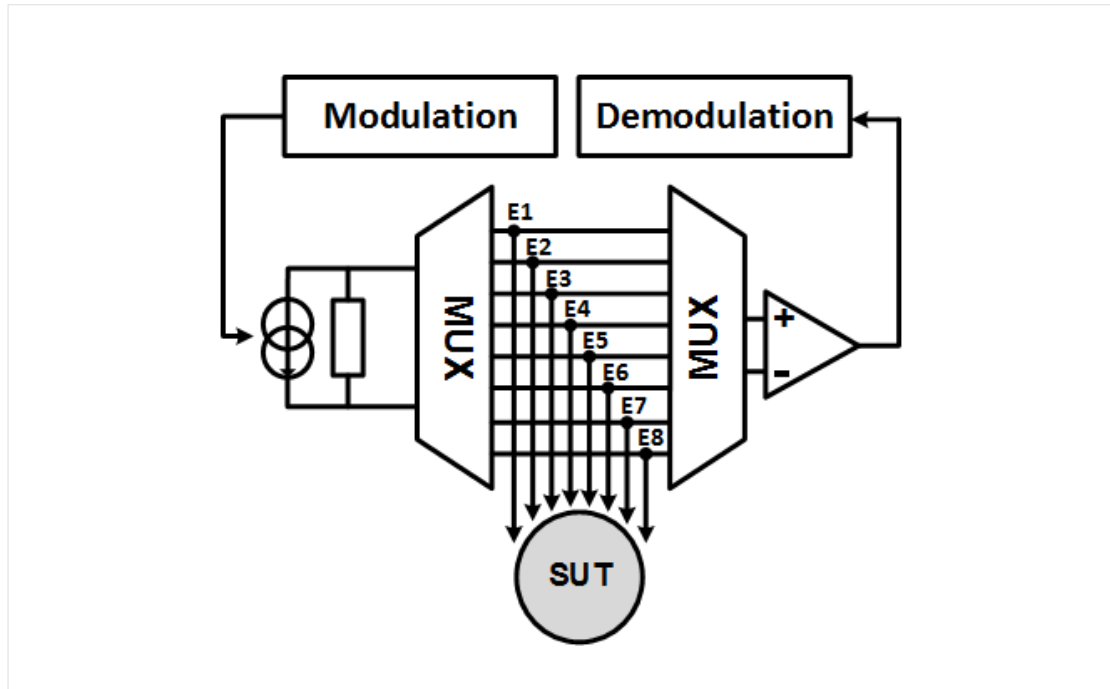


Figure 2.16: Passive 8 electrode EIT system architecture.

A typical passive EIT system architecture is shown in Figure 2.16. The system consists of the signal modulation unit which generates a voltage signal for current excitation and also receives the recorded voltages from the recording front-end for signal demodulation as described in section 2.3.1.2. The key issue with this type of arrangement is the severe parasitic capacitance effect attributed from cables and switches. The parasitic capacitance due to typically one-meter length cables can be from 50 to 200 pF and switching networks could also contribute ~20 pF.

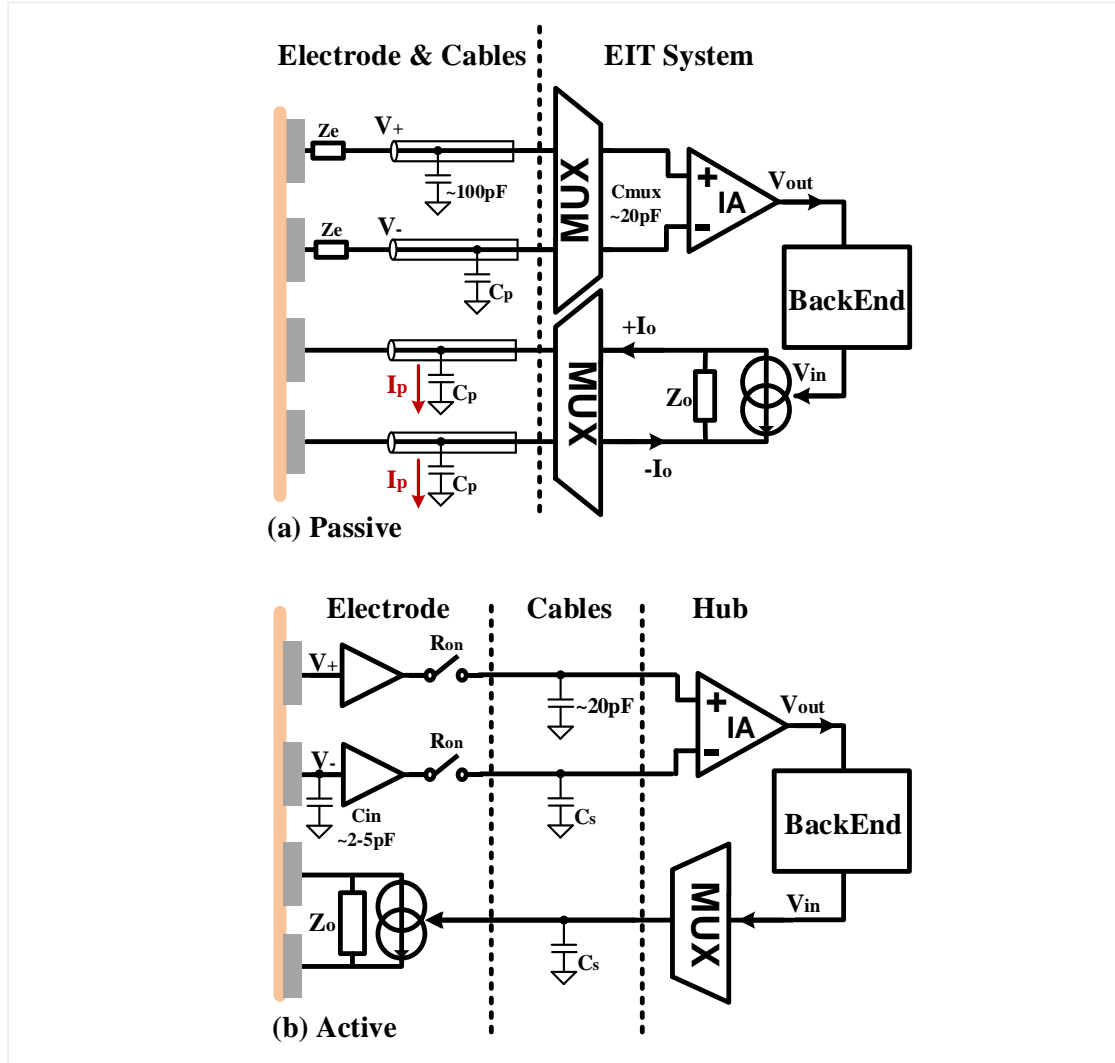


Figure 2.17: Difference between active and passive EIT systems, Z_e is the contact electrode impedance, and C_p is the cable parasitic capacitance with shielding and C_s is the FPC track parasitic capacitance without shielding, C_{mux} is the switch parasitic capacitance.

As discussed in section 2.3.2.1, for current injection, the value of parasitic capacitance C_p should be as small as possible. For voltage measurement as shown in Figure 2.17(a), the passive arrangement has a significant length of cable with associated capacitance C_p between the IA and the high output impedance (due to Z_e) signal source. The electrode contact impedance Z_e and the parasitic capacitance C_p form an R-C filter that lowers the input impedance of the IA.

This signal attenuation effect varies as both R and C values are not well defined and can vary due to movement or electrode-skin conditions. This further degrades the

system CMRR [61]. Furthermore, this high-impedance line is more susceptible to cross-talk and interference, and shielding is required [62]-[63]. To reduce the parasitic double shielding and active shield boot strapping are required, but such additional implementation is liable to cause instabilities in the system [64] and the thick shielded cables further lack flexibility to allow the belt to be in intimate contact with the SUT. To resolve this problem, active electrodes were suggested for EIT in [65], and [66].

As shown in Figure 2.17(b), the voltage controlled current driver and voltage buffer are placed in direct contact with the electrodes and the unwanted parasitic effect can be greatly reduced at the electrode circuit interface. For the current driver, the cable only carries a well-defined excitation signal to the driver's input, while the parasitic capacitance at the driver's output is minimised. For electrode voltage measurement the inserted buffer provides a high and stable input impedance with a small input capacitance C_{in} . At the same time, the buffer has a low output impedance which is in series with a switch whose on-resistance R_{on} , is small, so that the resultant RC filter effect is negligible. The results in [67] suggested that active buffer is less sensitive to contact impedance variation by one order of magnitude. And because of the low impedance line, shielding is no longer required, so that the cable can be managed in a more flexible and compact fashion.

2.3.3.2 Serial vs parallel architecture

In most of the EIT systems, there is only one current driver and one voltage acquisition device located in the central hub. This is referred to as a serial system. Such a system is simple and easy to build, but as shown in Figure 2.2, each voltage measurement within an EIT scan is taken Δt later than the previous one. This means, there may be a significant delay from measurement to measurement in a data set that is used to represent the inner conductivity distribution of the SUT at a single moment in time. This could cause image artefacts if rapid physiological changes happen in the SUT.

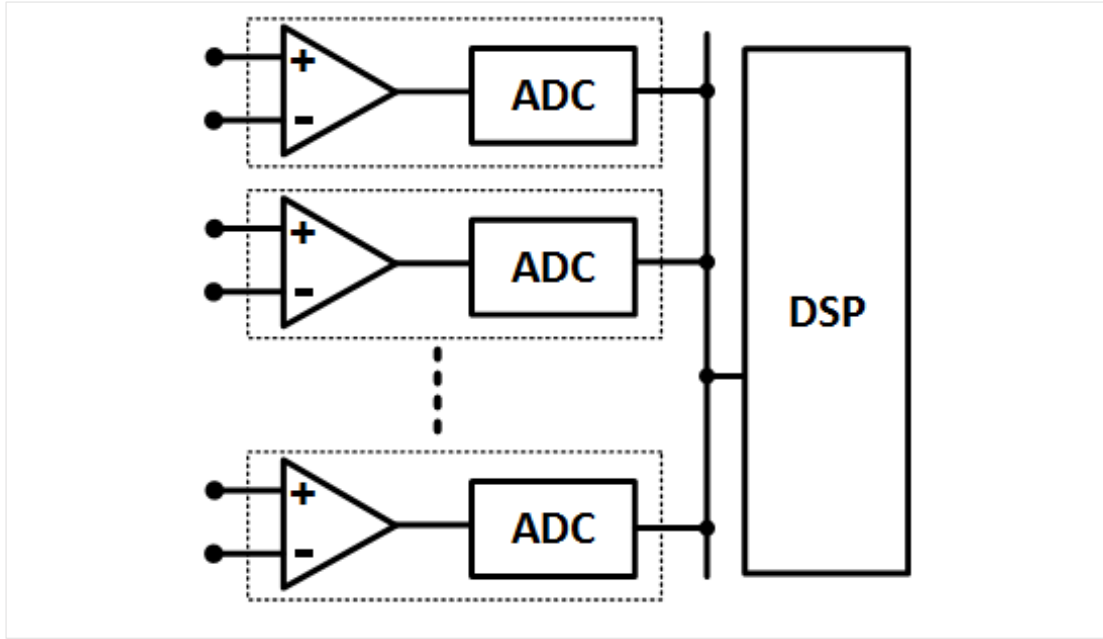


Figure 2.18: EIT system architecture with parallel voltage acquisition.

In Figure 2.18, a system architecture with parallel voltage acquisitions is shown. All the voltage data can be measured simultaneously within a current rotation cycle. The EIT scanning speed is also referred as the image fps which can be defined as:

$$FPS = \frac{1}{T_{total}} = \frac{1}{\frac{\delta t * E_N^2}{N}} \quad (2.10)$$

where T_{total} is the total time required to produce an image, and δt is time required per voltage recording, E_N is the number of electrodes in the system, and N is number of parallel channels.

High frame rate (> 100 fps) is not only more suitable for monitoring neonates whose breathing is twice as fast as adults, but also can capture rapid physiological changes e.g., during high-frequency oscillatory ventilation. However, the parallel system is complex to implement and requires calibration.

2.3.3.3 Other useful system functionalities for thorax EIT

- *Heart rate and breath rate monitoring:*

For the neonatal thorax EIT, the pre-term babies targeted are often ill and under mechanical ventilation in the intensive care unit. Thus, there will be other additional

vital sign monitoring devices, especially the ECG (electrocardiogram) heart-rate and breath rate monitoring. Because the babies have small chest circumferences, integration of such functionalities in a single system in the compact fashion will make EIT more accurate and attractive to clinical practices.

- *Positioning and torso shape tracking:*

Belt position is important because it is common practice for nurses to rotate the babies in the chamber, and with different lying positions, and due to gravity, the lung moves inside the chest. Thus, the lying position should also be recorded and taken into consideration for image reconstruction.

Regarding to the image reconstruction, conventionally, a single representative boundary model is obtained from CT scans and used for all patients. This one-size-fits-all practice can lead to image artefacts [68]. This artefact is shown in Figure 2.19. These EIT images intend to show the lung region with full inhalation. The blue areas are the higher impedance region due to lung inflation. As the accuracy of the FEM model is based on the boundary condition of the SUT (i.e. the shape of the chest), the lung regions are clearly shown in the bottom right image where the same boundary condition applies. Using the same data set, other three images are created but each with a lesser accurate boundary shape. As shown, the EIT images become more distorted and finally lose the lung region in the top left image. From that, it can be concluded that the patient-specific shape information should be recorded and incorporated into creating the FEM model. This can minimise the error artefacts in the reconstructed images and improve the image accuracy [69].

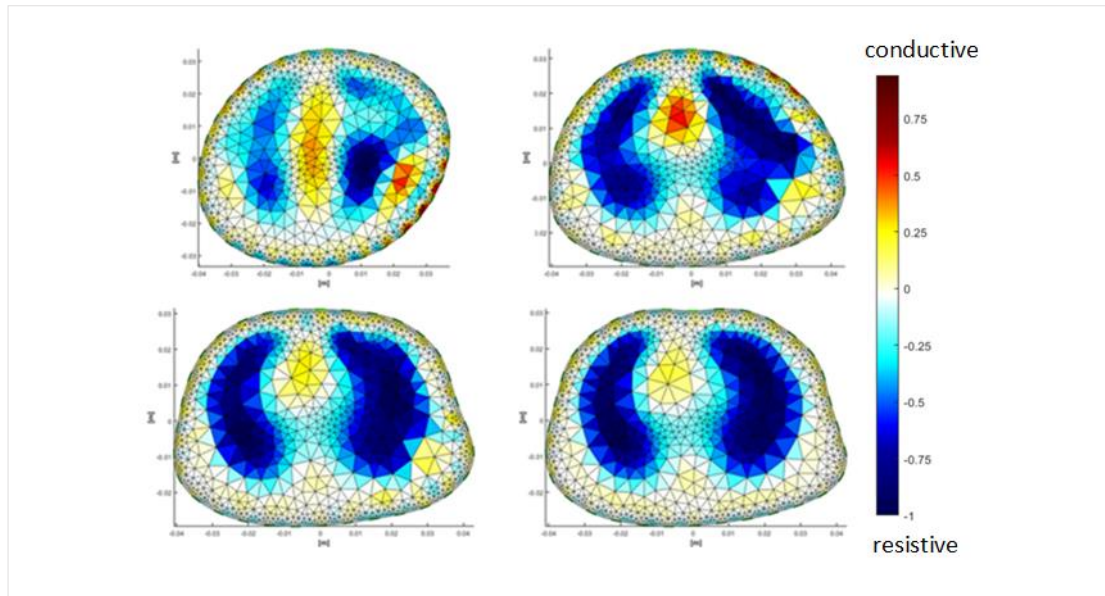


Figure 2.19: Reconstructed EIT images using the same set of data but different boundary conditions to illustrate that an accurate torso shape model can significantly improve the quality of lung EIT images [69].

2.4 Systems for biomedical EIT - A review

2.4.1 Passive EIT system for thorax EIT

The KHU Mark-2 [70] is a superior passive EIT system as shown in Figure 2.20(a). The system uses 16 electrodes with digital I-Q demodulation approaches achieving a bandwidth of 500 kHz. The advantage of the Mark-2 is that it uses a fully parallel system architecture to achieve a fast measurement frame-rate of 100 fps. Compare to serial architecture, Mark-2, uses many impedance measurement modules (IMM). The IMM can be seen as a fully integrated bio-impedance measuring device that can practice excitation as well as recording independently. This means that it can directly drive each cable and electrode without the need of switch networks.

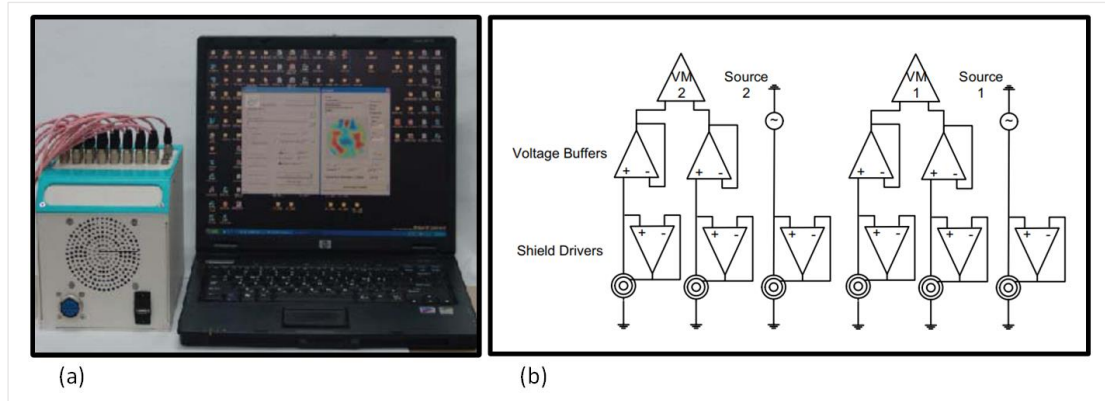


Figure 2.20: (a) EIT system KHU Mark-2 (b) Simplified circuit system implementation [70].

For the analog front-end circuit design and implementation, the simplified schematic of the IMM is shown in Figure 2.20(b). The current injection is based on a Howland current driver [71] as shown in Figure 2.21.

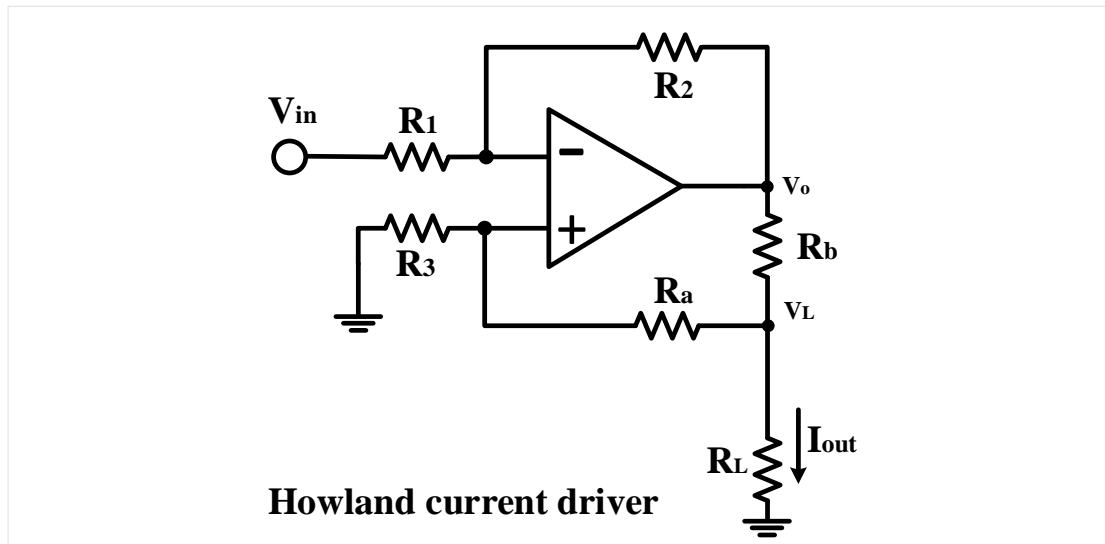


Figure 2.21: Howland current driver.

The output current of the circuit can be derived as:

$$I_{out} = \frac{V_L}{R_b} \left(\frac{R_2}{R_1} - \frac{R_a + R_b}{R_3} \right) - \frac{R_2 \cdot V_{in}}{R_1 \cdot R_b} \quad (2.11)$$

where $V_L = V_- = V_+$ and if $\frac{R_1}{R_2} = \frac{R_a + R_b}{R_3}$:

$$G_m = \frac{I_{out}}{V_{in}} = \frac{1}{R_b} \quad (2.12)$$

The output impedance of the circuit can be derived as:

$$Z_o = \frac{R_b \left(1 + \frac{R_a}{R_3}\right)}{\frac{R_2}{R_1} - \frac{R_a + R_b}{R_3}} \quad (2.13)$$

and if $\frac{R_1}{R_2} = \frac{R_a + R_b}{R_3}$, then Z_o becomes infinitely large. However, such condition is difficult to achieve due to resistor mismatches. In addition, the circuit performance also relates to the performance of the operational amplifier (opamp) e.g. finite opamp open loop gain as detailed in [72].

In addition, due to its parallel structure, intensive calibration is required for the system to achieve a good performance [73]. Implemented at discrete level, not to mention the extra complexity and cost, the size of the IMMs make it impossible to be further integrated on to the electrode-SUT interface. Thus, cables are still needed to connect the hub to the electrodes and the shield drivers must be used.

After KHU Mark-2, a commercial product based on the passive system architecture known as the Dräger system [74] became available for adult thorax application on the same year. The system is as shown in Figure 2.22(a), based on in [74], it is suggested that the Dräger uses serial passive EIT system architecture achieving a bandwidth of 130 kHz and a frame rate of 30 fps. The highlight of the system is its commercialised electrode-SUT interface which is made into a form of wearable belt. However, for neonatal applications, such a belt is not available. Thus, in EIT clinical trials, the cable based passive electrode-SUT interface are placed on babies for lung function monitoring [75]-[76] as shown in Figure 2.22(b). As a result, there are limited usage of EIT in clinical applications with such impractical ways of electrode installation. Even with a miniaturised version of the Dräger belt, the silicon electrode with snap button is still considered unsuitable for long term monitoring because its non-permeable nature provokes skin irritation.

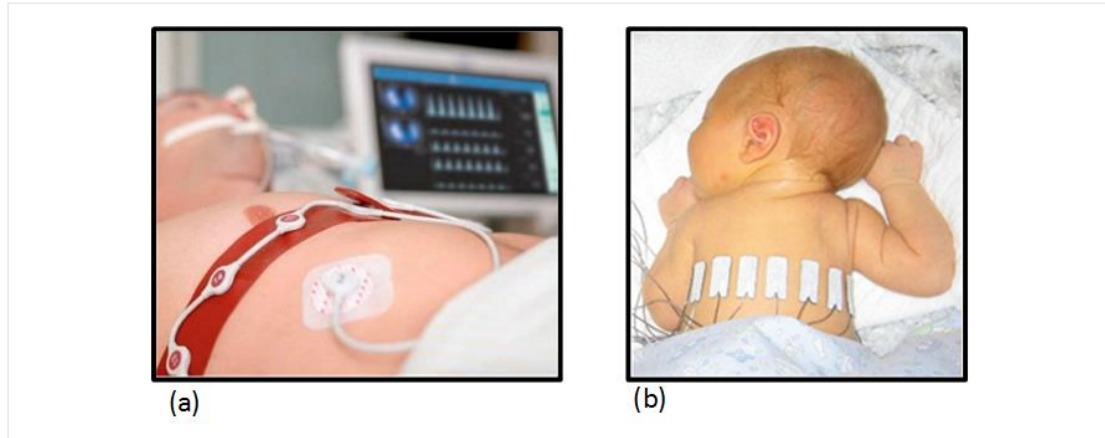


Figure 2.22: (a) The Dräger system [74] (b) apply passive EIT system in clinical neonatal thorax application [76].

2.4.2 Active EIT systems for thorax EIT

Although some of the more recognizable systems have gone through several updates [70], [77], [78], EIT is still not ready for daily clinical practice due to image qualities affected by limitations in the hardware as well as stray capacitance degradation caused by the impractical electrode-SUT interfaces as discussed in section 2.3.3.1. In pursuing better EIT performance as well as more comfortable and functional electrode-SUT interfaces, active electrodes and wearable belts have become popular.

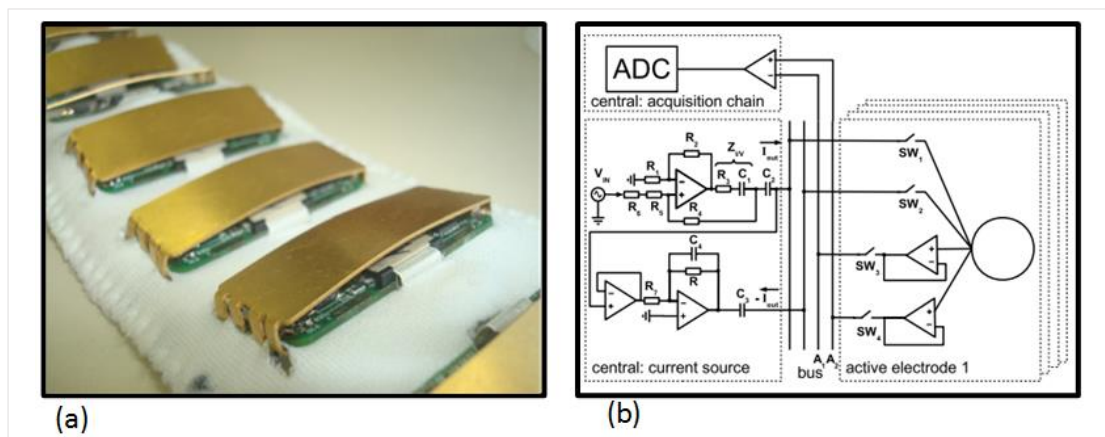


Figure 2.23: (a) active electrode on the wearable belt. (b) The active electrode system architecture [67].

The first wearable EIT system that uses 32 active electrodes is reported in [67] as shown in Figure 2.23. It has incorporated active electrodes by integrating voltage buffers onto the electrodes. The large parasitic capacitances are isolated to the output of the active buffer as shown in Figure 2.17. As a result, the cable and shielding in passive system is no longer required and a compact wearable belt can be implemented. The system uses digital I-Q demodulation and achieves a bandwidth of 200 kHz with 30 fps. However, it can be seen that compared to the ideal active electrode topology shown in Figure 2.17, the current source (current driver) of the system is still placed in the hub. This is due to the challenges in integrating multiple Howland current drivers at the electrodes, because of the resistor matching issue, and the active electrode size limitations. Due to a large parasitic capacitance, high output impedance of a central current driver cannot be maintained at high frequencies. This not only results in variable output current which decreases the measurement accuracy, and the system operating bandwidth.

To minimize noise and improve hardware performance while keeping the size small, ASIC are suggested for active EIT systems. Figure 2.24 shows an EIT system implemented using an ASIC. Given the advantages in using CMOS designs, many circuit functions can be integrated into a single chip. This chip forms a system-on-chip (SoC) ASIC that can be bonded onto a wearable belt. Despite offering certain advantages such as low-power and good compatibility, as a design trade-off, this work employs a full analog approach for I-Q signal generation and demodulation. Operating 16 electrode with 6 parallel read-out channels, the system only achieves 20 fps. For the analog front-end, the V/I converter employs an open-loop topology which has limited bandwidth and output impedance. For voltage recording, without active buffer, acquisition channel still may suffer from the parasitic effect described earlier as the electrodes are still some distance from the core electronics.

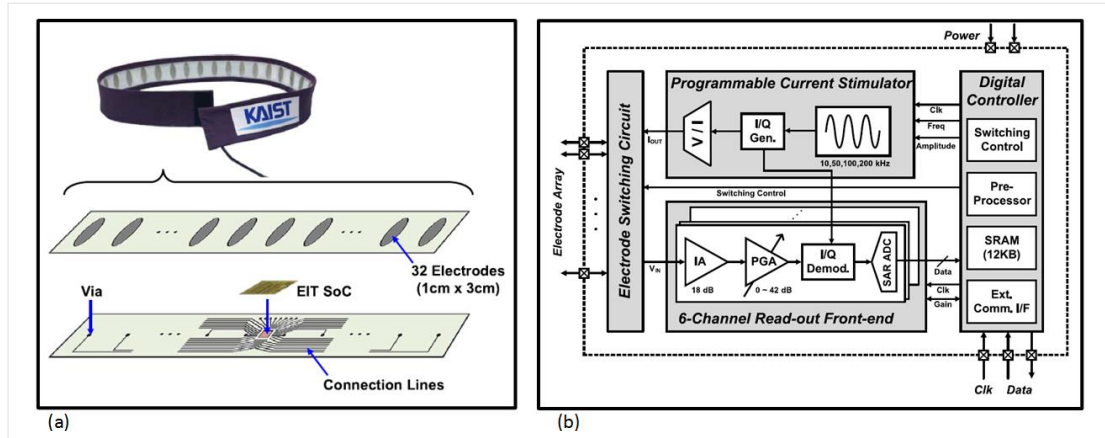


Figure 2.24: (a) Active belt assembly (b) ASIC system on chip architecture [79].

Another commercial device is shown in Figure 2.25 [13]. Based on the information given, it has system topology similar to [67] but ASIC are used inside its wearable belt. This commercial device is capable operating at 150 kHz with a frame rate of 50 fps. It also introduced a more clinical friendly electrode-SUT interface. It is in the form of a wearable belt based on silver-coated conductive textile fabrics which are considered suitable for neonatal thorax applications.

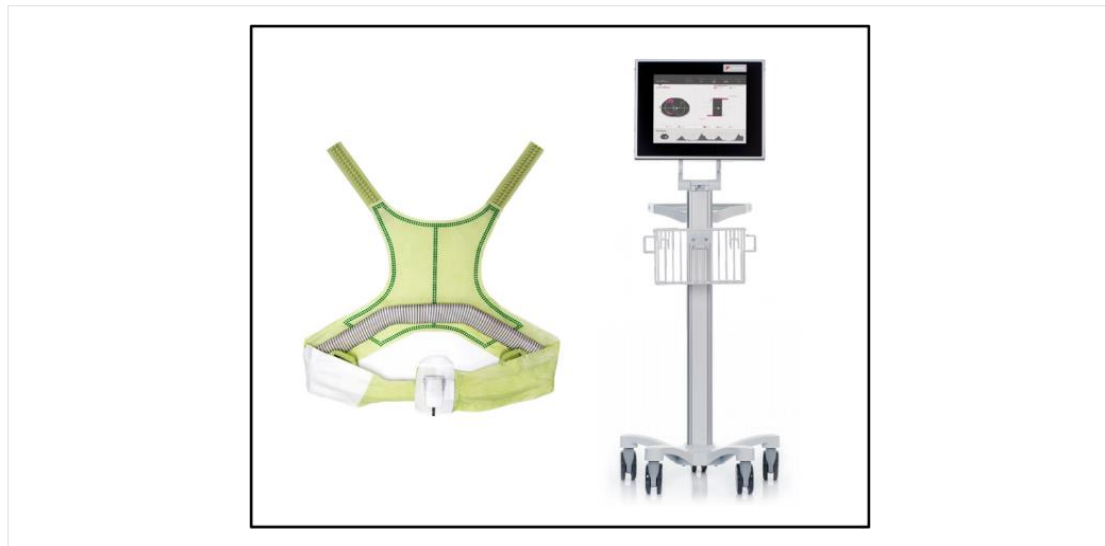


Figure 2.25: The Swisstom BB² system [13].

At the time of writing, two wearable EIT systems for thorax application have been reported. The first is shown in Figure 2.26 [80], its main EIT hardware implementation

is based on the KHU Mark-2, but also features other vital sign monitoring, such as ECG, and peripheral capillary oxygen saturation (SpO₂).

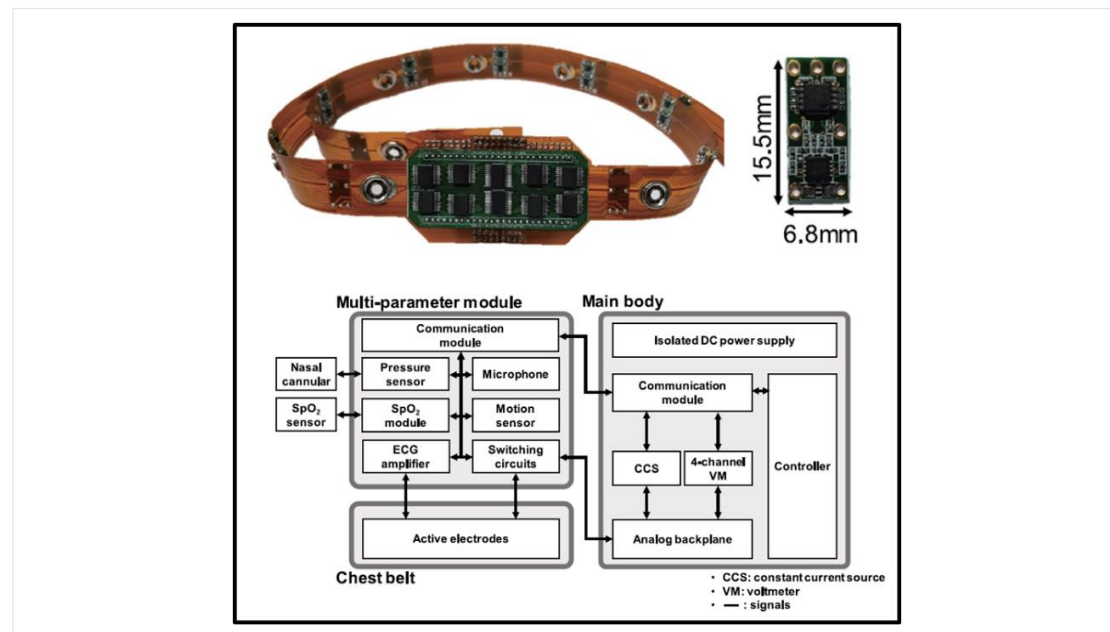


Figure 2.26: KHU multi-functional wearable EIT device [80].

The system has been redesigned to feature active electrodes. The active electrode is implemented on a small printed circuit board (PCB) which is mounted on a large flexible PCB. The active topology is similar to [67], where voltage buffers are placed at the electrode. It is reported that with 3 meters of cabling, the voltage acquisition maintains a constant SNR which would otherwise drop by 16 dB without the active buffers. While adding active electrode to enhance system performance and other useful clinical functions, compared to KHU Mark-2, the design focuses on clinical feasibility and EIT system performance. As a result, it can be seen that the parallel modules are reduced from 16 to only 4 in the main body, and the EIT operating frequency has been reduced to 11.25 kHz with a lower frame rate of 25 fps.

The second active electrode EIT system [81] is based on a different design concept called frequency division. The sensor is called a cooperative sensor which consists of voltage and current sensors. As the name suggests, the two type of sensors works cooperatively. Compared to other EIT systems, where there is one excitation

signal, this system has n signals (n is the total number of each I and V sensors). When $n=25$, dc plus 12 ac signals are generated and each signal is 80 Hz apart.

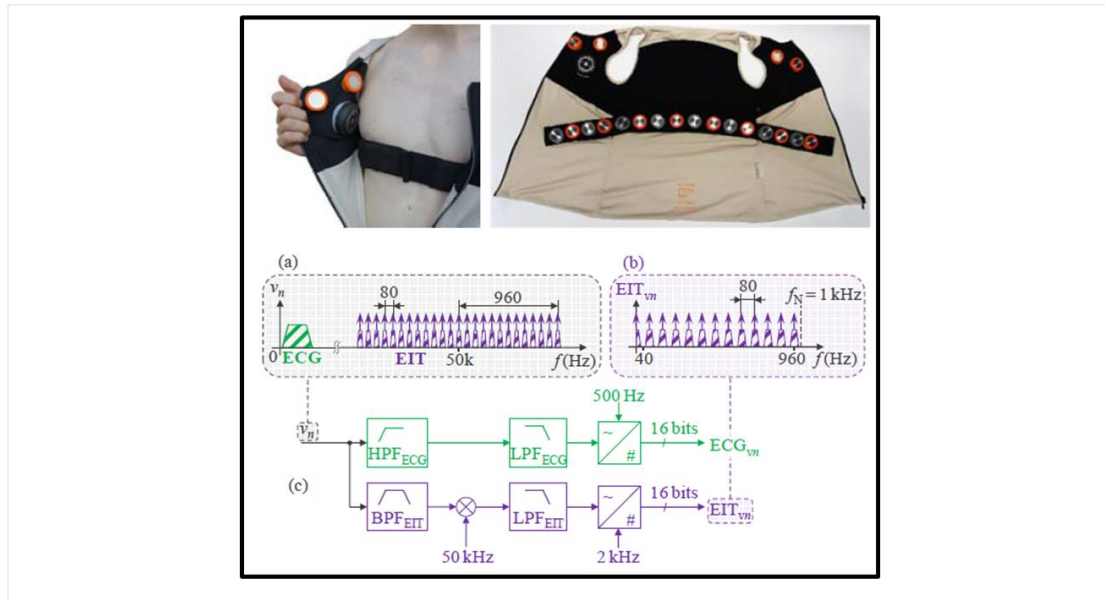


Figure 2.27 Cooperative sensors for EIT with frequency division [81].

All the signals are modulated with a carrier of 50 kHz, and 25 signals are injected into the SUT simultaneously. Each I-type sensor injects two frequencies (source or sink current). Figure 2.27(a) shows the ECG and the other 25 EIT signals measured by V type sensors. All the V-type sensors record the whole 25 EIT signals, and through demodulation each frequency component can be associated with the injection point based on frequency division. This is not only parallel recording but also parallel excitation, therefore, the measurement is done simultaneously without any EIT rotations as it has already been done in terms of frequency. It can be seen that there are no measurement delays. However, the signals are no longer at one exact frequency as each is separated by 80 Hz. It can be argued that even though tissue impedance is frequency dependent, 80 Hz will cause little measurement difference. One advantage of frequency division is that the control signals are sent at around 2 MHz sharing same line with the analog signal. This significantly reduces the wirings interconnection to only two.

However, in the paper, the final implementation is 8 electrodes instead of 25, which reveals the inherent complexity with this architecture. Even if ASIC could offer more integration and smaller size, given that other state-of-the-art EIT systems is capable of high frames, it is not certain that such complex architecture offers much merit.

2.4.3 EIT in human-machine interface

For this new application for EIT there are only two systems reported in the literature [22], [23]. In terms of the hardware implementation, the system reported in [22] is largely based on the AD5933, (a commercial bio-impedance analyser integrated circuit using two-electrode measurements by Analog Devices) which is not very suitable for EIT measurement.

Although as shown in Figure 2.28, an advanced version [23] is implemented using a four-electrode measurement scheme, it still employs a single-ended current driver that produces large common-mode voltages. Moreover, for simplicity, the system adapting AD5933 as a DDS, which leads to only the magnitude demodulation (see section 2.3.1.2). The system features a low-cost wearable device for proof of concept and several hardware improvements are possible providing a more robust EIT system for this application.

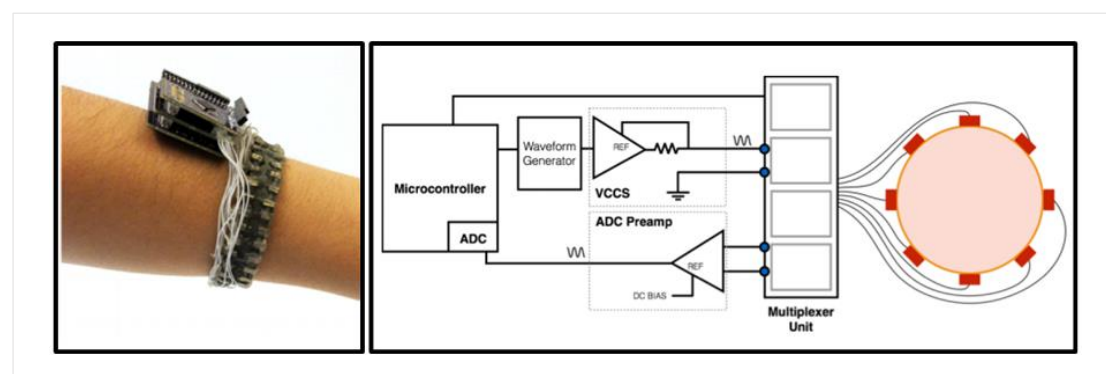


Figure 2.28: A wearable EIT for hand gesture recognition in [23].

2.4.4 Summary

In this section, a detailed review is given including both targeted thorax and HMI applications, and covers both passive and active EIT systems along with two commercial thorax EIT devices. It covers system architecture, circuit design, and electrode-SUT interfaces, all to provide benchmarks towards defining specifications for EIT systems in this work.

Following many years of research, numerous prototypes can be found in the literature, and in this section some of the standard systems together with several update versions as well as state-of-the-art EIT systems are summarised in Table 2-1. From Table 2-1, certain trends can be recognised. Firstly, the modern EIT system specification is set according to the application. Secondly, active electronics are becoming the mainstream with an increasing need for wider bandwidth as well as a higher frame rate, and finally, EIT system is trending towards a compact wearable device.

For neonate lung respiration monitoring, it is identified that at least 16-electrodes are required to gather adequate measurements for imaging, and active electrodes should be used to achieve better noise-performance, higher common-mode suppression, 1 MHz bandwidth, and >100 fps as well as multi-functionalities with smaller size requirements.

For HMI application, the aim is to investigate the potential of EIT for prosthesis hand control and identify possible further hardware development. Without the need of producing an image as a way of interpreting the data, 8-electrodes with moderate bandwidth and frame rate are targeted as the starting point. Also, given that the arm circumference is even smaller than the average neonatal chest size, the implementation of active electrodes may be impractical due to size limitations even with ASIC, thus for this application, towards a SoC approach is pursued.

With the benefit of fast operation, precise controls and flexible adjustability, the digital I-Q demodulation method is dominantly used in modern EIT systems. As a result, it is also the approach selected for all systems implemented in this work.

With this review, the specifications for the targeted systems are listed in Table 2-1 along with the analog front-end specifications listed in Table 2-2 and Table 2-3.

Table 2-1: Summary of the major EIT systems reported in the literature with systems specification proposed in this work.

Years & Ref	Names	# of <i>Ele</i>	Type ¹	Bandwidth	Acquisition	FPS ²	Demodulation	<i>Ele</i> interface	Application	Notes
2001-[77]	Sheffield Mk 3.5	8	Passive	1.6 MHz	Parallel	25	Digital FFT	Cables	General	-
2006-[78]	UCLH Mk 2.5	32	Passive	256 kHz	Serial	<1	Digital I-Q	Cables	Brain	-
2011-[70]	KHU Mk 2	16	Passive	500 kHz	Parallel	100	Digital I-Q	Cables	General	-
2011-[74]	Gräger	16	Passive	130 kHz	Serial	30	-	Wearable	Thorax	Commercial
2012-[67]	Gaggero et al	32	Active	200 kHz	Serial	30	Digital I-Q	Wearable	Thorax	1 st wearable active EIT
2015-[79]	KAIST	32	Active	200 kHz	Parallel	20	Analog I-Q	Wearable	Thorax	SoC solution
2015-[13]	Swisstom	32	Active	150 kHz	-	50	Digital I-Q	Wearable	Thorax	Commercial
2016-[82]	Santos et al	16	Passive	960 kHz	Serial	131	Digital I-Q	Wearable	Thorax	High speed, wide bandwidth
2016-[23]	Tomo-2 nd Gen	8-32	Active	100 kHz	Serial	87-3	Digital Mag ³	Wearable	HMI	-
2018-[80]	KHU wearable	16	Active	11.25 kHz	Parallel	25	Digital I-Q	Wearable	Thorax	Multi-functional
2018-[81]	Co-op Sensor	8/8 ⁴	Active	50 kHz	Parallel	-	Digital I-Q	Wearable	Thorax	Frequency division
This work	CRADLvision	16/32	Active	Up to 1 MHz	-	>100	Digital I-Q	Wearable	Thorax	Multi-functional
This work	HMI EIT	8	Active	>100 kHz	-	10-15	Digital I-Q	Wearable	HMI	Prosthesis control

¹ System architecture type; ² complete frame scan per second; ³ Magnitude demodulation; ⁴ 8 current plus 8 voltage electrodes

Table 2-2: Specification for the current injection.

	Specification	Notes
Drive method	Differential-drive	To reduce common mode on induced voltages
Bandwidth	Up to 1 MHz	To investigate high frequency bio-impedance characteristics
Output impedance	$> 500 \text{ k}\Omega$	To maintain constant current at the operating frequency
Output current amplitude (mA)	$< 10mA_{rms}$	Safety compliance

Table 2-3: Specification for the voltage acquisition.

	Active buffer specification	IA specification	Notes
Gain	1 V/V	$\sim 10 \text{ V/V}$	-
Bandwidth	Up to 1 MHz	Up to 1 MHz	-
CMRR	-	Up to 80 dB	-
Input linear range	$\sim 3 \text{ Vpp}$	$> 150 \text{ mVpp}$	Active buffer measures single-end voltage, IA measures the differential voltage
Noise level	$< 100 \mu V_{rms}$		This is application dependent e.g. number of electrodes, current amplitude etc.

2.5 Conclusion

This chapter has firstly introduced the basic concept and operation of EIT. The characteristic of the tissues and electrode interface including its circuit model, contact impedance characteristic, and noise features are covered. The method for BIM is also introduced including the techniques used for bio-impedance extraction. Following the fundamentals in BIM, the importance of analog front-end in EIT is emphasised for both current injection and voltage acquisition. We have identified that the wideband is preferred for both injection and recording to reflect the frequency related response of the bio-tissues, and parasitic capacitance is to be minimised by all means to prevent measurement errors. Differential current injection is considered necessary for EIT to reduce the common-mode signal together with high CMRR IA to suppress common mode induced measurement error.

Different system architectures have been described and their advantages and disadvantages discussed, following a review of EIT systems reported from year 2001 to date. Other system functionalities are analysed towards better EIT image as well as clinical feasibilities.

Finally, circuit specifications for the analog front-end and EIT system specification for the targeted application have been proposed.

Chapter 3

Active electrode based EIT system for lung respiration monitoring

3.1 Introduction

In the last 30 years many EIT systems have been developed for general or targeted medical applications. Although some of the more recognizable systems have gone through several updates, EIT is still far from ready for daily clinical practice. Especially for infants born extremely preterm, a successful wearable bedside EIT system for lung function monitoring in daily clinical practice is still hampered by their limited functionality. To address this, a high specification wearable EIT system is described in this chapter. The main features of this 32-electrode EIT system (CRADLvision 1.0) are: 1) a wideband ASIC integrating both current injection and recordings circuits for active electrodes; 2) a high frame rate (107 fps); 3) disposable textile electrode dressing [83]; and 4) multi-sensing functionality (heart rate, near belt temperature and humidity sensing, and belt orientation for EIT model selection to aid image reconstruction).

The rest of the chapter is organized as follows. Section 3.2 describes the overall system design architecture, the digital control and signal processing blocks. Section 3.3 describes the ASIC for active electrodes comprising a linear feedback current driver and two analog buffer amplifiers. Section 3.4 presents the measured electrical performance of the ASIC as well as measurements with the 32-electrode wearable EIT system constructed using this ASIC. The system is compared with other work showing its superiority. Summary and remarks are presented in section 3.5.

3.2 System design and implementation

3.2.1 System architecture and design

The overview of the CRADLvision 1.0 EIT system is shown in Figure 3.1. It comprises a wearable flexible printed circuit board (FPC) belt covered by a textile dressing, a central hub which controls the 32 active electrodes on the belt, and a computer display to visualize the captured clinical parameters. The first prototype belt has been designed to fit an average adult for test and validation purposes and can then be miniaturized for neonate applications.

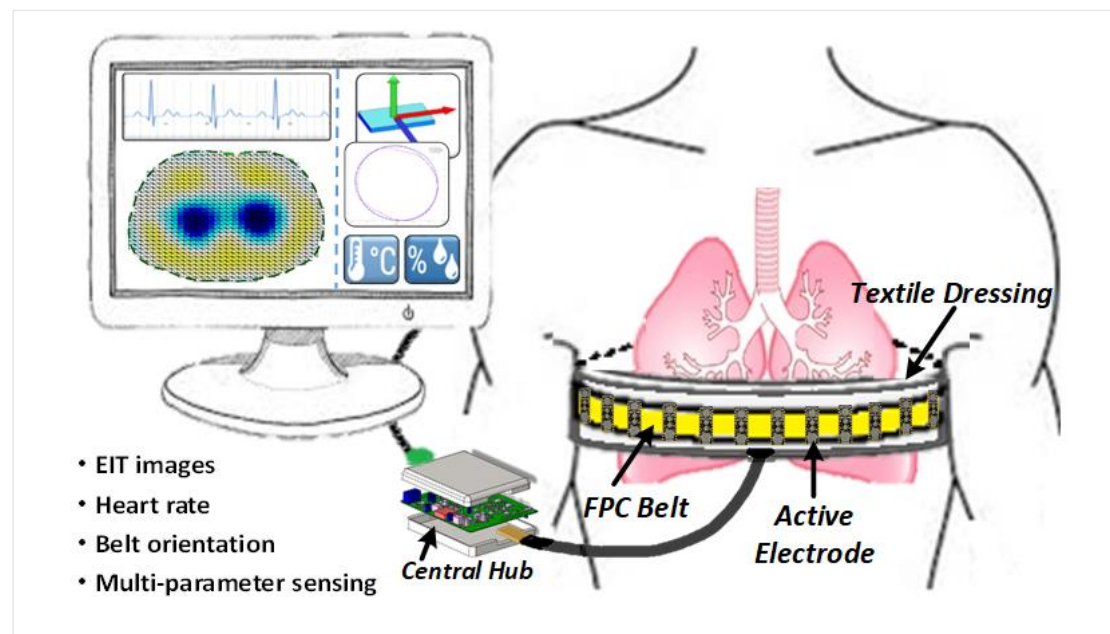


Figure 3.1: Wearable EIT lung respiration monitoring system with heart rate monitoring and other functions using active electrode ASIC.

Figure 3.2 shows the detailed system architecture. Each of the 32 ASICs comprises a current driver (CD), a main buffer (B1) for measuring EIT and heart rate signals, and a multi-sensor buffer (B2). The ASIC is mounted on an active electrode PCB together with two analog switches (S1: ADG1211; S2: ADG1213) and a digital CPLD (XC2C64A) to provide signal routing. The 32 active electrode PCBs are identical and share all the coloured analog paths shown in Figure 3.2 (e.g. VDC, VO4, VO3 etc.). The CPLD receives two daisy chains from the central hub. Sequentially, the first

chain configures the desired active electrode to current drive mode while the other puts the selected electrode into voltage sense mode. The CPLD shifts the digital control signal in daisy chain according to a user-defined scan pattern. This method allows the user to define injection or measurement EIT scan patterns independently.

In the example of Figure 3.2, the four active electrodes are configured into a typical tetra-polar (four electrode) bio-impedance measurement scheme. The top electrode is configured into current drive master-mode; CD in the ASIC is powered on, and the differential excitation signals VP and VN are connected to CD to generate the current I_+ . Buffer B1 is connected to the VF path to send back the injecting electrode voltage for current sink feedback. The bottom active electrode is configured into current drive slave-mode. In this mode, the electrode turns on the appropriate analog switch to provide a current return path for I_- to flow back to the central hub. The two middle active electrodes are configured to voltage sense mode where only B1 is functioning. The CPLD selectively connects the output of B1 to one of the four VO paths (VO1, VO2, VO3, VO4) to send the voltage signal back to the IAs in the central hub. There are two parallel recording channels in the central hub; each channel concurrently converts 16 of the 32 measured voltages into the digital domain for I-Q demodulation.

Sensors with a voltage output can be connected to buffer B2 that can be selectively powered by the CPLD. The powered-on B2 sends its sensor measurement back to the central hub through the VDC line. All modes of operation are explained in section 3.3.

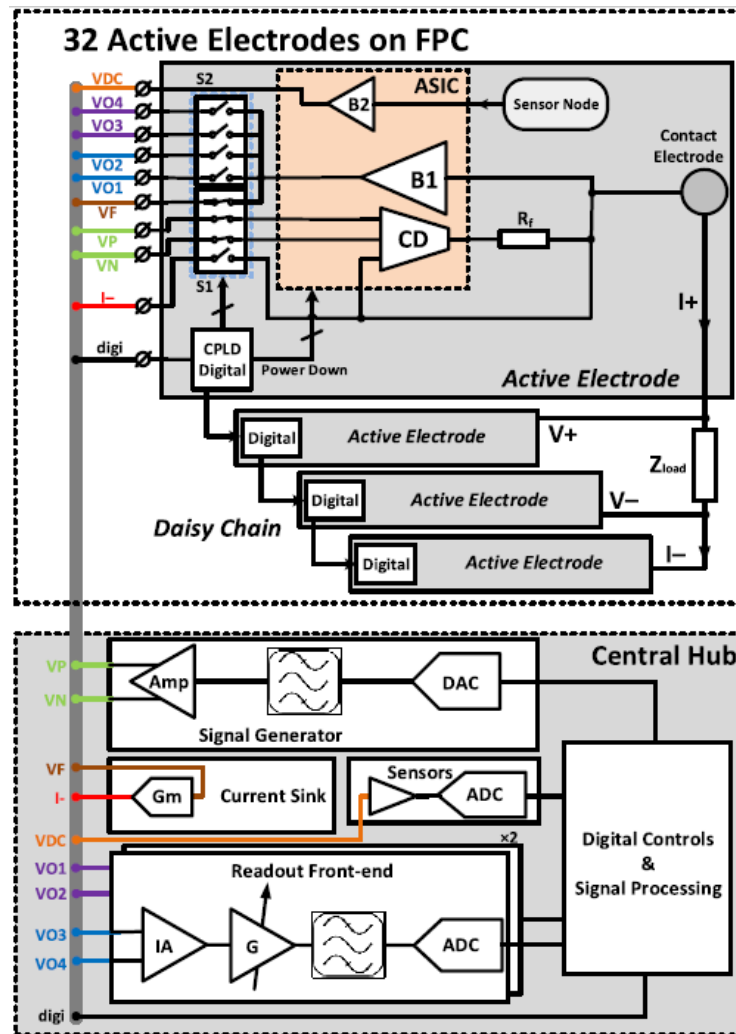


Figure 3.2: Active electrode belt system architecture. B1 is the main buffer, B2 is the sensor buffer and CD is the current driver in the ASIC. All electrodes share coloured analog paths, and are controlled by the digital CPLD.

3.2.2 Digital controls and signal processing¹

3.2.2.1 Active electrode control

One of the design challenges in the active electrode arrangement is how to address the electrodes for current drive and voltage scan. For a 32 electrode system, 1024 voltages needs to be recorded from different electrode positions. Using two parallel analog readout front-ends for voltage scan (see Figure 3.2) and for a frame rate higher than 100 fps, data acquisition on each pair of electrodes must be completed within 19.5 μ s before the IAs are switched to the next pair of electrodes. Therefore, the digital control of electrode switching must be as fast as possible to allow sufficient time for the amplifiers to settle and for acquiring sufficient samples for signal processing. Direct control of each electrode for current drive or voltage scan would provide the maximum flexibility and fastest control, but would require two dedicated tracks on the belt per electrode, which significantly increases design complexity and post risk of device failure. Another option is to assign each electrode an address and broadcast the addresses of the selected electrodes via a shared bus on the belt. Although this solution could reduce the number of tracks on the belt, it requires a high data rate ($> \text{Mbits/s}$) for address broadcasting.

A third option is to activate the electrodes in a pre-stored sequence. This avoids the shortcoming of the previous two solutions but limits the flexibility in electrode selection. This is accomplished by using a shifting daisy chain control arrangement which allows the electrode selection to be conducted from shared clock and data buses. There are two 2-line control buses on the belt to activate the electrodes for current drive and voltage scan. Each bus consists of a clock line and a data line. The clock line is shared by all the active electrodes, and the data line is arranged in a daisy chain fashion.

¹ The digital circuit design in this section is collaborative work with Dr. Dai Jiang, UCL

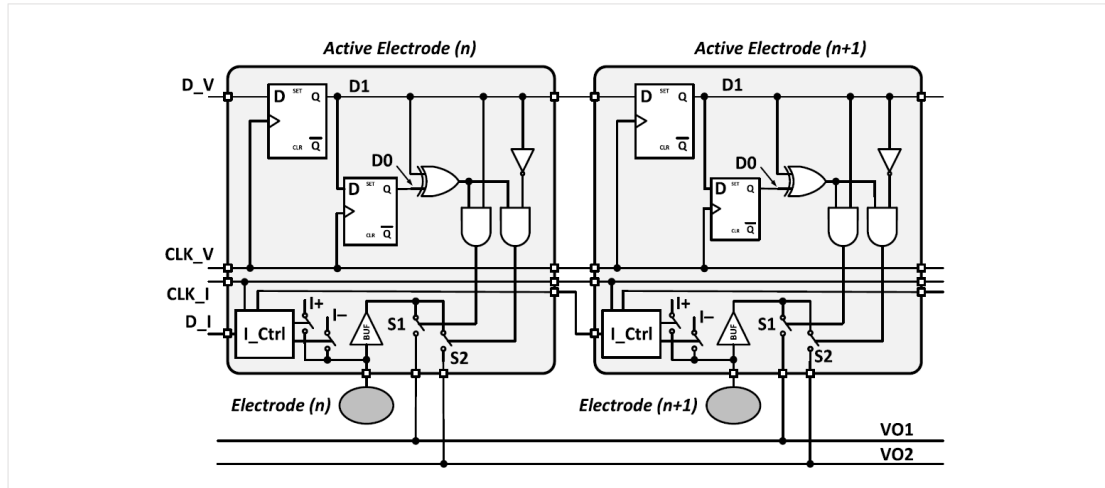


Figure 3.3: Control logic for electrode selection.

Figure 3.3 illustrates the control arrangement for voltage scan. The data line D_V is cascaded in a daisy chain, which is clocked by CLK_V on the clock line. There are two latches in each electrode, where $D1$ is connected to the next electrode as part of the D_V daisy chain, and its output also feeds into the second latch, $D0$. During operation, a 32-bit stream shifts through the electrodes along D_V at one bit per rising edge of CLK_V . The bit stream has two identical 16-bit segments with either segment consisting of m consecutive logic “1” bits and $(16 - m)$ logic “0” bits. At every rising edge on CLK_V , each electrode latches the incoming bit to $D1$ and compares it with the previous bit on D_V , now latched on $D0$, to decide whether and how to activate this electrode for voltage scan. For example, as shown in Figure 3.3, if $D1$ is “1” and $D0$ is “0” on *Active Electrode (n)* on the left, $S1$ will turn on to connect the buffered electrode voltage to $VO1$, which is connected to the positive voltage input of the IA in the readout analog front-end in the central hub (see Figure 3.2). Concurrently, $D1$ will be “0” and $D0$ “1” on *Active Electrode (n+m)*, which will turn on $S2$ to buffer the electrode voltage to the negative input of the IA through $VO2$ (similarly for $VO3$ and $VO4$ from *Active Electrode (n+16)* and $(n+16+m)$, respectively). A full voltage scan cycle is completed by shifting the bit stream through the daisy chain, where the scan pattern can be programmed by changing the value of m .

The electrode activation for current drive is similar and is operated from the other 2-line bus on the belt consisting of D_I and CLK_I. The selected electrode connects to either I+ or I-. The scan pattern for current drive can also be programmed in the same fashion. For every bit shifting on D_I, a full voltage scan cycle is conducted. Once the bit stream on D_I has shifted through all the 32 active electrodes, the image acquisition of one frame is completed. CLK_I, CLK_V, D_I and D_V are all generated by the control and signal processing module in the central hub.

3.2.2.2 Control and signal processing in the central hub

The control and signal processing module in the central hub can operate with a master clock frequency up to 50 MHz limited by the maximum operating frequency of the data converter. Besides controlling the electrode selection among the active electrodes, this module also manages a DDS-based signal generator, the operation of data acquisition from the analog readout front-end, and the digital I-Q demodulation.

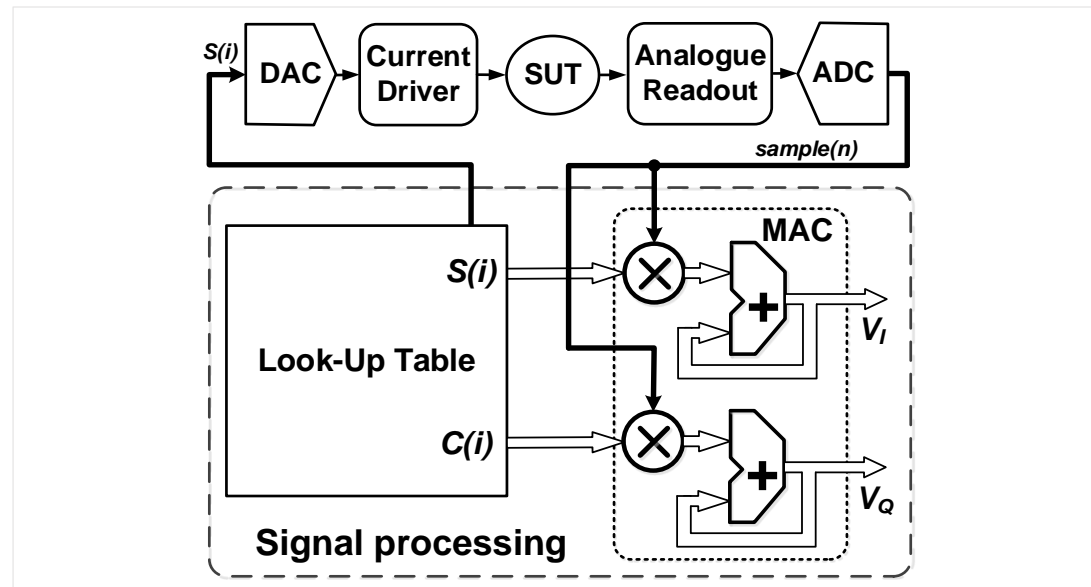


Figure 3.4: Control flow of calculating vectors V_I and V_Q .

Figure 3.4 shows the control flow of impedance measurement during the voltage scan on a chosen pair of electrodes. The operation of data demodulation synchronizes to the signal generator. In operation, two 16-bit sequences, $S(i)$ and $C(i)$, are read out

from a look-up table at a sampling rate of 3 MHz, where $S(i) = \sin 2\pi(n/N)$ and $C(i) = \cos 2\pi(n/N)$, and $N = 16$. $S(i)$ goes to the DAC to generate a sinusoidal signal for the current drivers. Concurrently, both $S(i)$ and $C(i)$ values are fed to a pair of multiplier accumulators (MACs) to multiply the ADC samples of the voltage readout, $sample(n)$. The real and imaginary vectors, V_I and V_Q , can be respectively derived using:

$$V_I = \sum_{n=0}^{N-1} sample(n) \times \sin 2\pi(n/N) \quad (3.1)$$

$$V_Q = \sum_{n=0}^{N-1} sample(n) \times \cos 2\pi(n/N). \quad (3.2)$$

The gains of the amplifiers in the analog readout front-end (Figure 3.2) are set with respect to the relative position between the electrode pairs for voltage scan and current drive, in order to utilize the full dynamic range of the ADC input.

3.3 Active electrode ASIC

3.3.1 Current stimulation

The current driver topology is shown in Figure 3.5 (a). It comprises a differential difference transconductance amplifier (DDTA) and an operational transconductance amplifier (OTA) configured in a linear current feedback to regulate the output current to the load R_L .

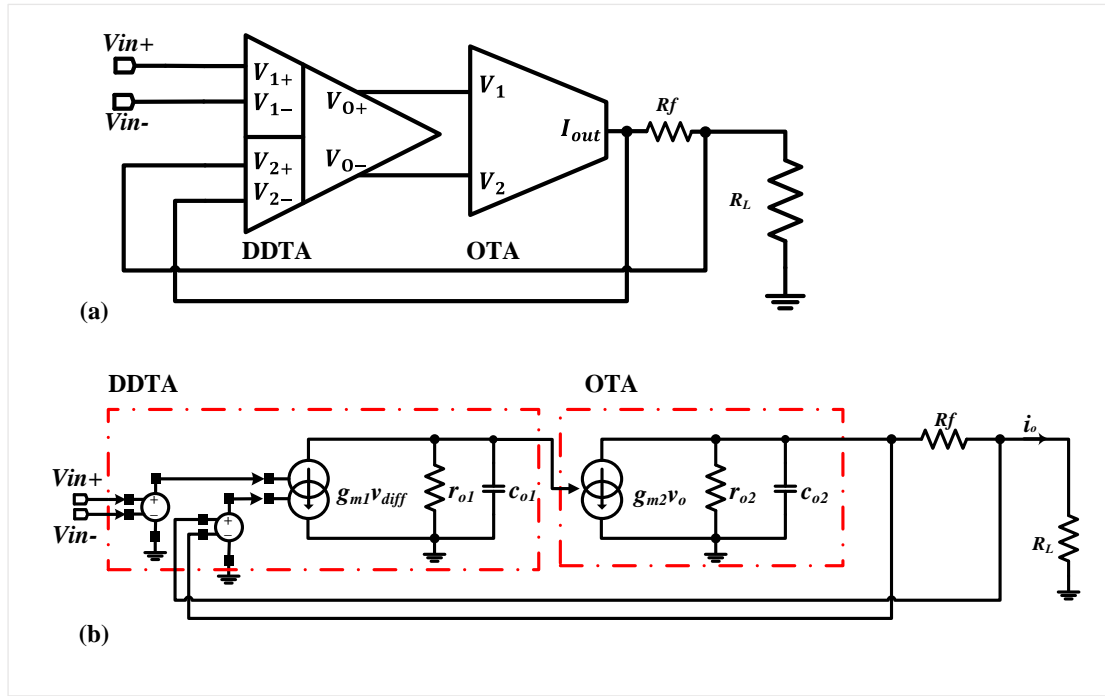


Figure 3.5: (a) the proposed current driver topology, (b) the small-signal analysis circuit for the current driver.

The small-signal circuit of the current driver is shown in Figure 3.5 (b). By analysing the small-signal circuit, at low frequency (ignoring the effect of C_{oi}) the transconductance of the current driver can be written as:

$$Gm_{CD} = \frac{i_o}{V_{in+} - V_{in-}} = \frac{g_{m1} \cdot r_{o1} \cdot g_{m2}}{1 + g_{m1} \cdot r_{o1} \cdot g_{m2} \cdot R_f + \frac{R_f + R_L}{r_{o2}}} \quad (3.3)$$

where $g_{m1} \cdot r_{o1}$ is the open loop gain of DDTA, g_{m2} is the transconductance of the OTA stage, and r_{o2} is the output impedance of OTA at node I_{out} .

The output impedance of the current driver can be derived by grounding the input and applying a current to the circuit's output while R_L is disconnected. The output impedance at low frequency can be written as:

$$Z_o = r_{o2} + R_f \cdot (gm_1 \cdot r_{o1} \cdot gm_2 \cdot r_{o2} + 1) \quad (3.4)$$

When considering the frequency response due to capacitor C_{o1} from the DDTA stage, and C_{o2} from OTA stage, the r_{o1} and r_{o2} are modified to $\frac{r_{o1}}{1+j\omega/2\pi f_{p1}}$ and $\frac{r_{o2}}{1+j\omega/2\pi f_{p2}}$,

where $f_{p1} = \frac{1}{2\pi \cdot r_{o1} \cdot c_{o1}}$, and $f_{p2} = \frac{1}{2\pi \cdot r_{o2} \cdot c_{o2}}$, equation (3.3) can be re-written as:

$$Gm_{CD}(\omega) = \frac{\frac{AG}{1+j\omega/2\pi f_{p1}}}{1 + \frac{AG}{1+j\omega/2\pi f_{p1}} \cdot R_f + \frac{R_f + R_L}{\frac{r_{o2}}{1+j\omega/2\pi f_{p2}}}} \quad (3.5)$$

where $AG = gm_1 \cdot r_{o1} \cdot gm_2$, and This equation can be further simplified dividing by $R_f \cdot \frac{AG}{1+j\omega/2\pi f_{p1}}$ on the denominator and numerator:

$$Gm_{CD}(\omega) = \frac{1/R_f}{1 + \frac{1+j\omega/2\pi f_{p1}}{AG \cdot R_f}} = \frac{1/R_f}{1 + \frac{j\omega}{2\pi f_{p1} \cdot AG \cdot R_f}} \quad (3.6)$$

assuming $AG \cdot r_{o2} \gg 1 + \frac{R_L}{R_f}$, and $\omega < 2\pi f_{p1}$, $\omega < 2\pi f_{p2}$. From equation (3.6), it can be seen that $f_{p1} \cdot AG \cdot R_f$ is the closed-loop dominant pole for the current driver under negative feedback.

Using equation (3.6), a 3-D mesh can be plotted to optimise design parameter AG and f_{p1} at e.g. 1 MHz operating frequency. The design also optimizes for wideband, high output impedance while maximizing output current amplitude towards higher signal to noise ratio.

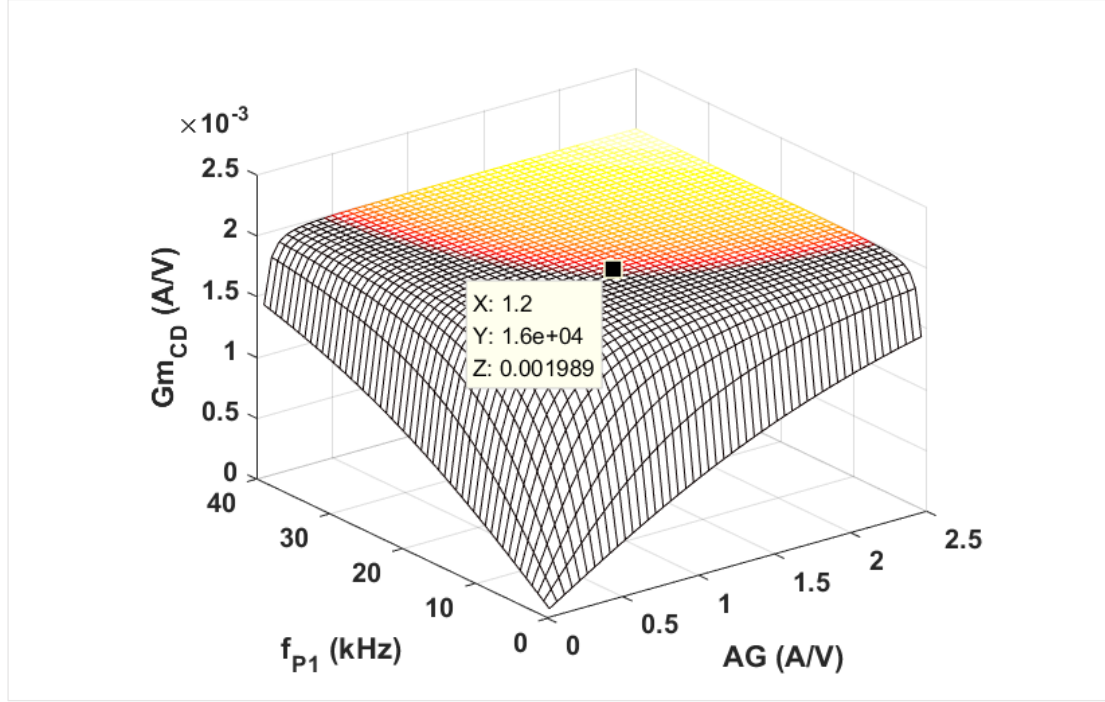


Figure 3.6: 3D mesh for the current driver transconductance parameter setting at 1MHz operating frequency.

When $R_f = 500 \Omega$, the ideal transconductance is 2 mA/V, and as shown in Figure 3.6, the coloured area indicates the optimal region where the overall current driver transconductance is higher than 1.985 mA/V. By targeting $AG > 1.2 \text{ A/V}$, and $gm_2 = 2 \text{ mA/V}$, the resultant open-loop gain of DDTA is $A_{ol_ddta} = \frac{AG}{gm_2}$ is around 56 dB with its dominant pole f_{p1} set around 16 kHz.

The same approach can be applied to equation (3.4), and it can be re-written as:

$$Z_o(\omega) = \frac{r_{o2}}{1 + j\omega/2\pi f_{p2}} + R_f \cdot \left(\frac{AG}{1 + j\omega/2\pi f_{p1}} \cdot \frac{r_{o2}}{1 + j\omega/2\pi f_{p2}} + 1 \right) \quad (3.7)$$

Using equation (3.7), and with $AG = 1.2 \text{ A/V}$, and $f_{p1} = 16 \text{ kHz}$ the following figure can be plotted at 1 MHz operating frequency.

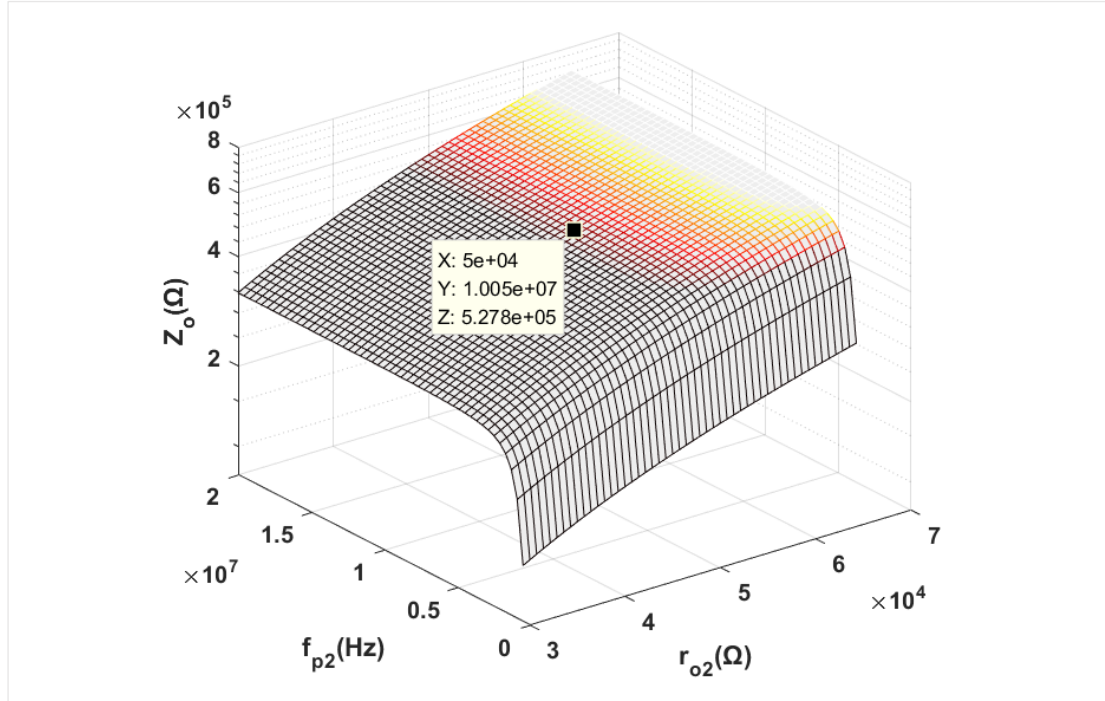


Figure 3.7: 3D mesh for the current driver output impedance parameter setting at 1MHz operating frequency.

To achieve an output impedance $|Z_o| > 500 \text{ k}\Omega$, the required specifications are set to $r_{o2} > 50 \text{ k}\Omega$, and $f_{p2} > 10 \text{ MHz}$. As a result, the OTA, which has its gm_2 set to 2 mA/V , should be designed with an open-loop gain ($A_{ol_ota} = gm_2 \cdot r_{o2}$) around 40 dB with its dominant pole set around 10 MHz . The output impedance seen by the load is defined by Z_o in parallel with any parasitic capacitances seen at the output. An active electrode provides an intimate connection between the current driver output and the electrode to avoid the large parasitic capacitance and thus allows the high output impedance to be maintained at high frequency.

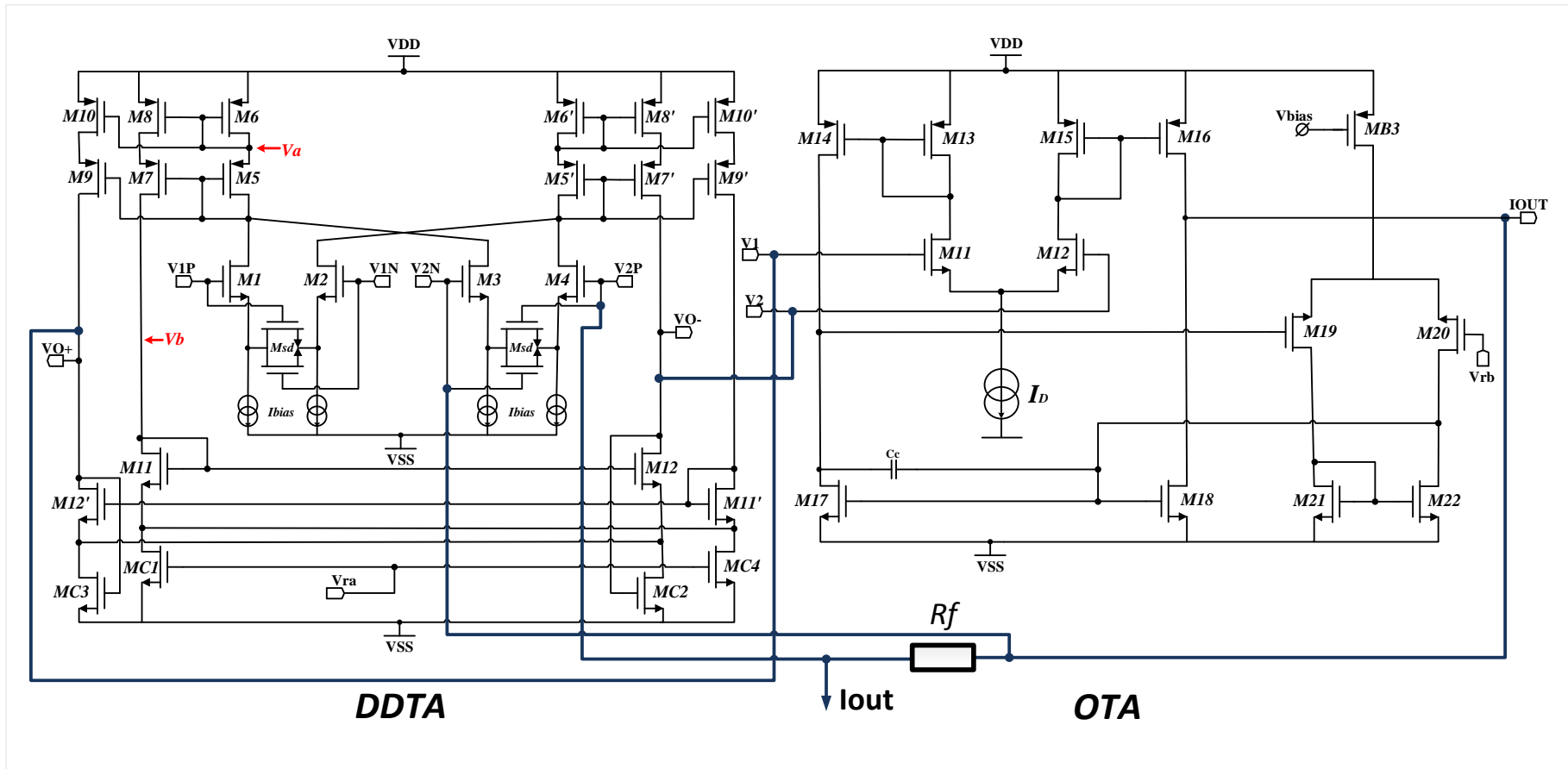


Figure 3.8: Detailed transistor-level schematic of the current driver (CD).

The circuit implementation at CMOS level is given in Figure 3.8, including both the DDTA and OTA stage in the linear current feedback configuration. The DDTA sums the current in M1 and M3 through M6 and mirrors this current through M8 to M11. Then this current is mirrored and is sunk from VO- by M20. While at the same time, the current in M2 and M4 is summed and mirrored to M14 and sourced to VO-. As a result, the circuit compares two differential input signals and the transfer function can be written as:

$$V_{O-} \approx A_{ol_DDTA} \cdot [(V_{1+} - V_{1-}) - (V_{2+} - V_{2-})] \quad (3.8)$$

where the A_{ol_DDTA} is the open loop gain of DDTA stage. The circuit employs a pseudo-differential topology [84] to offer a fully differential output stage.

To achieve a high output current amplitude with low distortion, four source-degeneration transistors M_D are added to the cross-coupled input pairs of the DDTA. The linear-range is approximately $\pm\sqrt{2} \cdot V_{ov}$ and $V_{ov} = \frac{2 \cdot I_D}{gm_{in}}$. With the added M_{SD} , the input transconductance:

$$gm_{in} = \frac{gm_1}{1 + gm_1 \cdot r_s} \quad (3.9)$$

where $gm_1 = \sqrt{2 \cdot \mu_n \cdot C_{ox} \cdot (\frac{W}{L})_1 \cdot I_d}$ and r_s is equal to:

$$r_s = \frac{1}{\mu_n C_{ox} (W/L)_D \cdot (V_{gs} - V_{th})} \quad (3.10)$$

For $gm_1 \cdot r_s > 1$, the linear range of the differential input pair is then extended by sizing the M_{SD} transistor dimension. Targeting a max current amplitude 6 mA_{pp} with a feedback resistor of 500Ω , the input linear range must accommodate maximum voltage of $3 V_{pp}$, and the size of the source degeneration transistors are swept using parametric analysis in Cadence to achieve the desired linear range.

Cascode current mirrors are used to enhance the output resistance and achieve the desired open-loop gain. Since the circuit is fully symmetrical, and $gm_6 \gg g_{01} + g_{03}$, the following equation can be written for the voltage node V_a :

$$V_a \approx -\frac{gm_{in}}{gm_6} \cdot (V_{1+} + V_{2-}) \quad (3.11)$$

and for voltage node V_b :

$$V_b \approx -\frac{gm_{in}}{gm_6} \cdot \frac{gm_8}{gm_{11}} \cdot (V_{1+} + V_{2-}) \quad (3.12)$$

then the output voltage V_{O-} is:

$$V_{O-} \approx \frac{gm_{in}}{g_{out}} \cdot \left[\frac{gm_{12} \cdot gm_8}{gm_6 \cdot gm_{11}} (V_{1+} + V_{2-}) - \frac{gm_{6'}}{gm_{8'}} \cdot (V_{1-} + V_{2+}) \right] \quad (3.13)$$

and:

$$V_{O-} \approx \frac{\beta \cdot gm_{in}}{g_{out}} [(V_{1+} - V_{1-}) - (V_{2+} - V_{2-})] \quad (3.14)$$

where $\frac{gm_{6'}}{gm_{8'}} = \frac{gm_6}{gm_8} = \beta$, $gm_{11} = gm_{12}$, and $\frac{1}{g_{out}}$ is the output impedance at node V_{O-}

which is $gm_7 \cdot r_{o7} \cdot r_{o8}$ in parallel with r_{o12} . As this node is also the only high impedance node in the circuit, the dominant pole of the system is at:

$$f_{p1} = \frac{1}{2 \cdot \pi \cdot \frac{1}{g_{out}} \cdot C_{out}} \quad (3.15)$$

where C_{out} is the capacitance seen at V_{O-} .

Four triode-transistors M_C are used for common-mode feedback, since M_{11} , M_{12} are a matched pair,

$$I_d = \frac{1}{2} \cdot \beta_{11} \cdot (V_{gs_{11}} - V_{th_{11}})^2 \quad (3.16)$$

and

$$I_d = \frac{1}{2} \cdot \beta_{12} \cdot (V_{gs_{12}} - V_{th_{12}})^2 \quad (3.17)$$

where $\beta_{11/12} = \mu_n \cdot C_{ox} \cdot \left(\frac{W}{L}\right)_{11/12}$, and because $V_{g_{11}} = V_{g_{12}}$, and $V_{th_{11}} = V_{th_{12}}$,

then $V_{s_{11}} = V_{s_{12}}$. For the MC transistors,

$$I_d = \beta_{c1} \cdot (V_{ra} - V_{ss} - V_{th_c}) \cdot (V_{s_{11}} - V_{ss}) \quad (3.18)$$

and

$$I_d = \beta_{c2} \cdot (V_{o-} - V_{ss} - V_{th_c}) \cdot (V_{s_{12}} - V_{ss}) \quad (3.19)$$

where $\beta_{ci} = \mu_n \cdot C_{ox} \cdot \left(\frac{W}{L}\right)_{ci}$. From equation (3.18) and (3.19), it can be seen that the

DC level at the circuit output can be set by biasing V_{ra} .

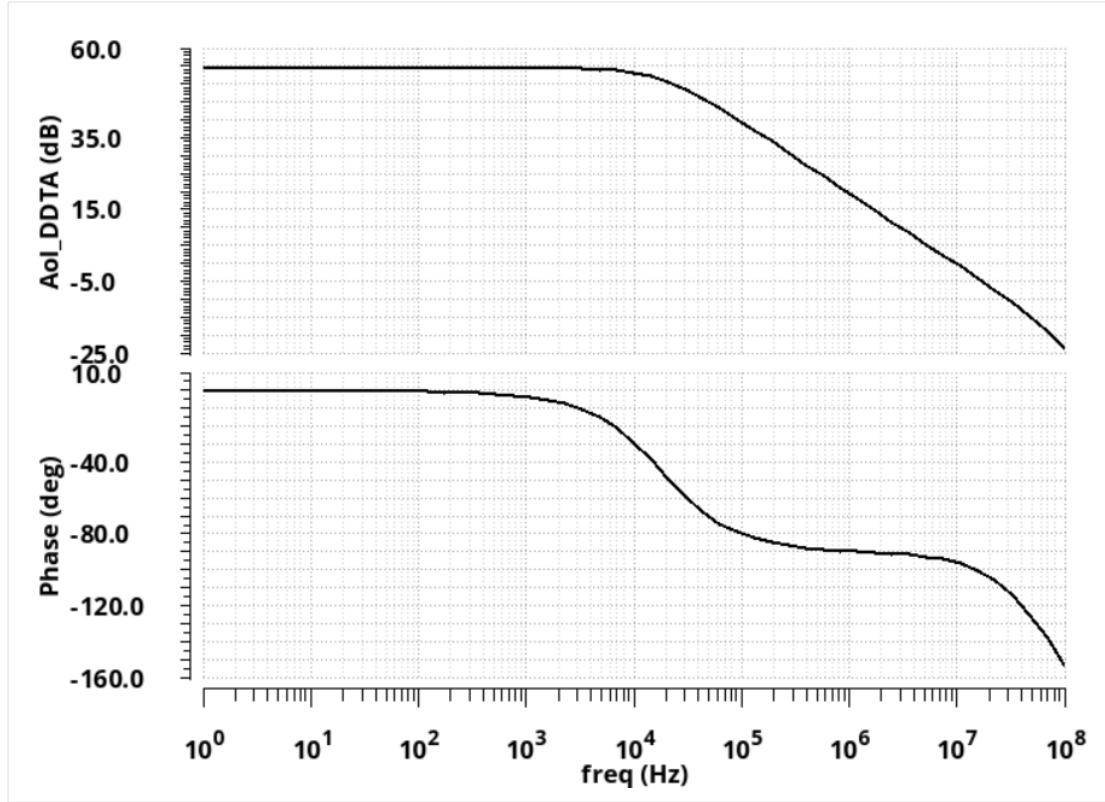


Figure 3.9: The open-loop gain and phase response of the DDTA.

The DDTA has been designed and the simulated open loop gain and the phase response is shown in Figure 3.9 with $A_{ol_{vo_}} = 54.5 \text{ dB}$, and $f_{p1} = 18.6 \text{ kHz}$

The transistor level circuit for the OTA is shown on the right-hand side of Figure 3.8. It enhances the current output ability of the current driver. It is based on a symmetrical topology and has a dc biasing stage M19 to M22 configured into a feedback loop with M14 and M17 to provide a biasing voltage for transistor M17 and M18 and set the dc level at IOOUT. The compensation capacitor C_c improves the phase margin of this dc biasing feedback loop. Its transconductance previously defined as g_{m2} can also be written as:

$$g_{m2} = \beta \cdot \sqrt{2\mu_n C_{ox} \cdot \left(\frac{W}{L}\right)_{11} \cdot I_D} \quad (3.20)$$

where the β is the aspect ratio of M15 and M16.

g_{m2} is designed to be 2.34 mA/V, r_{o2} is defined as $\frac{1}{g_{ds16}+g_{ds18}}$ and is extracted to be 55.3 k Ω . f_{p2} is defined as $\frac{1}{2\pi r_{o2} C_{o2}}$ which is designed to be 9.6 MHz. The output compliance of the circuit can be defined in the following equation:

$$V_{SS} + V_{ov_{18}} < V_{out} < V_{DD} - V_{ov_{16}}, V_{ov_i} = \sqrt{\frac{2 \cdot I_D}{\mu_i C_{ox} \cdot \left(\frac{W}{L}\right)_i}} \quad (3.21)$$

With the DDTA and OTA designed to the required specification using the parameters derived in the beginning of this section, the overall current driver was configured and simulated.

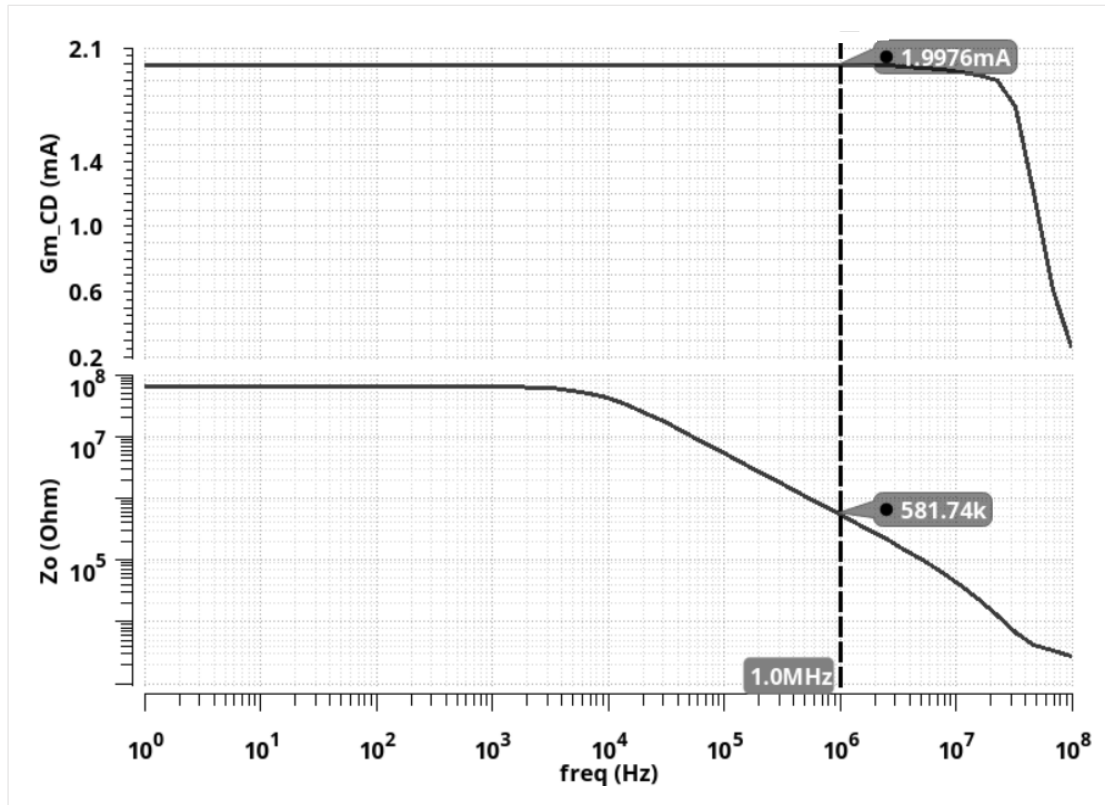


Figure 3.10: The simulated transconductance and output impedance of the current driver.

The simulated overall current driver transconductance and its output impedance over the frequency range is plotted in Figure 3.10, and these simulation results are found to be satisfactory.

The current driver implemented on the ASIC shown in Figure 3.8 provides a single-ended excitation drive I_+ . Differential injection can be implemented as shown in Figure 2.12 (b) using two independent ASIC driver. However, any transconductance mismatch between the current source and current sink would force the unmatched current to flow through the output impedance node of the current drivers [54]. To visualize the issue of common-mode error and aid the analysis, the equivalent circuit is given on Figure 3.11.

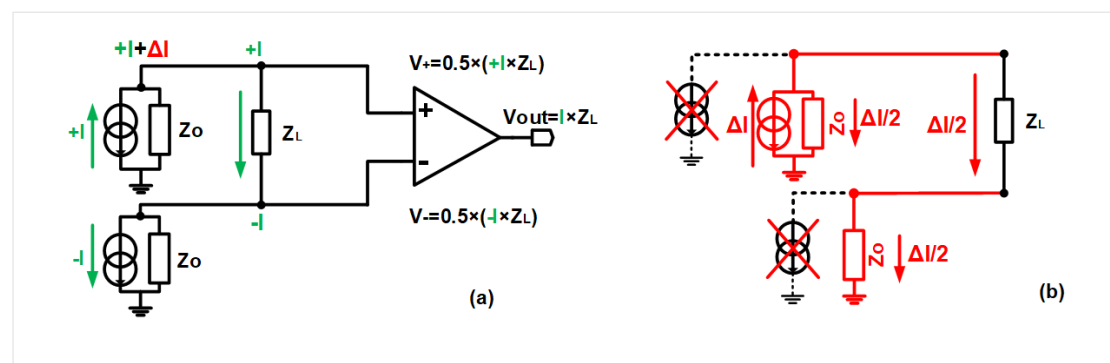


Figure 3.11: (a) Current driver without consider ΔI mismatched current flowing through the load Z_o ; (b) Current driver mismatch ΔI generating common-mode signals.

In the ideal case, as shown in Figure 3.11(a), current is sourced by $+I$ current driver will sink back to $-I$ current driver with zero CM. However, when mismatches occur as shown in Figure 3.11(b) in red, a mismatched current ΔI is generated and flows through the high-impedance node Z_o of the current driver. This results in two possible scenarios: 1) The output of the current driver is saturated, especially for large mismatch errors; 2) With small mismatch errors, low Z_o or benefiting from a high voltage compliance, the current driver may not be saturated, but a large common-mode signal of $\Delta I \times \frac{Z_o}{2}$ is generated and added to the small differential signals which then has to be accommodated by CMRR of the IA. Therefore, having two independent current drivers to perform the differential drive is not ideal and an alternative sink current circuit must be provided.

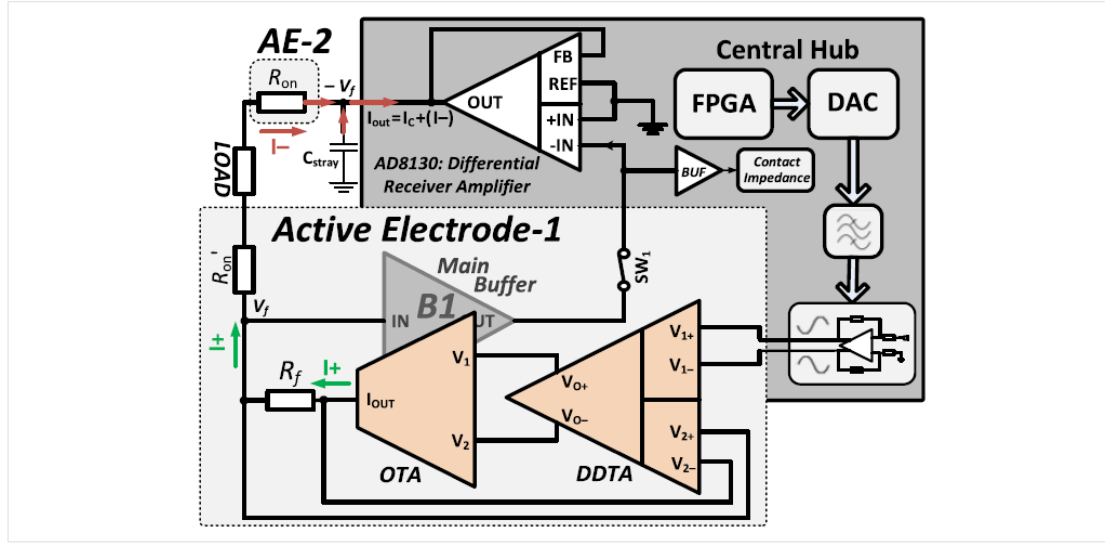


Figure 3.12: Complete current driver topology in the EIT system.

The implemented fully differential current driver is shown in Figure 3.12. When the selected *Active Electrode-1* is configured into master current excitation mode, a fully differential voltage signal is generated from the central hub as inputs to the current driver. This minimizes the input difference between the 32 current drivers on the wearable belt. The current driver on the ASIC sources a current of I_+ and the main buffer B1 senses the voltage V_f directly on the load and feeds it back to the central hub. The differential receiver amplifier (AD8130) receives V_f and generates a sink current I_- .

When the source current I_+ is equal to the sink current I_- , the voltage across the load is fully differential with zero common-mode voltage. This can be achieved by monitoring the CM voltage and actively offsetting the unmatched current [55], or generating a differential voltage with respect to V_f . This is achieved by connecting AD8130 as a resistive-less inverting unity gain amplifier as shown in Figure 3.12 and the closed-loop transfer function of this current sink amplifier can be written as:

$$A_{cl}(\omega) = A_{cl}(\omega) = -\frac{A_{ol}}{1 + A_{ol}} \cdot \frac{1}{1 + jf/A_{ol} \cdot f_o} \quad (3.22)$$

where A_{ol} is the open-loop gain, and $A_{ol} \cdot f_o$ is the gain bandwidth of AD8130, f is operating frequency.

AE-2 is a second active electrode that is configured in current drive slave-mode in Figure 3.12. In this mode, an analog switch is turned-on to connect the differential receiver amplifier to the load. As this switch has an on-resistance R_{on} , a dummy R_{on}' is placed in series with R_f for load matching.

Despite the fact that current sink circuit is located in the hub, its input signal V_f is actively buffered using B1, therefore the cable stray capacitance on the signal path is isolated from the output of the current driver on the active electrode. At the output of the differential receiver amplifier, to achieve $-V_f$, the receiver sinks not only a current I_- equal to I_+ , but also a current I_c to compensate for the cable stray capacitance in the current return path. As this current sink topology responds to the linear current feedback loop in the ASIC current driver, and compensates for the stray capacitance at its output, it also appears to have a high output impedance.

The voltage V_f fed back by B1 can also be used to monitor the contact impedance. For a good contact, the contact impedance is e.g. $500\ \Omega$, and a bad contact can be detected when the amplitude of $V_f > (I_+) \times 500\ \Omega$. By checking the voltage level on the buffer, the electrode contact can be continuously monitored while making EIT measurements in real-time.

3.3.2 Voltage acquisition and heart-rate recording

During EIT recording, a pair of active electrodes is selected to be in the voltage sense mode. The main buffer B1 sends the signal back to an IA in the central hub (see Figure 3.13) according to the user defined EIT scan pattern to measure the voltage difference between two electrodes. The current driver on the ASIC whose active electrodes are in voltage sense mode is powered-down as shown in Figure 3.13. The heart rate can be monitored using a selected pair of active electrodes in voltage sense mode to detect the ECG and send it via a separate analog path in the hub as shown in Figure 3.13. This provides an efficient way of measuring heart rate as well as EIT without the need for dedicated electrodes or an ECG device.

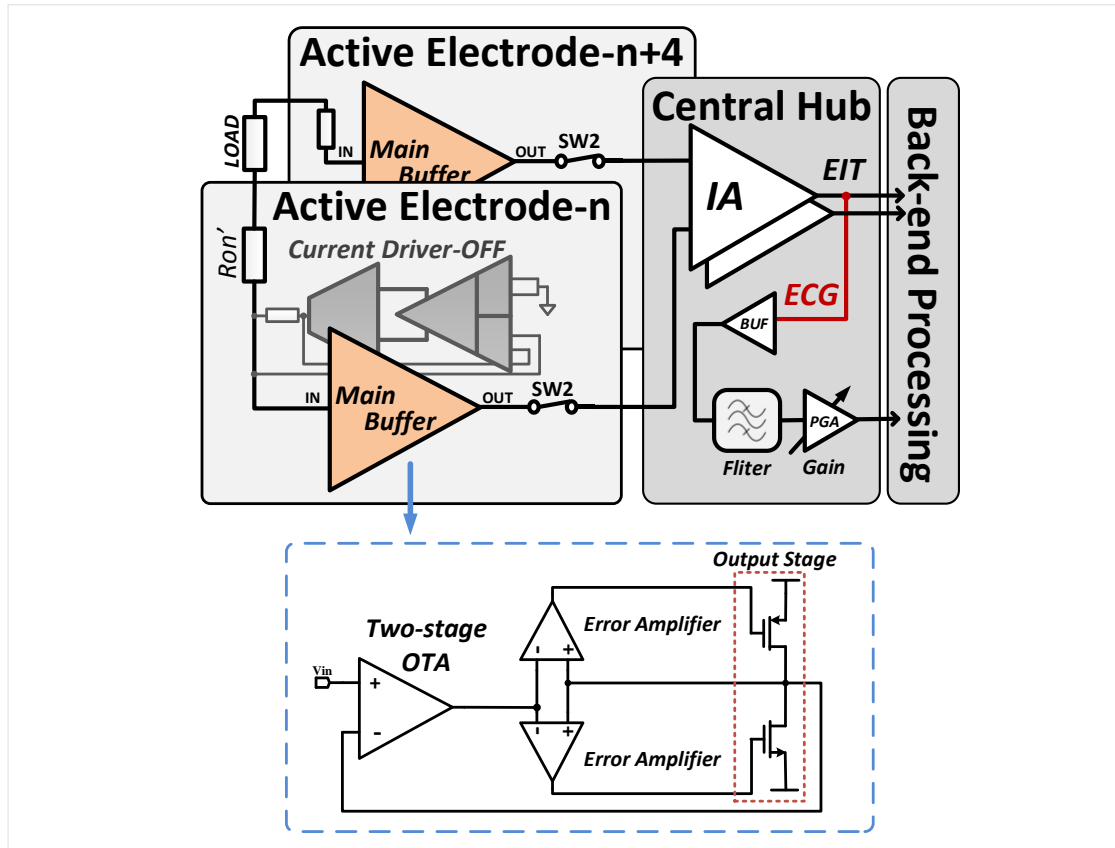


Figure 3.13: Proposed EIT voltage signal recording with active electrodes.

The working principle of main buffer B1 is also shown in Figure 3.13. It comprises a two-stage Miller OTA, and a common-source push-pull output stage (necessary to drive the large capacitive load on the FPC). The two error amplifiers regulate the quiescent current in the push-pull transistors and ensure the voltage at its output stage is equal to the voltage at the output of the OTA. The detailed CMOS level main buffer schematic is given in Figure 3.14

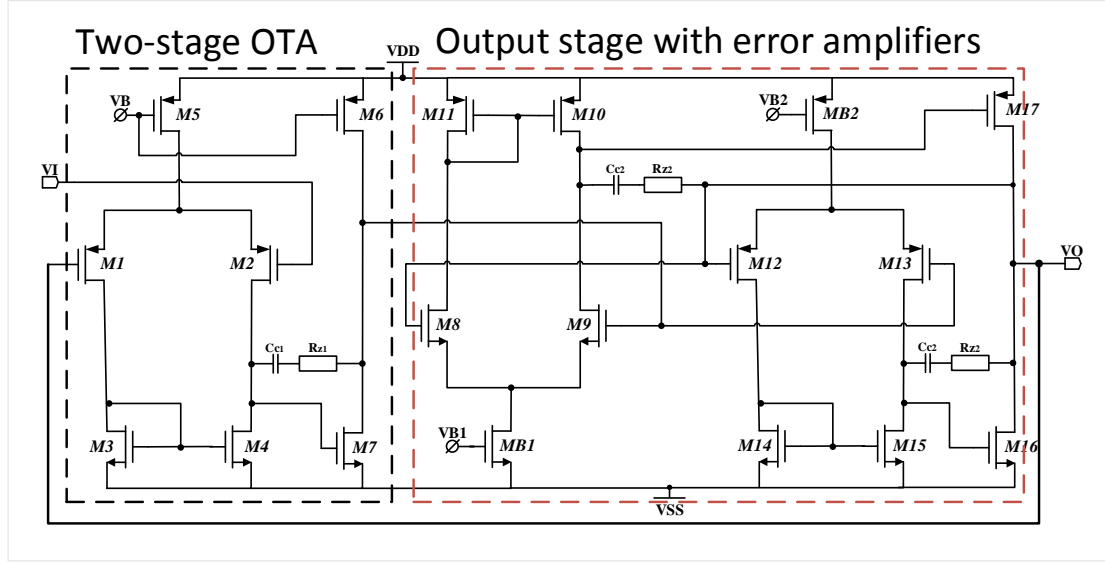


Figure 3.14: Main buffer B1: (a) working principle and (b) transistor-level circuit.

In a two-stage OTA design, all transistors need to be in the saturation region. For the front end two-stage OTA, $\frac{S_7}{S_4} = 2 \cdot \frac{S_6}{S_5}$, $S_i = \left(\frac{W}{L}\right)_{Mi}$ is required to achieve a proper mirror condition where $V_{M4_DG} = 0V$. This forces M4 into saturation and a balanced biasing current $I_{M6} = I_{M7}$. For the error amplifier, by setting V_{B1} and V_{B2} , the tail currents are set to be equal for both amplifiers. The frequency response of the front-end two-stage OTA has a loop gain of:

$$A_{ol_{front_end_OTA}} = A_{v1} \cdot A_{v2} = g_{m1} \cdot r_I \cdot g_{m7} \cdot r_{II} \quad (3.23)$$

where $r_I = \frac{1}{g_{ds2} + g_{ds4}}$, $r_{II} = \frac{1}{g_{ds6} + g_{ds7}}$. With Miller compensation, the dominant pole is

at $f_{dp} = \frac{1}{2 \cdot \pi \cdot g_{m7} \cdot r_I \cdot r_{II} \cdot C_c}$, and using pole-zero cancelling, the non-dominant pole is

removed. The same design procedure applies to the error amplifier two-stage OTA and

with feedback, this output stage has a low output impedance of $\frac{\frac{1}{g_{ds16}} + \frac{1}{g_{ds17}}}{1 + A_{ol_outputStage}}$.

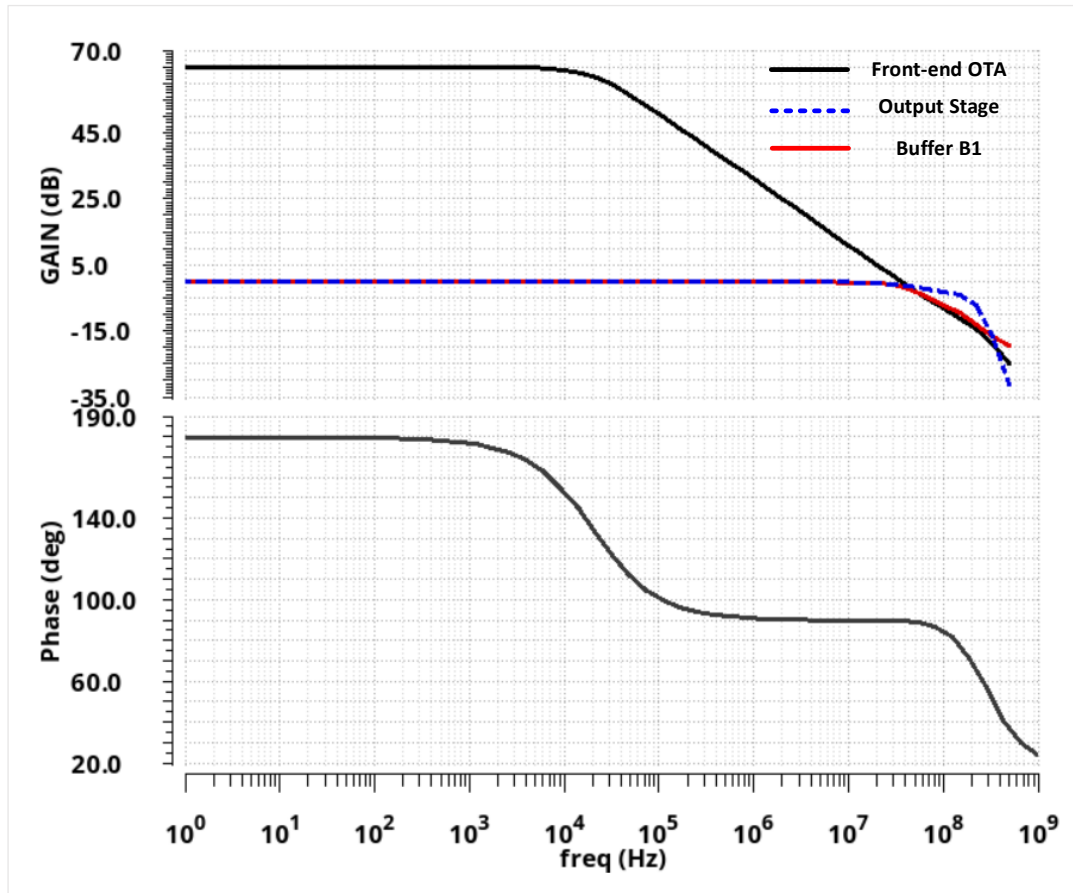


Figure 3.15: simulated ac response for the main buffer B1, front-end OTA in open-loop, and the error-amplifier output stage.

The simulated ac response for the main buffer and front-end OTA in open loop and the error amplifier output stage is shown in Figure 3.15 with $C_L = 2 \text{ pF}$. Aol of the front-end OTA is 65.3 dB and has the dominant pole designed at 21 kHz. With zero-pole cancelling, the new non-dominant pole is >400 MHz which is beyond the GBW of the front-end OTA. In closed loop, the output stage has its -3 dB point at 100 MHz, which is >3 GBW of the front-end OTA which is at 37.5 MHz and leads to a phase margin of 72°. When driving larger capacitive load, e.g. 20 pF, a small series resistor of 300 Ω is required, this reduces the BW to 30 MHz with a phase margin of 57°.

3.3.3 Multi-parameter sensor buffer

In addition to EIT and heart rate monitoring, the sensor buffer B2 on the ASIC allows measurement of dc signals from any connected sensor. This buffer uses a two-stage amplifier connected in unity feedback with a power-down. By controlling the power-down, the output of all sensor buffers can share a single bus line to the central hub for processing; this significantly simplifies the FPC design (see Figure 3.2). As proof of concept, four different types of sensor were integrated onto the belt with small FPCs to provide additional sensing parameters. An NTC based temperature sensor and a Honeywell HIH4000-001 humidity sensor were embedded to monitor the environmental temperature and humidity close to the belt to monitor belt condition for safe operation. Accelerometer sensors were included for belt orientation monitoring which provides additional information to aid the selection of EIT models for enhanced image reconstruction.

3.4 Measured results

3.4.1 Active electrode ASIC

The ASIC was designed in 0.35- μm CMOS HV process technology and operates from $\pm 9\text{ V}$ power supplies for high amplitude current injection and sufficient voltage compliance. The chip micrograph is shown in Figure 3.16 with the various blocks labelled. The total area is $3.1\text{ mm} \times 1.25\text{ mm}$.

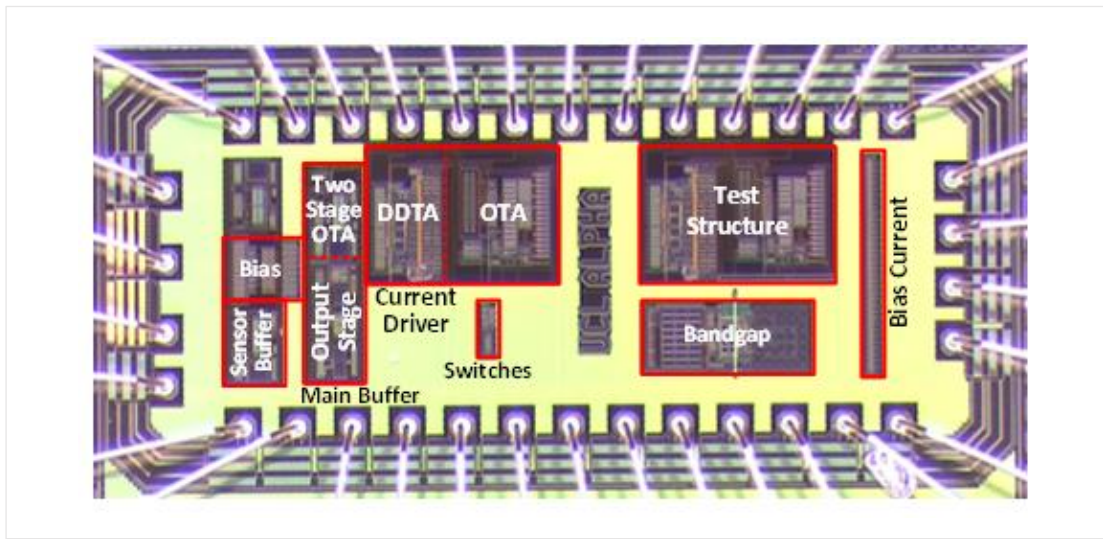


Figure 3.16: Active electrode ASIC micrograph.

A custom-designed PCB is used to measure the ASIC electrical performance. For buffer testing, the input V_{in} is generated by an external signal generator and sent to the buffer while the output is measured on the oscilloscope. The gain of the sensor buffer B2 is 0.99 V/V at dc and the gain of the main buffer B1 is 0.98 V/V up to 750 kHz . The phase delay is the phase difference between V_{in} and V_{out} . At 500 kHz it has a phase delay of 2° . Its output swing reaches 14 V_{p-p} at 500 kHz with an average total harmonic distortion (THD) of 59 dB which is a measurement of the harmonic distortion in dB relative to the fundamental as distortion attenuation. It has an input-referred noise voltage of $22\text{ }\mu\text{V}_{rms}$ measured from 20 kHz to 1 MHz with its input grounded while measuring the output on a spectrum analyzer using the post-amp method [85].

The transconductance of the current driver (Gm_{CD}) was measured at 500 kHz with a load of $50\ \Omega$ to eliminate the effect of parasitic capacitance. The output current was measured from $200\ \mu A_{p-p}$ to $6\ mA_{p-p}$ and the transconductance was calculated by $Gm_{CD} = V_{load}/(V_{in} \times 50\ \Omega)$ where V_{load} is the voltage across the load. As shown in Figure 3.17, the average transconductance is $1.99\ mA/V$ with a standard deviation of $10.3\ \mu A/V$. The current driver has a THD of 55 dB at the maximum output current of $6\ mA_{p-p}$ and a phase delay of 4° at 500 kHz (measured from the induced voltage on the load).

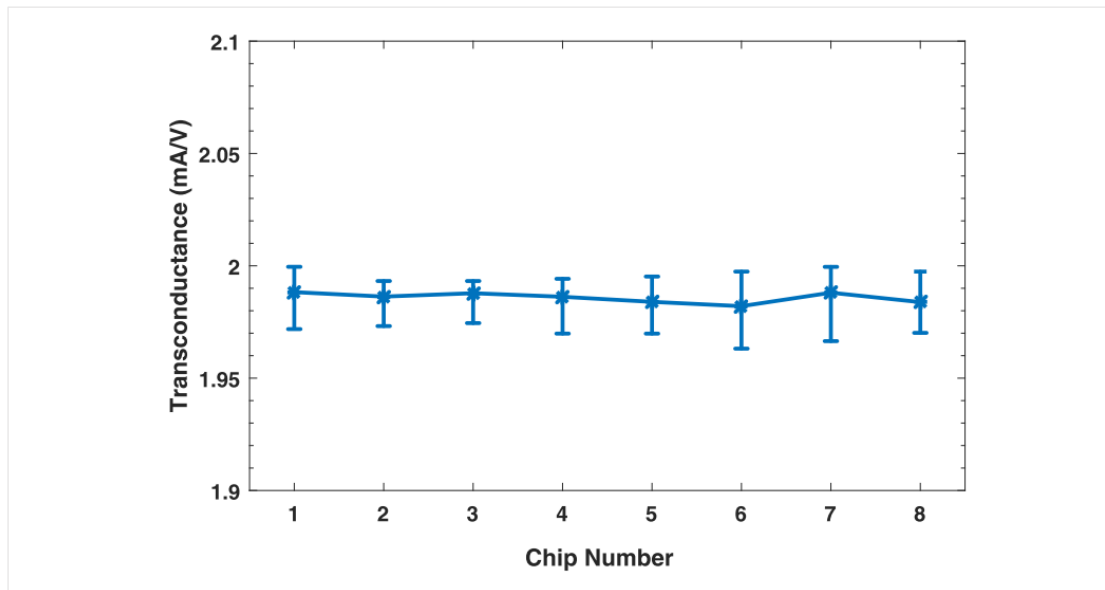


Figure 3.17: Measured transconductance of the current driver across eight chip samples. The average value is $1.99\ mA/V$ with a standard deviation of $10.3\ \mu A/V$.

When measuring the output impedance Z_{out} , any parasitic capacitance in parallel with Z_{out} should be excluded. The measurement set up used to obtain Z_{out} is shown in Figure 3.18. The current driver drives two different loads which can be toggled using a switch S_L . Initially, it drives $R_1 = 50\ \Omega$ to minimize the effect of the parasitic capacitance C_{stray} so the output current can be accurately set to $I = 1\ mA_{p-p}$ and the initial phase delay θ_{R1} due to the current driver can be measured between V_i and V_o . Then S_L opens and the current driver connects to $R_2 = 5.1\ k + 50\ \Omega$. As R_2 is significantly larger, the output current I splits into I_Z , I_C and I_O that flow into Z_{out} ,

C_{stray} and R_2 , respectively. As a result, a new phase delay θ_{R2} and voltage V_{R2} can be recorded and the output impedance of the current driver can be calculated using the following equations:

$$Z = \frac{V_{R2}}{1 \text{ mA}} \quad \text{and} \quad \theta_C = \theta_{R2} - \theta_{R1} \quad (3.24)$$

$$R_X = \sqrt{Z^2 + Z^2 \times \tan(\theta_C)^2} \quad (3.25)$$

$$Z_{\text{out}} = \frac{(R_X \cdot R_2)}{R_2 - R_X} \quad (3.26)$$

where Z combines R_2 , Z_{out} and C_{stray} in parallel, and θ_C is the phase delay due to C_{stray} only. Using (3.25) the capacitance C_{stray} can be excluded giving R_X (which is simply R_2 and Z_{out} in parallel) and using (3.26) finally Z_{out} is calculated.

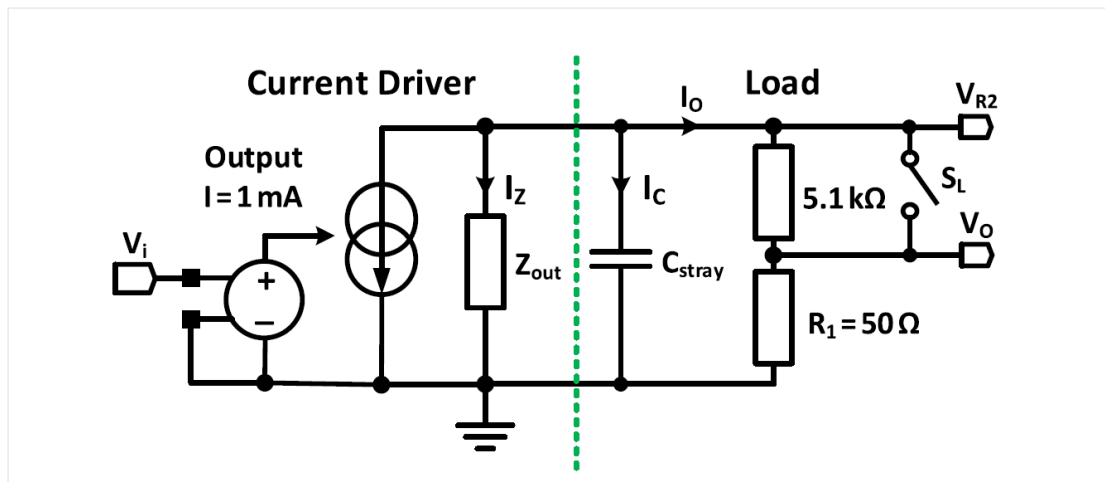


Figure 3.18: Current driver output impedance measurement circuit equivalent model.

Figure 3.19 shows Z_{out} measured from 250 kHz to 1 MHz; it is on average $>1 \text{ M}\Omega$ at the targeted 500 kHz bandwidth. The error bars in Figure 3.19 indicate the spread at a specific frequency. Table 3-1 summarizes the measured performance of the ASIC.

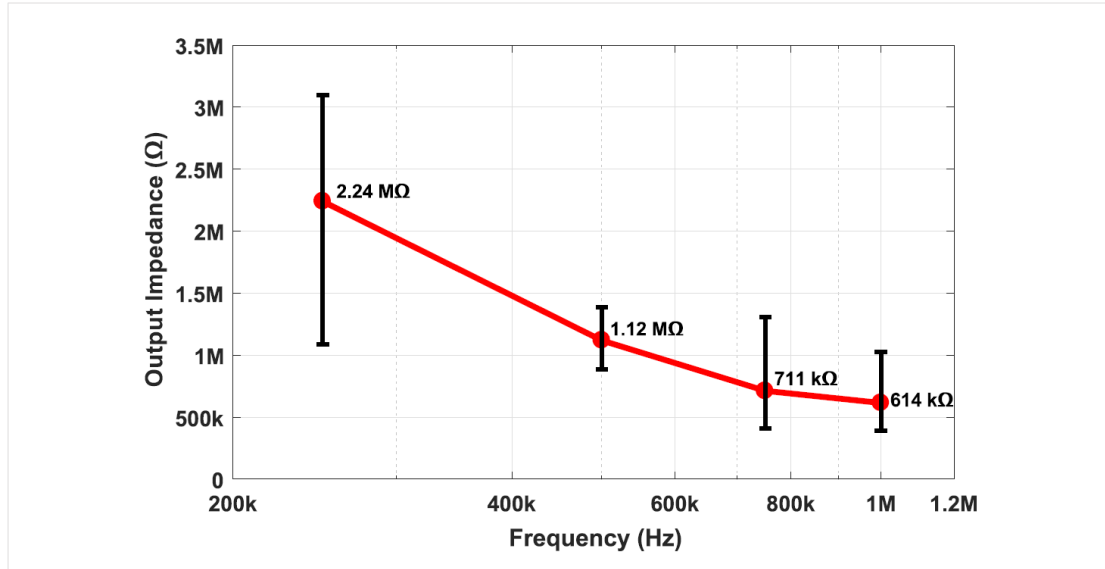


Figure 3.19: Measured mean output impedance of the current driver.

Table 3-1: ASIC Measured Performance.

	Transconductance (mA/V)	Bandwidth (Hz)	Phase (at 500 kHz)	Z_{out} (at 500 kHz)	Maximum I_{OUT}	THD	Voltage Compliance
Current Driver	1.99	500k	4°	1.12 MΩ	6 mA _{p-p}	55 dB	10 V _{p-p}
	Gain (V/V)	Bandwidth (Hz)	Phase (at 500 kHz)	Output Swing	THD	Input-Refereed Noise (0.02-1 MHz)	
Main Buffer B1	0.98	750 kHz	2°	14 V _{p-p}	59 dB	22 μVrms	
Sensor Buffer B2	0.99	dc buffer	-	16 V at dc	-	-	

3.4.2 EIT system evaluation

For system performance, 200 kHz is chosen as the nominal operating frequency. All 32 electrodes are numbered, and with all the odd and even-numbered electrodes are shorted and connected to a single resistor for calibration. For a 32-electrode system, according to the EIT adjacent scan pattern, it provides $32 \cdot (32 - 3) = 928$ channels of voltage readings (excluding the injecting pair). After calibration, each channel gives a calibration coefficient saved in a LUT table. The table is used to offset channel variations during EIT measurement.

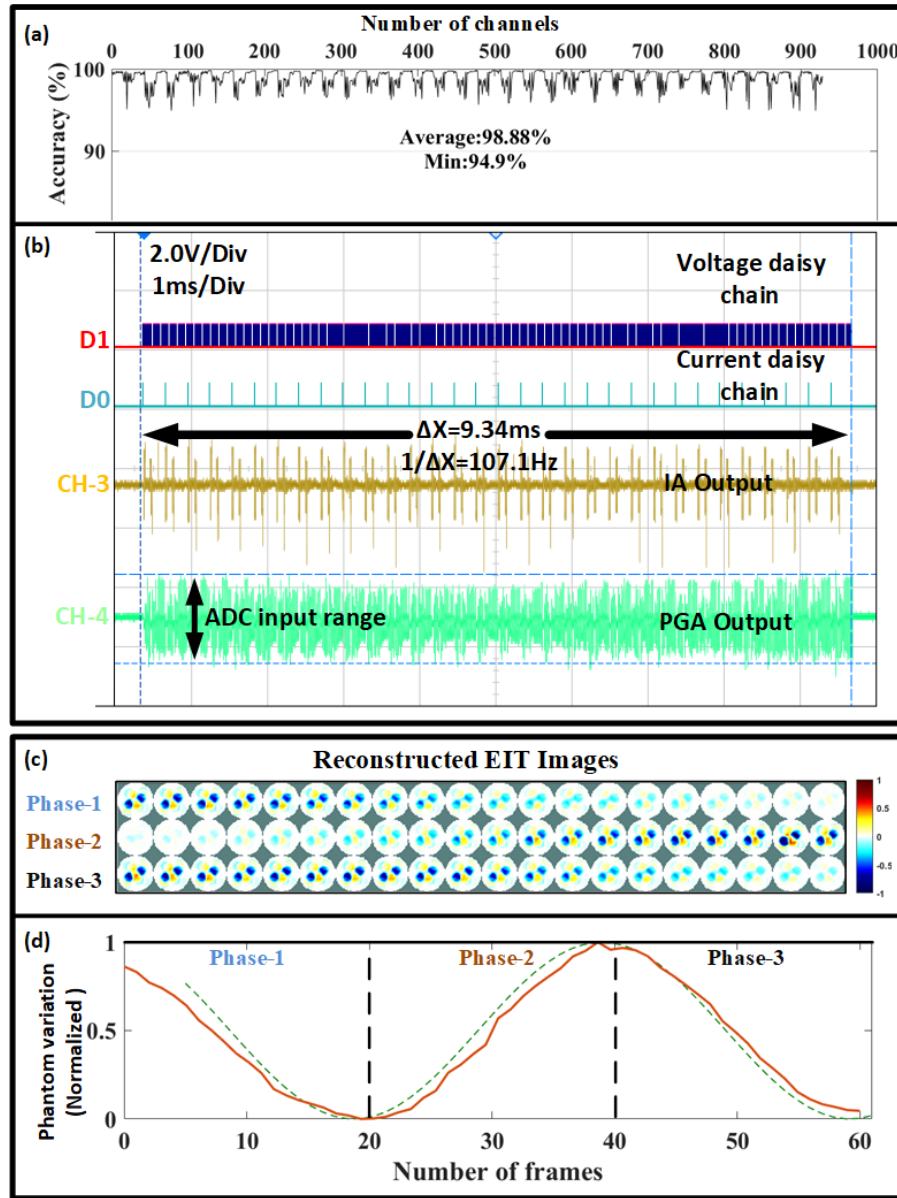


Figure 3.20: (a) System calibrated measurement results; (b) image frame rate capture on the oscilloscope; (c) resistive-mesh phantom test results in form of EIT images, the colour bar shows normalized conductance; (d) impedance variation plotted using data from resistive-mesh phantom test compared to the idea variation.

To evaluate system measurement accuracy, $R_{test} = 500 \Omega$ was used. The measurement accuracy is calculated by:

$$Acc\% = 100\% \cdot \left[1 - \frac{abs(R_{measured} - R_{test})}{R_{test}} \right] \quad (3.27)$$

Across all 928 EIT readings as shown in Figure 3.20(a), the system has an averaged measurement accuracy of 98.88%.

The system was then connected to a resistive-mesh phantom for EIT imaging. This phantom adapted from Figure 2.13 [50], has two diagonal inner resistive elements that are made variable from $36.5\ \Omega$ to $53.6\ \Omega$. Shown in Figure 3.20(b) is the oscilloscope signal waveform captured in one EIT frame. The D0 signal is the current drive daisy chain trigger signal CLK_I, and there are 32 signals indicating 32 current drive positions in one complete EIT frame. Between two current daisy chain signals, as shown by D1, 16 voltage-sense daisy chain triggers CLK_V are captured so that 16 differential voltages are measured per channel within one current drive position. Also in Figure 3.20(b), CH 3 shows the differential voltage signal at the output of the IA in the first data acquisition channel, and CH 4 shows the dynamic gain feature in the same data acquisition channels. The PGA equalizes all the voltage signals after the IA to a level close to the maximum ADC input range before digitization. One EIT frame to be completed in 9.32 ms or 107 fps.

In Figure 3.20(c) the EIT images reconstructed using EIDORS. The two dark blue circle areas indicate the location of the variable element. As the two elements change their resistive values, for example in phase-1, from maximum to minimum in a sinewave fashion, the corresponding 20 frames of EIT images tend towards all-white indicating their decrement in resistivity and vice-versa. The normalized regional impedance variation is plotted in solid-red in Figure 3.20(d) with reference to the ideal variation in dotted green.

To test the belt on a human subject, a suitable belt dressing with electrode contact is required. In the reported active EIT belts [79], [13] the electronics are permanently connected; autoclaving will damage the electronic components and the whole belt must be disposed of after use. The proposed belt is a combination of an FPC electronic core and a separate textile belt dressing. Only the low-cost textile dressing is disposed of after use. This significantly reduces the cost per patient from hundreds of dollars to a few dollars. Figure 3.21 shows the detailed belt layer-stacking diagram in 3D. Each FPC unit contains eight active electrode PCBs and an active belt consists of four units,

joined by FPC-to-FPC connectors. This provides a 32 electrode EIT system. The 8 mm×30 mm electrode-pads are on the bottom layer of the FPC to facilitate connection between the active electrode ASIC and the skin-contact electrode via the textile dressing. As only bus-lines are running on the FPC, this design allows easy adjustment of the overall length of the belt for future neonate applications.

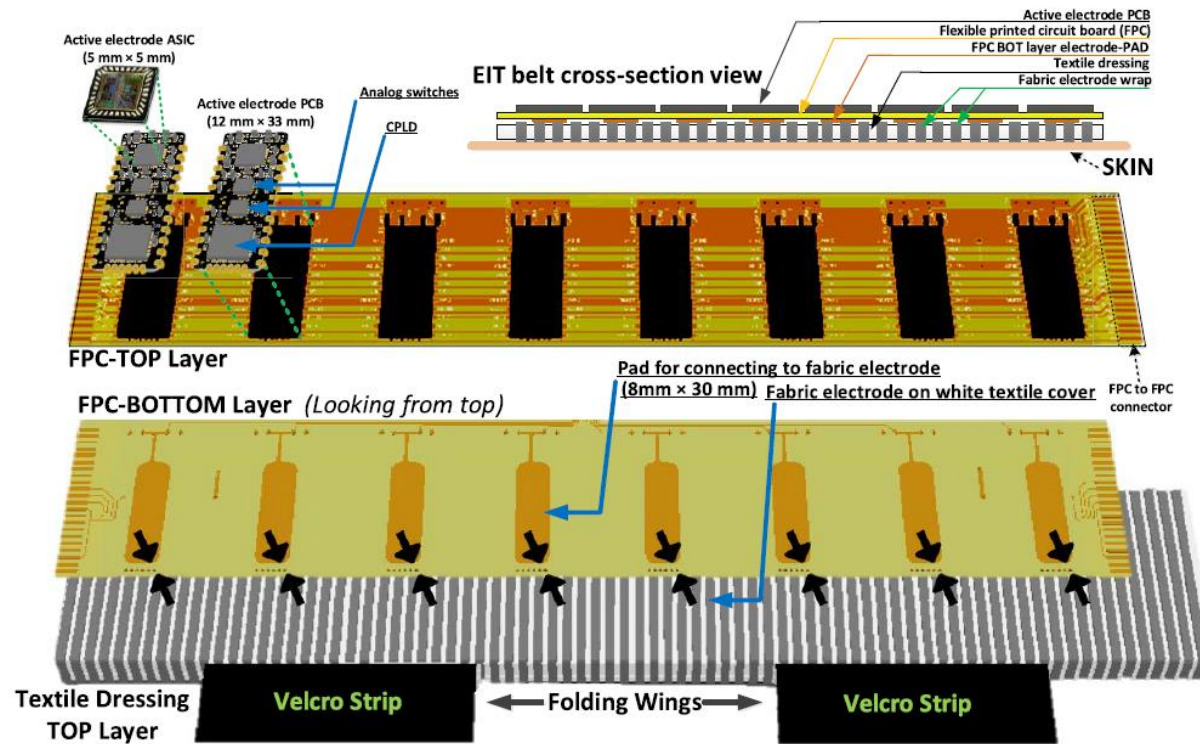


Figure 3.21: Detailed active EIT belt layer-stacking and cross-section view.

The disposable textile dressing consists of a white textile substrate with silver-coated fabric-electrode stripes evenly distributed across it. Each stripe wraps all the way around the substrate and when the FPC is placed on the top of the dressing, the electrode-pad on the bottom layer of the FPC contacts the fabric-electrode, which will then contact the skin.

This arrangement results in skin contact only a few millimetres away from the electronics with a fabric material resistance of less than $1\ \Omega$ from 50 kHz to 1 MHz. With the help of Velcro folding strips, the FPC electronic-core is held firmly inside the fabric dressing². The device is secured on the sternum by means of an elastic fastening.

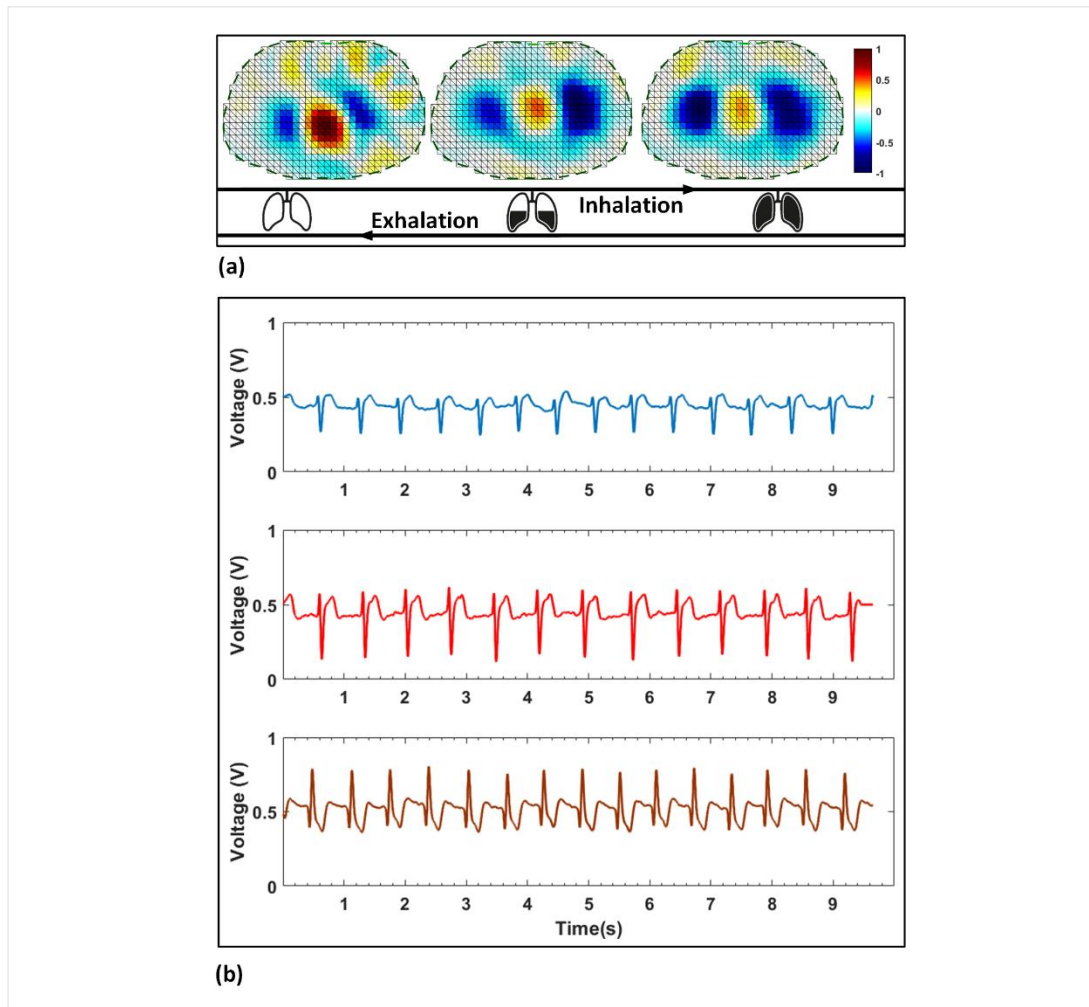






Figure 3.22: EIT in-vivo test with the belt worn by a healthy male volunteer; (a) The exhalation and inhalation lung images where the colour bar shows normalized conductance; (b) ECG signals captured in 30 s switching between three different locations using the EIT system.

² The fabric dressing presented in the section is fabricated by redLoop, Middlesex University London

The belt was covered with the textile dressing and worn by a healthy male volunteer. The volunteer's lung respiration cycle was captured; see Figure 3.22(a). Figure 3.22(b) shows the ECG signal recorded for 30 s, switching between three different locations by selecting different pairs of active electrodes.

Table 3-2 compares wearable EIT systems for lung function monitoring. The system reported here has advantages, not only in terms of electronic design specification, but also in providing more functions for clinical applications.

Table 3-2: Comparison with other work.

Wearable EIT system for lung function monitoring	Dragger [74]	Swisstom [13]	KAIST [79]	This Work
				
Number of electrodes	16 electrodes + 1 reference	32 electrodes	32 electrodes	32 electrodes
Active electrodes	No	Yes	No (Electronics on belt)	Yes
Active electrode configuration	N/A	Active buffer	N/A	Active buffer and current driver
EIT scan pattern	Adjacent	N/A	Adjacent	Programmable
Frequency	80 – 130 kHz	150 kHz	10 – 200 kHz	50 – 500 kHz
Current amplitude	90% of I_{max}^3	50% of I_{max}^3	0.1 – 1 mA_{p-p}	≤ 6 mA_{p-p}
Frame rate	≤ 30 fps	50 fps	≤ 20 fps	107 fps
Heart rate	No	No	No	Yes
Belt orientation	No	Yes	No	Yes
Multi-parameter sensing	No	No	No	Yes

³ Maximum patient auxiliary current conforming to IEC 60601-1.

3.5 Summary

A multi-functional adult wearable EIT system based on active electrode ASIC has been developed, the functions of which will form the basis of a neonatal design. The high amplitude active current driver is capable of 6 mA_{p-p} output with a THD of 55 dB and a high output impedance over 1 M Ω at 500 kHz. The active buffer has a nominal gain of 0.98 V/V up to 750 kHz, with an output swing of 14 V_{p-p}.

The 32-electrode system can provide EIT images at 107 fps and a measurement accuracy of 98.88%. With the replaceable innovative textile dressing, it has been tested on a human volunteer and the lung respiration has been successfully imaged. The system is also capable of recording heart rate signals as well as providing other measurement parameters for clinical purposes.

Chapter 4

Towards the next generation of active EIT system

4.1 Introduction

In the active system, as explained in section 2.3.3.1 unwanted parasitic effects from the multiplexing as well as the cables are isolated compared to the passive system. Many state-of-the-art EIT systems are implemented using such active electrode architecture. Active electrode architecture was proposed in the nineties [65], by simply inserting an active unity gain buffer before multiplexing the signals to the IA. It improves the noise immunity but it can be seen from Figure 2.17 that due to unmatched switching networks and cables in front of the IA, it offers little CMRR improvement. Active amplifiers with gain intimately connected to the electrodes can reduce the noise figure of the analog front-end voltage acquisition [86]. This limits the flexibility of electrode selection for voltage acquisition [87], to recording from only two adjacent electrodes. In this Chapter, a novel active electrode architecture is proposed that overcomes this limitation providing very flexible EIT current drive and voltage sensing patterns with simple digital control and low complexity wiring demand, as well as active gain and higher CMRR.

The system is developed from the CRADLv1.0, and has been significantly enhanced by the introduction of a new active electrode architecture with an improved integrated active electrode ASIC avoiding the use of any active electrode PCB or off-the-shelf ICs. This version, CRADLv2.0, provides further improvement on CMRR, noise performance, and system bandwidth while maintaining a high frame rate and

other important clinical functionalities such as heart rate, and boundary shape detection.

The rest of the chapter is organized as follows. Section 4.2 examines the conventional active EIT architectures and describes the proposed new active electrode architecture. Section 4.3 gives details regarding the ASIC design and the measured results are presented in section 4.4 with the chapter summary in section 4.5.

4.2 System design and implementation

4.2.1 Proposed active electrode architecture

The new active electrode architecture is shown in Figure 4.1. The active electrodes are identical and each uses a fully integrated ASIC. It has five analog switches which are controlled by digital logic. For voltage recording, instead of multiplexing the signals through active buffers, it has an IA in direct contact with the two adjacent electrodes. This approach is a development of the use of the active buffer and provides superior CMRR. In Figure 4.1 the voltage across electrodes 8 and 11 has been chosen as an example of voltage acquisition. Three IAs are switched on to record voltages V_{9-8} , V_{10-9} and V_{11-10} directly from the electrodes, and through MUX4, these voltages are summed by an inverting amplifier (at the bottom of Figure 4.1) that provides $V_{\text{sum}} = V_8 - V_9 + V_9 - V_{10} + V_{10} - V_{11} = V_{8-11}$. Other IAs which are not required for measurement are switched off and their MUX4 switches connected to ground. Although each IA can only measure its dedicated electrode pair, with a summation readout topology, the system is able to access differential voltages across any pair of selected electrodes with only one readout track.

In this design, any pair of electrodes can be chosen for current injection using a source CD+ on one electrode and a sink CD- on a different electrode.

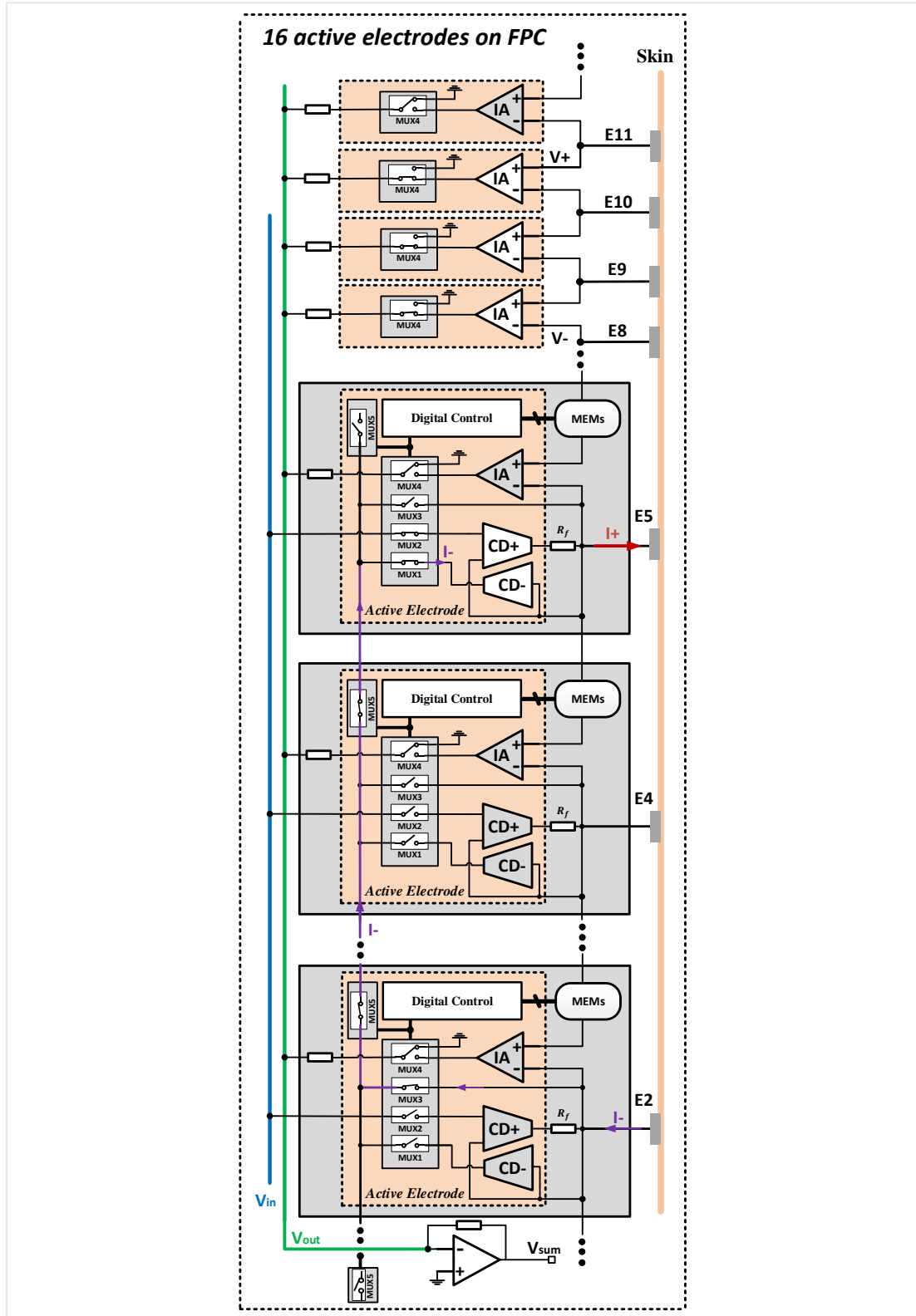


Figure 4.1: Proposed active electrode EIT belt architecture with active current driver, IA and MEMs shape sensors.

During current injection CD+ is excited by an input signal V_{in} via MUX2. In Figure 4.1, electrode 5 (E5) has been chosen to source the current and electrode 2 (E2) to sink it by switching on MUX3. Both source ($I+$) and sink ($I-$) currents are generated by CD+ and CD– in E5. $I-$ is guided by appropriate MUX1, MUX3 and MUX5 switches to E2 to complete the current path (coloured in purple). In a given cycle, only one pair of CD+ and CD– are switched on; the other drivers are switched off.

Also shown in Figure 4.1 is that each ASIC is able to drive a MEMS sensor (ADXL313 by Analog Devices), designed for tracking the individual patient's thorax shape and lying position to aid in EIT model selection [88]. The ASIC can also measure ECG providing added clinical information (see section 4.3.3).

An important consideration in voltage recording is noise within Figure 4.2 shows the models used for analysis of the noise performance of two active voltage recording topologies. As shown, the cascade gain in both topologies is set to be equal. For the active buffer topology the input-referred noise V_{n_buff} is:

$$\begin{aligned} V_{n_buff} &= \frac{\sqrt{2 \cdot A^2 \cdot (e_{n1}^2 + e_{n2}^2) + A^2 \cdot e_{n3}^2}}{A} \\ &= \sqrt{2 \cdot (e_{n1}^2 + e_{n2}^2) + e_{n3}^2} \end{aligned} \quad (4.1)$$

where e_{n1} and e_{n3} is the input-referred noise of active buffer and the IA in the hub respectively, and e_{n2} is the noise coupled to the tracks while transmitting signals back to the hub. Assuming $e_{n1} = e_{n3}$ then:

$$V_{n_buff} = \sqrt{3 \cdot e_{n1}^2 + 2 \cdot e_{n2}^2} \quad (4.2)$$

For the IA summing topology, the input referred noise V_{n_IAS} is:

$$\begin{aligned} V_{n_IAS} &= \frac{\sqrt{m \cdot A^2 \cdot e_{n3}^2 + m \cdot e_{n2}^2 + e_{n1}^2}}{A} \\ &= \sqrt{m \cdot e_{n3}^2 + \frac{m \cdot e_{n2}^2}{A^2} + \frac{e_{n1}^2}{A^2}} \approx \sqrt{m \cdot e_{n3}^2} \end{aligned} \quad (4.3)$$

where e_{n1} and e_{n3} is the input-referred noise of the summing amplifier and active IAs respectively, e_{n2} is the noise coupled to the tracks plus thermal noise of the input

resistors used in the summing amplifier, and m is the number of IAs used for summation.

From the above equations, it can be concluded that if m is less or equal to three, the IA summing topology has less noise than the buffer topology, but if $m \geq 4$, the summing topology has more noise. In EIT measurement, the most frequently used drive pattern is still adjacent drive, with no electrode offset ($m = 1$). Other stimulation patterns have been investigated and the results suggest that polar drive which involves large electrode offsets should be avoided [24]. However, a better image could be obtained with a suitable electrode offset selected for specific targeted applications. Nevertheless, when a high number of IAs are used in summation, a design trade-off is made between CMRR and noise.

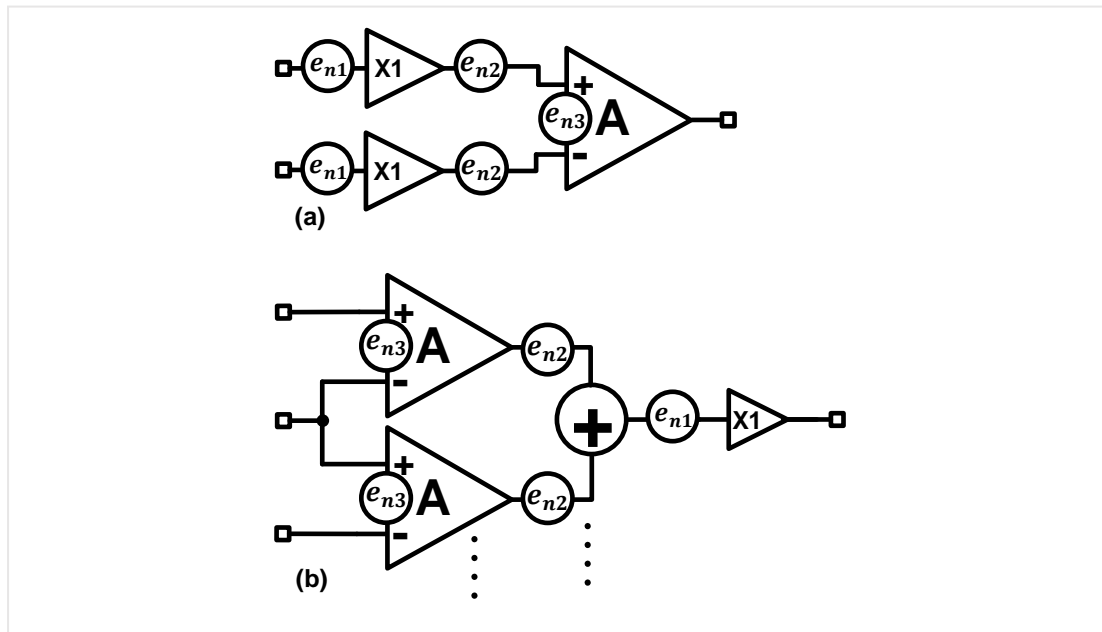


Figure 4.2: Noise analysis of the two active EIT system topologies (a) active buffer topology and (b) active IA sum topology.

4.2.2 Central hub of EIT system¹

Operation control and signal conditioning of the proposed EIT system is carried out in a central hub unit. In operation, the digital control module reads out from a look-

¹ The hub and digital circuit design in this section is a collaborative work with Dr. Dai Jiang, UCL

up table (LUT) a 12-bit data stream of a pre-stored single-tone sinusoidal waveform. The data stream is converted into an analogue sinusoidal signal, V_{in} , by a 12-bit DAC at 32 MSps. This sinusoidal signal excites the current driver in one of the 16 current drivers on the active electrode belt. The address of the LUT readout is programmable so that the frequency of V_{in} can be selected as 125 kHz, 250 kHz, 500 kHz and 1 MHz. The output voltage from the active electrode belt, V_{sum} , is further amplified first by an IA and then a programmable gain amplifier (PGA). The amplified voltage is digitized by a 12-bit ADC at 32 MSps into a data stream, $D(n)$, where the real and imaginary vectors, I and Q , of each electrode voltage readout are derived from $D(n)$ with digital quadrature demodulation. I and Q are sent to a PC for image reconstruction. The digital control module is implemented on a Xilinx Artix-7 FPGA. The operation of the digital control, including LUT readout, ADC digitization, quadrature demodulation and active electrode control, is synchronized by a central state machine operating at 64 MHz. The analogue frontend is built with commercially off-the-shelf components.

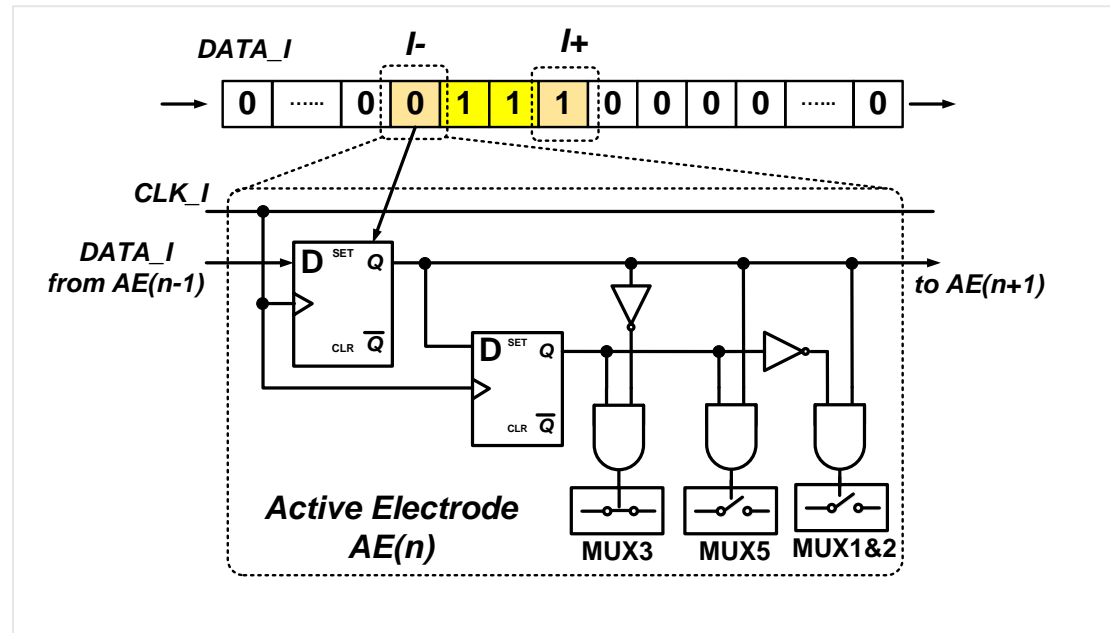


Figure 4.3: Injection control logic in the active electrode (AE).

The active electrode is controlled by two 16-bit stream daisy chains as described in section 3.2.2.1. Figure 4.3 illustrates the active electrode digital control for the

current injection which compares the register current state with the new state to set current drive to source, sink or at idle. The active electrode for voltage recording is controlled by the current bit of $DATA_V$ on each active electrode and at '1' the active electrode IA and MUX4 are turned on. The period of CLK_I is set to 512 μs , with 16 I-rotations, this gives a frame rate of 122 fps.

4.3 Active electrode ASIC

4.3.1 EIT current stimulation

The current driver implemented in this ASIC consists of a source driver CD+ and a sink driver CD- for fully differential drive.

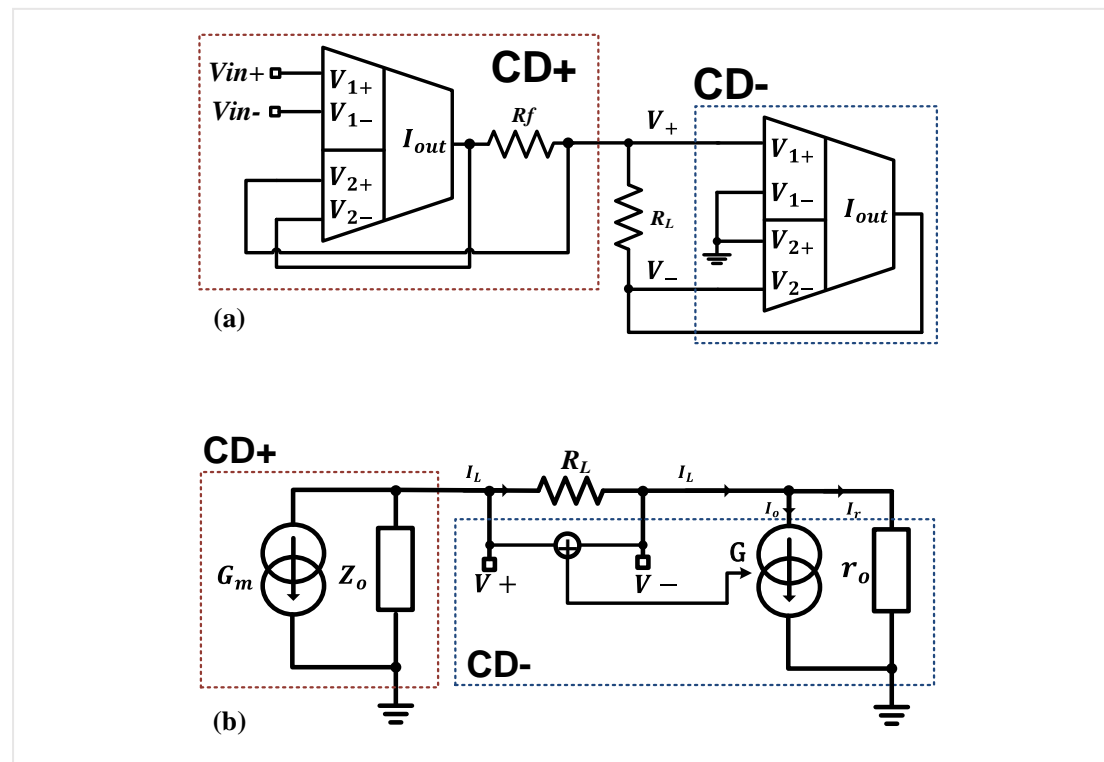


Figure 4.4: The fully differential current driver implemented in the ASIC driving a load R_L .

As shown in Figure 4.4(a), both drivers are based on a four-input transconductance amplifier which is formed by a DDTA and an OTA adapted from section 3.3.1. Each driver has a different feedback configuration. The source driver

CD+ (left) is configured in current feedback, where its output current is set by $G_m = \frac{I_o}{V_{in+} - V_{in-}} \approx \frac{1}{R_f}$ (see Figure 3.8). For the sink driver CD-, its output current is controlled

by measuring the CM voltage across the load and its transfer function can be written as:

$$I_{out} \approx G \cdot [(V_{1+} - V_{1-}) - (V_{2+} - V_{2-})] = G \cdot (V_+ + V_-) \quad (4.4)$$

where G is the open loop transconductance of the four-input transconductance amplifier. With the configuration in Figure 4.4(a), an equivalent circuit can be drawn in Figure 4.4(b), where the CD+ is simplified to a current source with $G_m = \frac{1}{R_f}$ and its output impedance Z_o . CD- has a transconductance of G to sink a current according to the CM voltage across the load and r_o is the impedance seen at its output node.

The current sourced by CD+ flows from the load R_L to the transconductance G , and r_o , thus we have:

$$I_L = G \cdot (V_+ + V_-) + \frac{V_-}{r_o} \quad (4.5)$$

as $I_L \cdot R_L = V_+ - V_-$ and if let $\alpha = 1 + \frac{1}{G \cdot r_o}$, then:

$$V_+ = \frac{\alpha \cdot I_L}{1 + \alpha} \cdot \left(\frac{1}{\alpha G} + R_L \right) \quad (4.6)$$

and

$$V_- = \frac{I_L}{1 + \alpha} \cdot \left(\frac{1}{G} - R_L \right) \quad (4.7)$$

with equation (4.6) and (4.7), the operation of CD- can be written as a function CM voltage:

$$V_{cm} = \frac{1}{2} \cdot (V_+ + V_-) = \frac{I_L}{2} \cdot \left(\frac{1}{G} + \frac{R_L}{2 \cdot G \cdot r_o} \right) \quad (4.8)$$

From the above, it can be seen that CD- employs a common mode feedback (CMFB) to accompany CD+ to achieve the differential current drive.

4.3.2 EIT voltage acquisition

The circuit is formed by two building blocks. A current feedback IA front-end and an output buffer (as described in section 3.3.2) to provide low output impedance and avoid stray capacitance distortion in the connecting tracks. The circuit CMOS level

implementation is shown in Figure 4.5. The IA is based on a current feedback topology [59].

The IA has an input transconductance stage with a source degenerative resistor R_1 . The input stage also has a local feedback current loop M5 to M8. This feedback serves to set the current in M1 and M2 at equal by adjusting the current in MA and MB. The input differential voltage is thus reflected across R_1 which causes a current difference in MA and MB corresponding to this voltage difference.

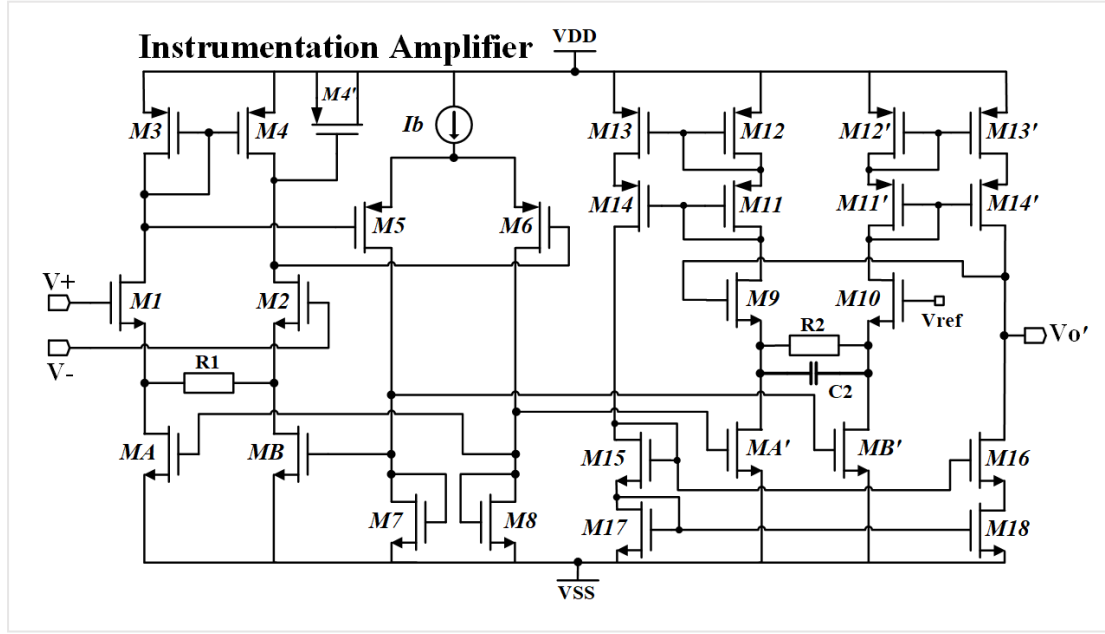


Figure 4.5: Current feedback instrumentation amplifier CMOS level implementation.

At the output stage of the IA, another transconductor mirrors the current difference in MA' and MB' which flows in resistor R_2 . The gate terminal of M10 can be connected to a reference voltage, with $V_{ref} = 0$ V, and by connecting the gate of M9 to the output V_o' , this forms a feedback loop which adjusts the gate voltage of M9 until the current in both M9 and M10 are equal. This results in an output voltage $V_o' = (V_+ - V_-) \cdot \frac{R_2}{R_1}$.

Resistor R_2 and capacitor C_2 set the bandwidth of the IA to $f_{-3dB} = \frac{1}{2\pi R_2 C_2}$.

The input-referred voltage noise of the IA is defined by:

$$\frac{V_{iN}^2}{\Delta f} = 4kTR_1 + 2 \cdot 4kT \cdot \frac{2}{3} \left(\frac{1}{g_{m1,2}} + \frac{g_{m3,4}}{g_{m1,2}^2} \right) \quad (4.9)$$

where g_{mi} is the small-signal transconductance of transistor i , k is Boltzmann's constant, T is the absolute temperature, and the noise is measured over a bandwidth of Δf . From equation (4.9) it is observed that the noise can be minimised by having a small R_1 . In addition, R_1 is also related to the differential input range, defined as $2 \cdot R_1 \cdot I_{d1,2}$. Thus, there is a design trade-off between input range, noise performance and power consumption.

Capacitive mismatch is the primary reason for a limited CMRR in this IA design. To enable a high CMRR at high frequencies, apart from random mismatches which could be reduced by a symmetrical layout, a simple but effective method is to insert a neutralization capacitor, implemented by transistor M4' as shown in Figure 4.5, to equalize the capacitances at the drains of M3 and M4. The ratio of the width of M4' to the width of the current mirror transistors (M3, M4) is set to approximately 4/3 [59].

4.3.3 Heart rate recording and shape sensing

In EIT, the shape information can be used to improve EIT algorithms. Through the multiplexers in the ASIC, the hub can selectively communicate with any MEMS accelerometer for boundary shape detection as shown in Figure 4.6 (a). The boundary shape is detected by calculating the accelerometer tilt angle with respect to earth surface, and because the relative position of each accelerometer is known, boundary shape can be drawn and monitored.

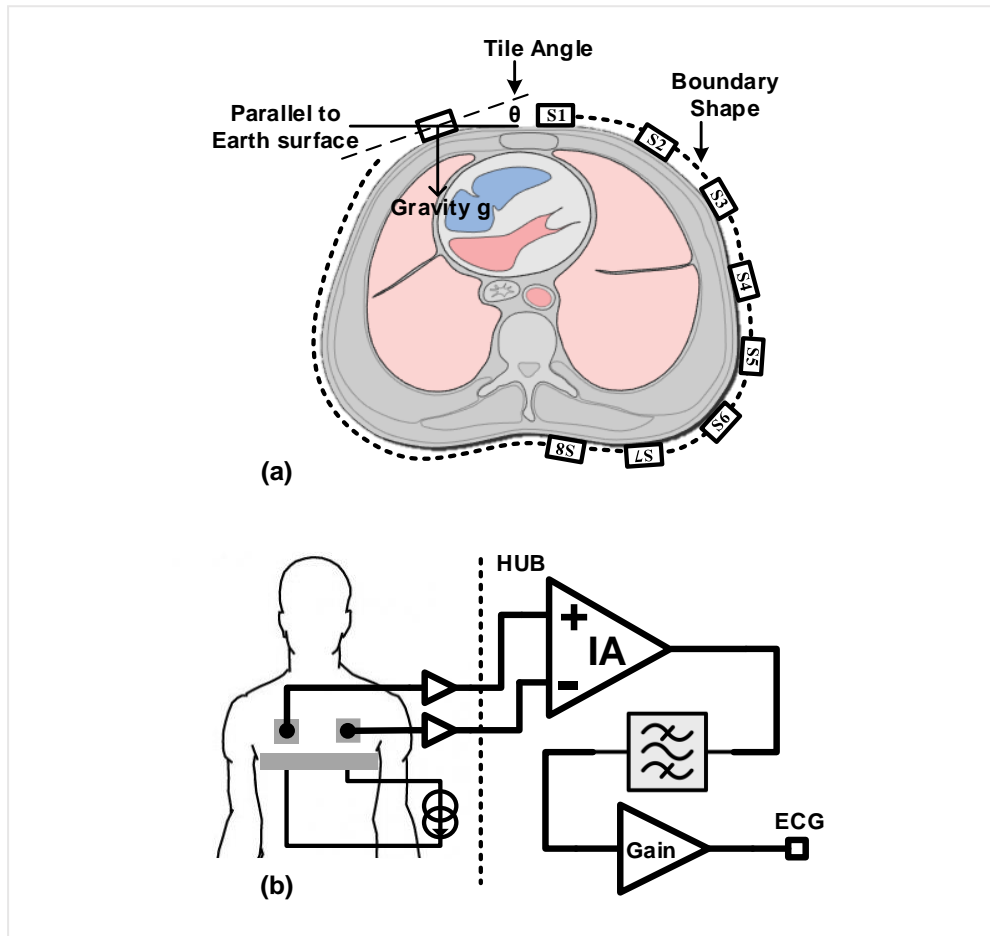


Figure 4.6: (a) Boundary shape detection for EIT model selection using MEMs (b) ECG measurement for heart-rate monitoring.

In each ASIC, there is an extra voltage buffer and by selecting two buffers, an ECG signal can be measured using an IA in the hub to extract heart rate as shown in Figure 4.6 (b). Because the current driver biases the body to a known potential, a third lead is no longer required during the ECG recording.

4.4 Measured results

4.4.1 Active electrode ASIC

The ASIC was designed in 0.35- μm CMOS HV process technology and operates from $\pm 9\text{ V}$ (analog) and 3.3 V (digital) power supplies. The chip micrograph is shown in Figure 4.7 with the various blocks labelled. The total area is $3.1\text{ mm} \times 3.1\text{ mm}$. Table 4-1 summarizes the measured performance of the ASIC.

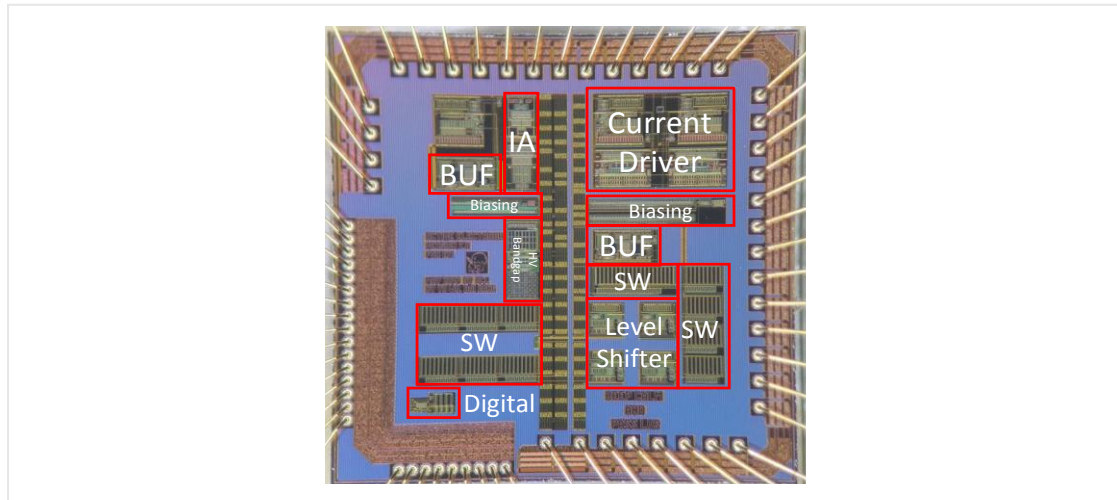


Figure 4.7: Active electrode ASIC micrograph.

4.4.2 System performance test

To verify the system performance, impedance measurement tests were carried out for all possible channels to investigate system measurement accuracy and channel variations. After calibration as specified in section 3.4.2 for each operating frequency, the system was set to measure a parallel R-C load where $R=99\ \Omega$ and $C=2.88\text{ nF}$. For the 16-electrode system, there are 208 channels, and it measures impedances at 125 kHz, 250 kHz, 500 kHz and 1 MHz. The system gives results in terms of the impedance and the phase delay from the R-C load and the measured results are compared to the ideal value.

The measured results are plotted in Figure 4.8 in solid black lines for both impedance amplitude and phase along with the ideal value given in dotted blue lines. Across the frequency band, on average, the system has an impedance measurement accuracy of 98.9%, and a phase measurement accuracy of 98.2% calculated based on the following equation:

$$Impedance\ acc\% = 100\% \cdot \left[1 - \frac{abs(Z_{measured} - Z_{ideal})}{Z_{ideal}} \right] \quad (4.10)$$

and

$$Phase\ acc\% = 100\% \cdot \left[1 - \frac{abs(\theta_{measured} - \theta_{ideal})}{\theta_{ideal}} \right] \quad (4.11)$$

where $Z_{measured}$ and $\theta_{measured}$ is the average value obtained from the 208 channels at each frequency and the final accuracy is the average value from all four frequencies.

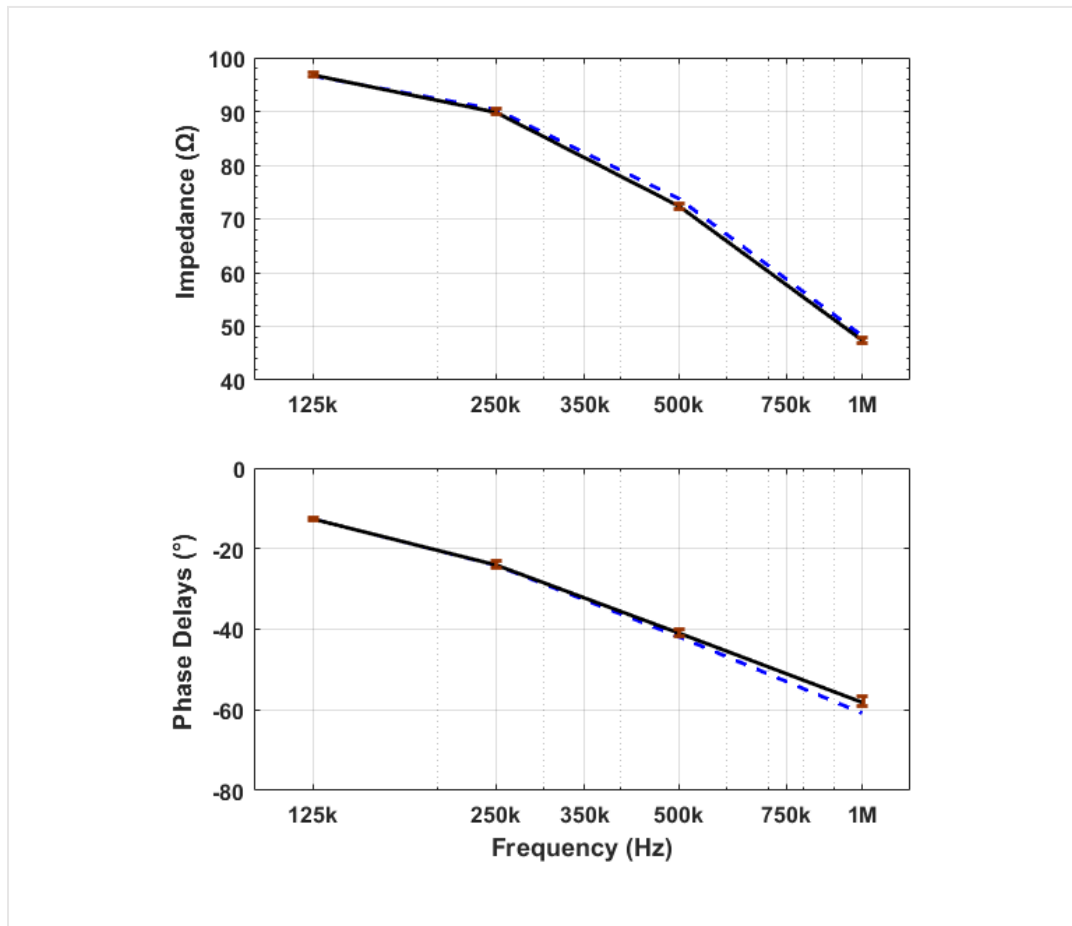


Figure 4.8: System impedance measurement accuracy where the solid black lines are the measured values and blue dotted lines are ideal values.

The red error bars in Figure 4.8 show the maximum spread across all 208 channels at a given frequency. The measurement variance on impedance amplitude is $\pm 0.49 \Omega$ and the phase variance is $\pm 0.77^\circ$.

To illustrate the merit of the proposed active electrode architecture, a comparison is made between three eight-electrode EIT systems using different architectures, namely the passive, active buffer, and the proposed active IA. All three systems were tested on the same resistive phantom [50] which has two diagonal inner resistive elements (see Figure 4.9 for reference) R_L and R_R which represent the ‘objects’ inside the phantom. Figure 4.10 (a) is the EIT image using simulation data as reference for comparison. Figure 4.10(b) is the image obtained from a passive system, Figure 4.10 (c) is the image obtained from an active buffer system, and Figure 4.10 (d) is from the proposed IA based architecture implementation. The active IA is the best match to the ideal.

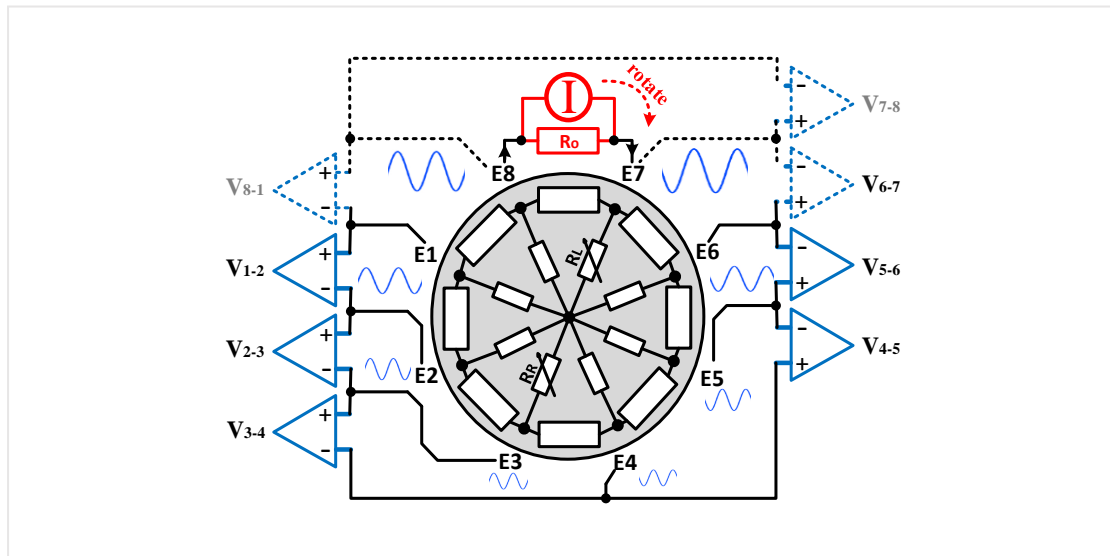


Figure 4.9: Simplified EIT model with both current drive and voltage recording for an eight-electrode system.

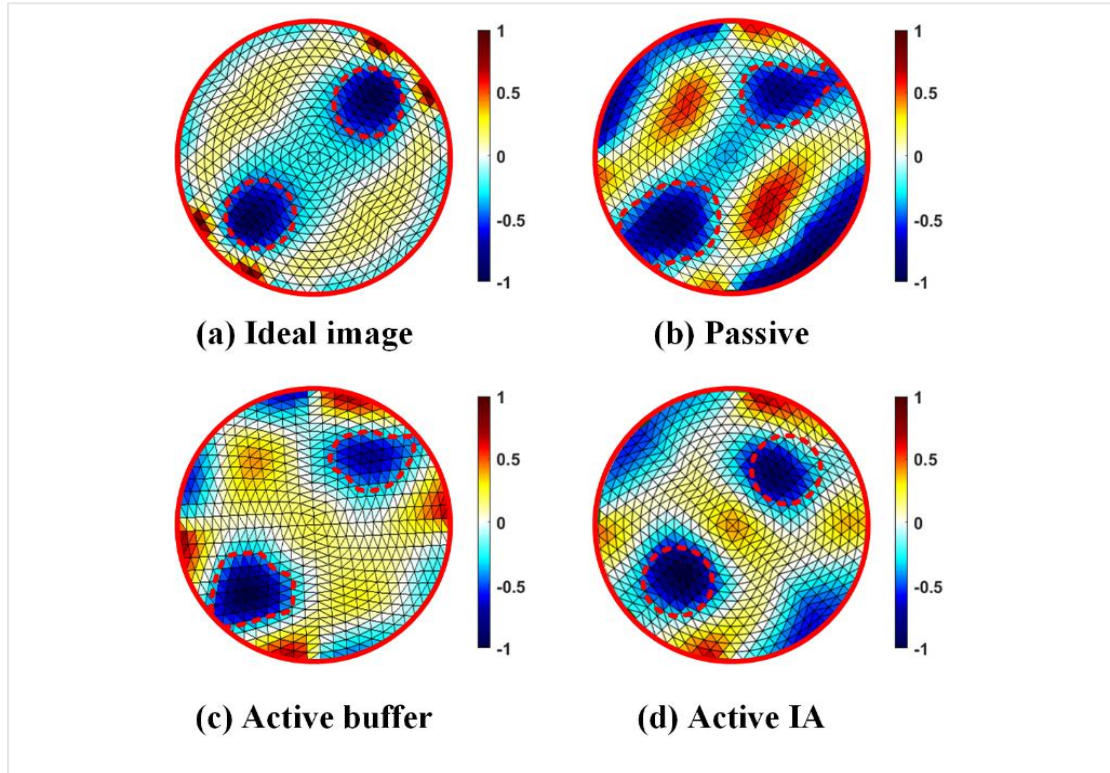


Figure 4.10: Comparison of images that is produced between three different 8-electrode based EIT systems to an ideal EIT image by simulation; (a) Ideal EIT image, (b) Passive EIT (c) Active buffer EIT system (d) Proposed active IA EIT system, the colour bar shows normalized conductance.

For the 16 electrode system imaging test, the phantom is measured from 125 kHz to 1 MHz and the results are shown in Figure 4.11 and Figure 4.12. In the top phantom, two $45\ \Omega$ resistive elements for both R_L and R_R to represent the diagonal phantom 'objects' so that the phantom is purely resistive. However, tissues are modelled as a combination of R-C elements, and for different types of tissues or due to certain clinical conditions, they vary differently with respect to frequency. To illustrate that, as shown in Figure 4.11, for the bottom phantom, it is modified with R_R and Z_R at the two diagonal positions. $R_L = 45\ \Omega$ but Z_R is a R-C parallel impedance where $R = 68\ \Omega$, $C = 21\ \text{nF}$.

As shown in Figure 4.12, the effect of Z_R is demonstrated when multi-frequency images are applied. The phantom 'object' corresponding to Z_R fades away as the frequency increases due to its reactive component. This phenomenon is significant at

1 MHz. It cannot be detected as shown in Figure 4.11 at 125 kHz because the impedance value of Z_R is also $\sim 45 \Omega$ at that frequency. In clinical applications, different tissues or conditions (e.g. pulmonary edema) can be identified by observing the EIT images over a wide bandwidth.

These results not only demonstrate that the proposed system can image accurately up to 1 MHz when compared to the ideal image, but also show the importance of a wide EIT bandwidth for impedance differentiation.

	Transconductance (mA/V)	Bandwidth (Hz)	Phase (at 1 MHz)	Z_{out} (at 1 MHz)	I_{OUT} Maximum	THD (at 1 MHz)	Voltage Compliance
Current Driver	1.99	1 M	12°	507 k Ω	6 mA _{p-p}	43 dB	10 V _{p-p}
	Gain (V/V)	Bandwidth (Hz)	Phase (at 1 MHz)	CMRR (at 1 MHz)	Input range	THD (at 1 MHz)	Input-Referred Noise (Bandwidth)
Instrumentation Amplifier	10.5	1 M	23°	74 dB	300 mV _{p-p}	42.5 dB	25.8 μ Vrms (0.05-1 MHz)

Table 4-1: ASIC measured performance.

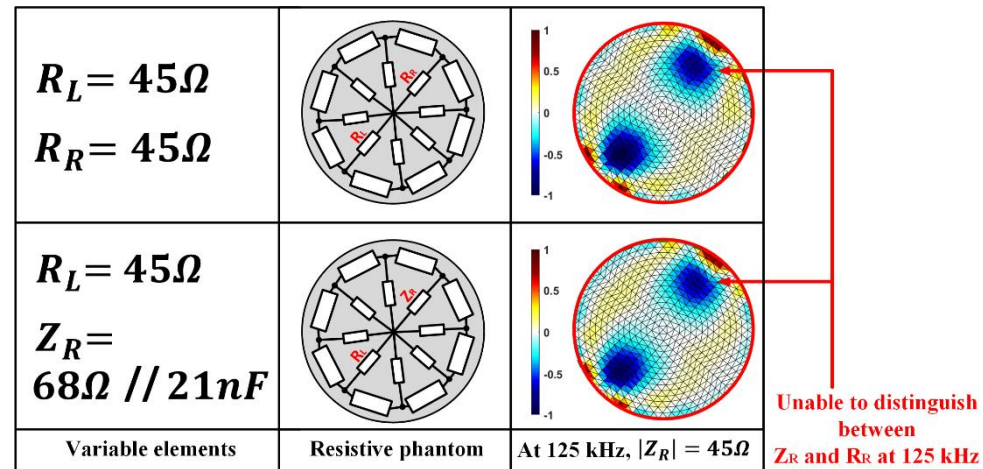


Figure 4.11: The 16 electrode system phantom image results at only 125 kHz; the top phantom has two resistive elements R_L and R_R at diagonal positions. The bottom phantom has one resistive element R_L and an R-C impedance load Z_R at diagonal positions. The colour bar shows normalized conductance.

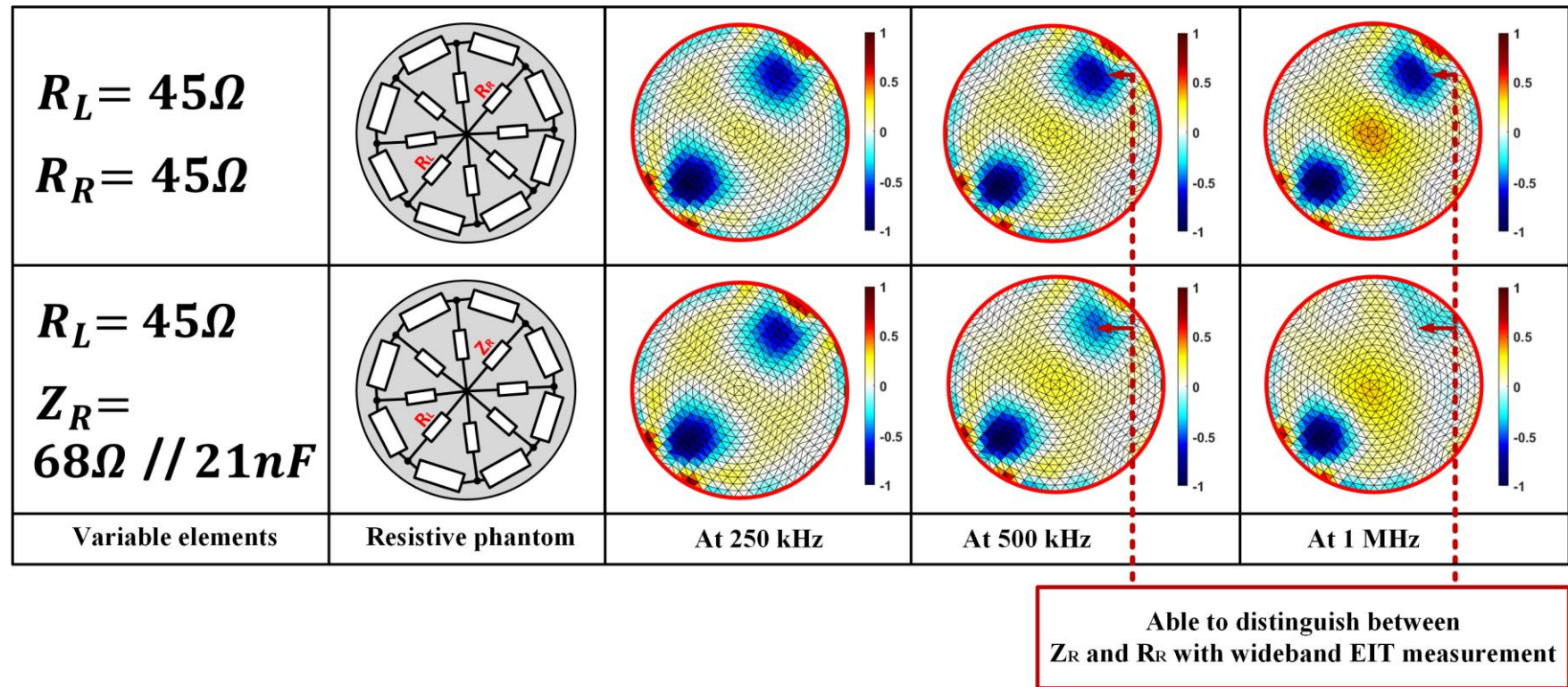


Figure 4.12: The 16 electrode system phantom image results at 250 kHz, 500 kHz and 1 MHz to distinguish between Z_R and R_R , the colour bar shows normalized conductance.

4.4.3 Boundary shape tracking

The shape measurement test is shown in Figure 4.13(a); a variety of contour shapes are created. A test belt containing the ASIC and MEMS is wrapped around these contours for shape measurement, the contour shapes are recorded and compared with the shapes reconstructed from the MEMS. As shown in Figure 4.13 three shapes, circle, oval and torso were tested. The black line is the reference contour and the dotted line is the reconstructed shape with each MEMS sensor labelled. By identifying the sensors, the belt orientation can also be observed. In the torso-like shape in Figure 4.13(d), the belt is rotated by 100 degrees compared to Figure 4.13(c).

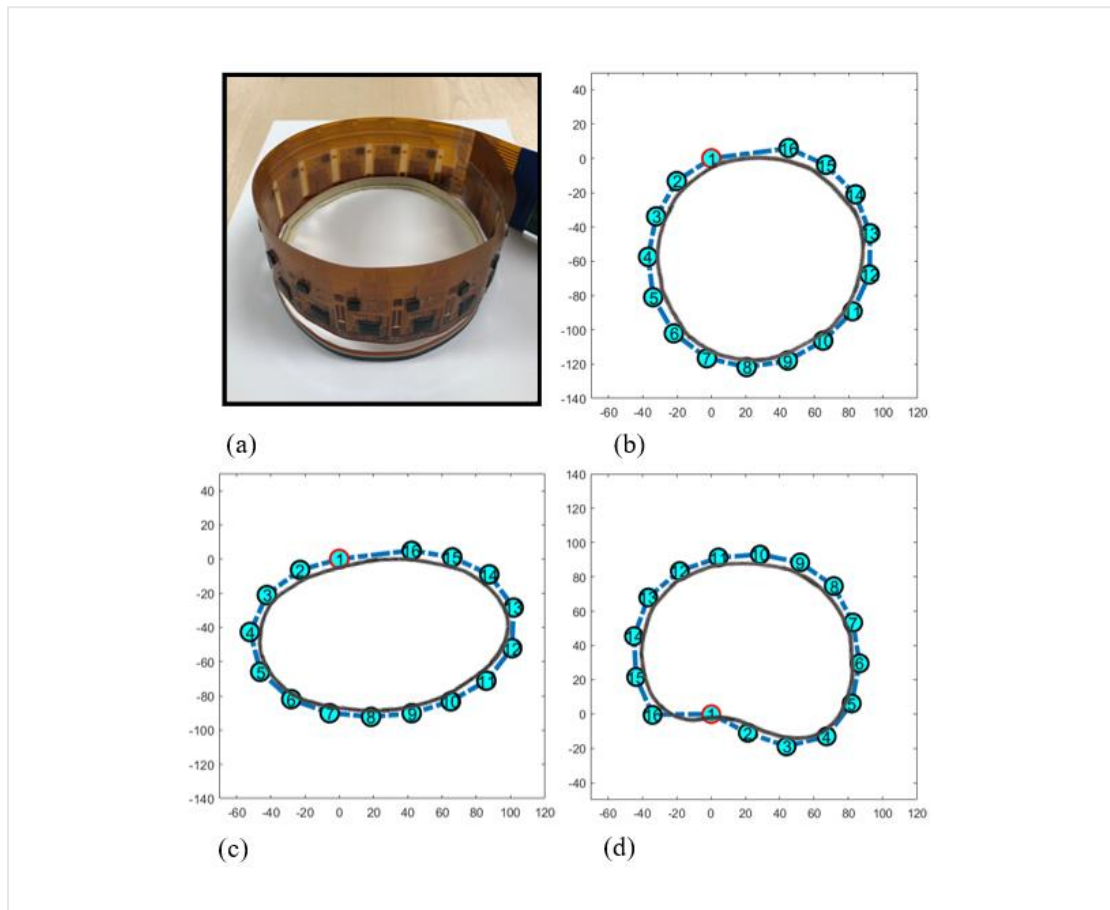


Figure 4.13: Shape measurement (a) the belt is wrapped on the contour (b) Circle shape (c) Oval shape (d) Torso-like shape reconstructed in comparison with the scanned reference where the black lines are the reference contours and blue lines are the reconstructed shape.

4.4.4 System in-vivo validation

The in-vivo test was carried out on a healthy male volunteer using a larger size belt. The belt was covered with the textile dressing and a detailed description of the belt construction is given in Figure 3.21. The volunteer was asked to breathe normally while EIT measurements were taken. Eighty frames of lung respiration EIT images are reconstructed in Figure 4.14(a).

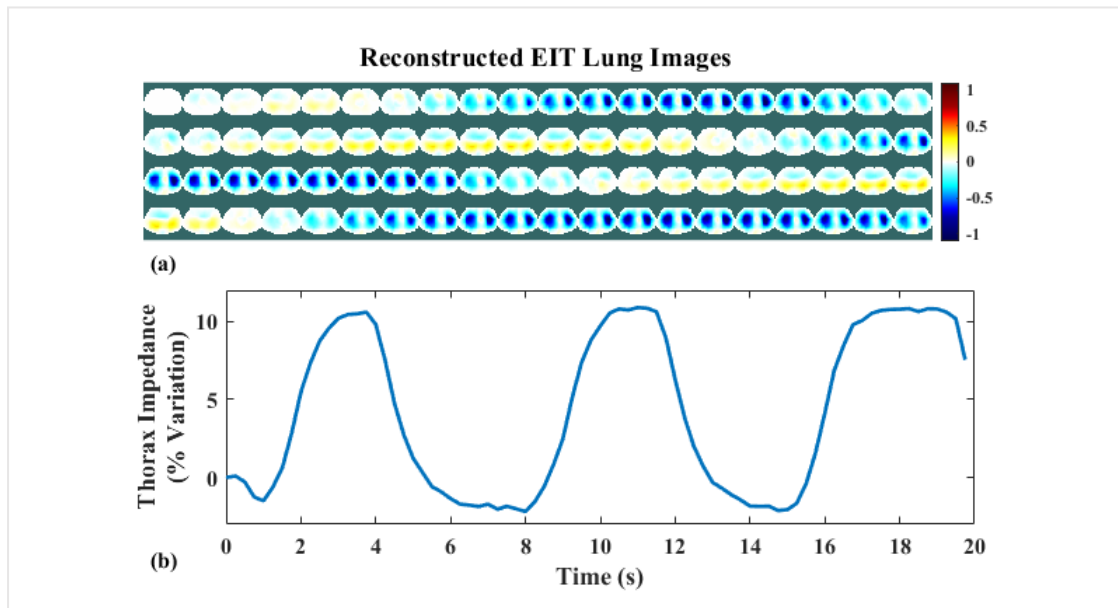


Figure 4.14: The in-vivo measurement results (a) Reconstructed EIT lung images, the colour bar shows normalized conductance. (b) The breathing cycle corresponding to the EIT images.

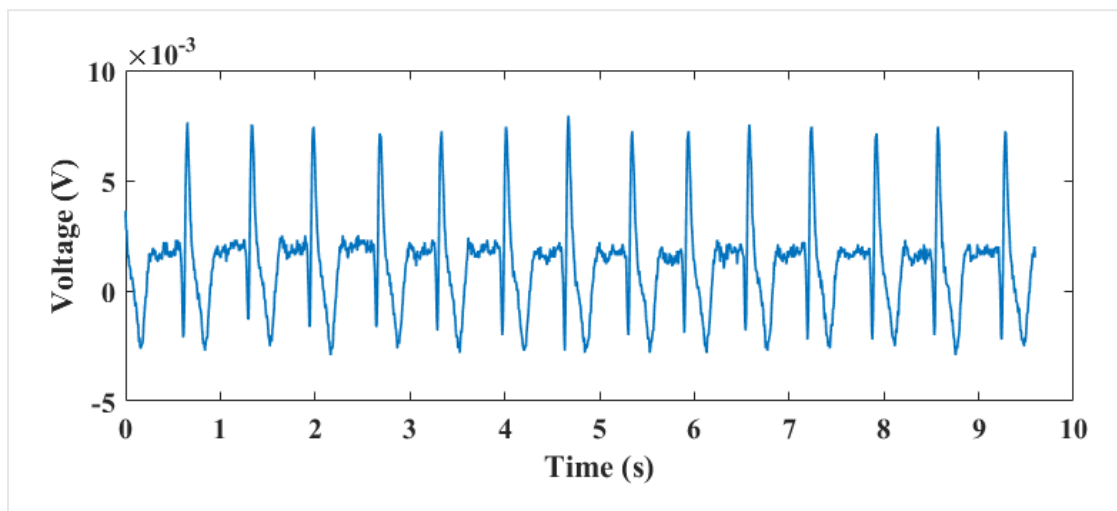



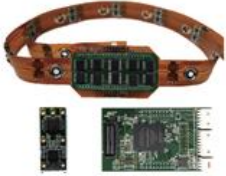


Figure 4.15: The ECG measurement results for heart-rate monitoring.

The EIT images show lung respiration changes in a cross-section view, the colour scale on the right-hand side indicates the conductance variation compared to the reference baseline (the first frame). The colour maps from red to blue indicate the regions that are more conductive (red) or resistive (blue). During inhalation, the lung is inflated, and this results in impedance increments in the chest region. The regions have impedance increments and the level of such increments is illustrated by the area and intensity of blue scaled colours on the EIT image and vice-versa. The thorax impedance variation is with respect to the reference frame, and it is plotted in Figure 4.14(b). It corresponds to the EIT images in Figure 4.14(a) and can be used to identify the breathing cycle, e.g. a longer breath was held after the third inhalation.

The ECG was also measured on the volunteer and the result is shown in Figure 4.15. The ECG signal is recorded for heart rate monitoring.

4.4.5 Comparison with other work

Table 4-2 compares state-of-the-art wearable EIT systems for lung function monitoring. The proposed system is highly integrated with a novel active electrode architecture. This system has the widest bandwidth of 1 MHz and the highest image frame rate of 122 fps. In addition, it offers very flexible programmable electrode patterns for current injection and voltage measurement. It also incorporates other important clinical features in an integrated wearable belt.

Wearable EIT system for lung function monitoring	2015 – Swisstom [13]	2018 – KHU [80]	2018 – CRADL v1.0 [111]	This Work – CRADL v2.0
				
Number of electrodes	32 electrodes	16 electrodes	32 electrodes	16 electrodes
Active electrodes	Yes	Yes	Yes	Yes
Active electrode configuration	Active buffer	Active buffer	Active buffer and current driver	Active IA and current driver
EIT scan pattern	N/A	N/A	Programmable	Programmable
Frequency	150 kHz	11.25 kHz	50 – 500 kHz	Up to 1 MHz
Current amplitude	50% of I_{\max}^1	2.8 mA _{p-p}	≤ 6 mA _{p-p}	≤ 6 mA _{p-p}
Frame rate	50 fps	25 fps	107 fps	122 fps
Heart rate	No	Yes	Yes	Yes
Torso shape tracking	No	No	Yes	Yes

¹ Maximum patient auxiliary current conforming to IEC 60601-1.

Table 4-2: Comparison with other work.

4.5 Summary

A programmable neonatal thorax vital multiple sign monitoring EIT system that is capable of monitoring lung respiration, breathing cycle and heart rate as well as tracking belt position and boundary shape information has been developed. Unlike other active electrode EIT systems, this system has a novel IA based summation architecture with an ASIC providing superior common-mode rejection ratio while reducing the complexity of wiring and digital control. The system has a fast image frame rate of 122 fps, a wide bandwidth of 1 MHz, and multi-frequency capability. It can measure impedance with 98% accuracy within less than $0.5\ \Omega$ and 1° variations across all channels. The EIT image results demonstrated the merits of the new system architecture and the benefit of wideband EIT. Using the system, different shapes were accurately measured and lung respiration EIT images, breathing cycles and heart rate were successfully captured.

Chapter 5

EIT for prosthesis hand control

5.1 Introduction

As a promising HMI approach, sEMG has undergone years of development, especially for hand prosthesis [89], [90]. Reported studies cover topics such as: 1) electronic designs for detection of sEMG using discrete components [91] as well as integrated circuit solutions [92], [93]; 2) electrode materials, placement and number of channels [94], [95]; 3) data processing methods for intent interpretation e.g. using support vector machine [96] and neural networks [97]; 4) myoelectric actuator control profiles such as on-off, and proportional schemes [98] as well as grasp force feedback control [99].

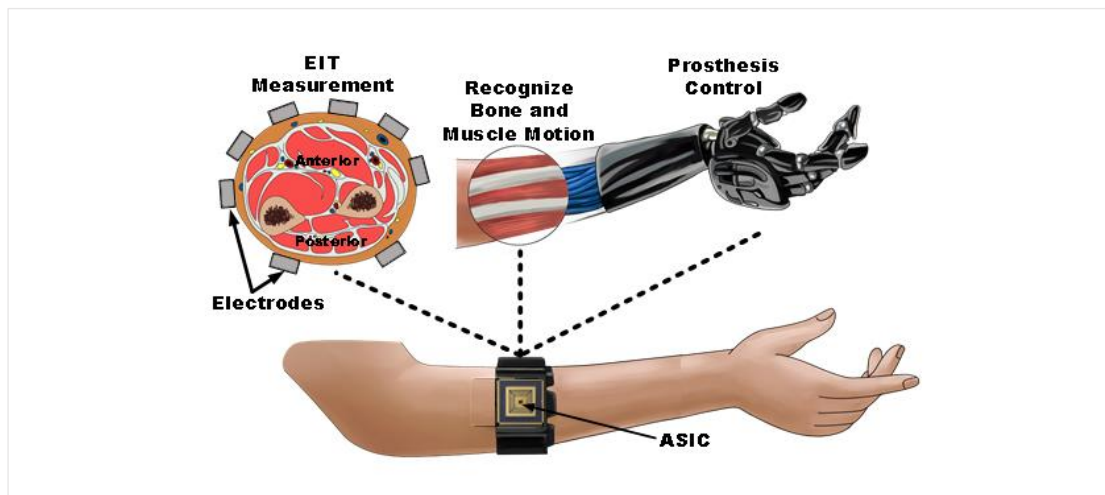


Figure 5.1: Proposed EIT based hand prosthesis control system with ASIC.

However, a significant gap remains in making a seamless HMI for hand prosthesis control, and the fundamental challenges relate to sEMG recording [100]. The sEMG

amplitude is up to tens of mV with frequencies up to about 500 Hz. This makes recording susceptible to noise and low frequency interference. Deep muscle activity in the forearm is also difficult to record using sEMG. This chapter presents a different HMI approach. The proposed system is shown in Figure 5.1 to capture the bone and muscle motion through EIT measurements and uses the data to control a prosthetic hand in real-time.

The rest of the chapter is organized as follows. Section 5.2 presents the detailed system design and implementation. Measured results in section 5.3 which demonstrate the successful operation of the EIT based HMI hand prosthesis system and its medium-term performance. The merits and limits of EIT for HMI hand prosthesis control are also discussed. Summary and remarks are provided in section 5.4.

5.2 System design and implementation

5.2.1 System architecture

The overall system architecture is shown in Figure 5.2. It comprises three parts: 1) hardware EIT system, 2) software on the PC for data processing and pattern recognition, and 3) hand prosthesis control unit. The EIT reader is attached to the wearable wristband and can operate the eight electrodes inside the band.

As shown in Figure 5.2, the front-end ASIC includes a differential current driver, and a current feedback IA designed with low-voltage compliance. The DAC generates a voltage signal, which is filtered and sent to the fully differential current driver in the ASIC. The EIT voltages are measured through the current feedback IA in the ASIC. Following band-pass filtering the IA's output is digitized for I-Q demodulation. After receiving the user input through the UART link, EIT measurements are initiated. On completion, demodulated data carrying hand motion information is transferred back to the PC for pattern learning and then classification. When given a classification, it is

passed on to the microcontroller on the prosthesis hand. The control unit sends out pulse width modulation (PWM) signals to ultimately recreate the same hand grip pattern that the user is performing when EIT measurements are taken.

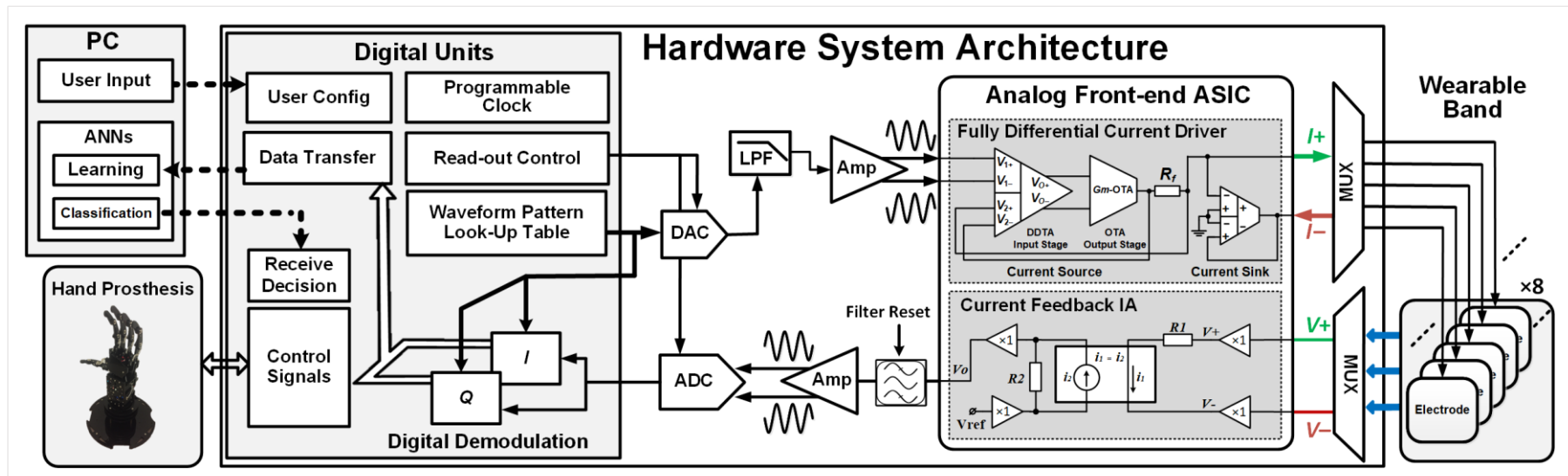


Figure 5.2: Overall HMI system architecture.

5.2.2 Analog front-end ASIC

The current driver block diagram is shown in Figure 5.2 and its corresponding transistor-level schematic is shown in Figure 5.3. Under current feedback, the source current I_+ can be written as:

$$I_+ = (V_{1+} - V_{1-}) \cdot \frac{A_{ol} \cdot Gm_{ota}}{1 + A_{ol} \cdot Gm_{ota} \cdot R_f} \quad (5.1)$$

where Gm_{ota} is the transconductance of the OTA output stage and $V_{1+} - V_{1-}$ is the input voltage of the current source circuit, and A_{ol} is the open loop gain of the DDTA input stage that is enhanced by the cascoded output branch, it is defined as:

$$A_{ol} \approx \beta \times gm_{in} \times \left\{ \frac{1}{\left(gm_7 \times \frac{1}{g_{o6}} \times \frac{1}{g_{o7}} \right) + \left(gm_8 \times \frac{1}{g_{o8}} \times \frac{1}{g_{o9}} \right)} \right\} \quad (5.2)$$

where g_o is the admittance at the drain of each labelled transistor, β is the transistor W/L ratio between $M5$ and $M6$, and gm_{in} is the transconductance of the input stage. $M10$, $M10'$ are biased in the triode region with drains connected to measure and regulate the output CM level. The differential output is connected to the OTA output stage whose output is connected to R_f to provide a linear feedback. The current sink driver is implemented by a two-stage DDTA whose open loop transconductance is $G = \frac{gm_{in}}{g_{o17} + g_{o21}} \times gm_{23}$. The detailed design procedure of the current driver is explained in section 3.3.1 and 4.3.1.

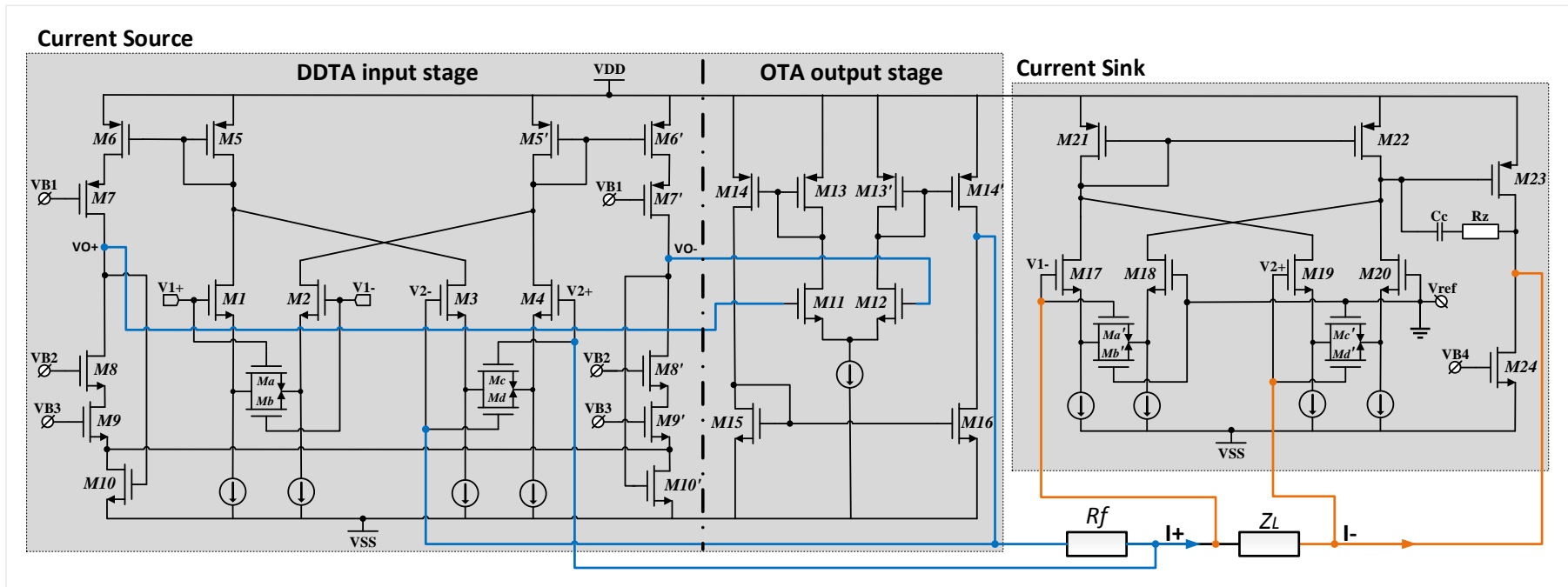


Figure 5.3: Transistor-level schematic of the current driver.

The basic functional diagram of the IA is shown in Figure 5.2. It applies differential inputs to resistor R_1 via buffers, so that the current i_1 is equal to $\frac{V_{in}}{R_1}$. Because i_1 is equal to i_2 , the output voltage V_o is the sum of voltage V_{ref} and the voltage across R_2 provided via buffers. The IA implementation is detailed in section 4.3.2. Given the application, the maximum output current is set to 1 mA_{p-p}, and the linear range of the IA is set to 100 mV_{p-p}. To achieve low power consumption, the biasing current is set to 25 μ A, and R_1 is set to 2 k Ω which gives an input-referred noise of 10 μ V_{rms} over the bandwidth from 25 kHz to 1 MHz. With $R_2=20$ k Ω , the gain of the IA set to 10 V/V.

5.2.3 Digital controls and I-Q demodulation¹

The ASIC is connected to the digital circuits through a pair of data converters and the analog back-end comprising standard analog filters and two single-to-differential amplifiers as shown in Figure 5.2, using off-the-shelf components.

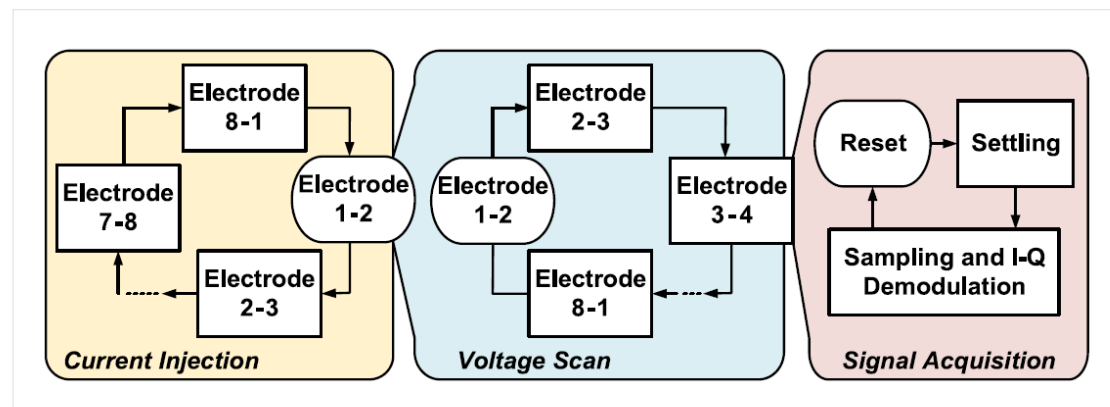


Figure 5.4: State machine for controlling the EIT operation.

The digital circuits control the EIT operation with a state machine comprising three nested loops, as shown in Figure 5.4, managing the electrode scan for current drive, voltage readout, and signal acquisition and processing. The outer loop controls the current drive, which has eight states, each selecting a pair of adjacent electrodes to be multiplexed to the current driver. Each state in the outermost loop triggers the middle loop for voltage scan. The middle loop runs a full cycle before the outer loop

¹ The digital circuit design in this section is a collaborative work with Dr. Dai Jiang, UCL

moves to the next state. The outer loop completes a full cycle to generate one complete dataset. The middle loop also has eight states controlling the multiplexing of eight pairs of adjacent electrodes to the IA. Each state in the middle loop triggers the inner loop for signal acquisition. There are three states in the inner loop. After the middle loop has switched the IA inputs to a new pair of electrodes, the inner loop first resets the band-pass filter in the analog back-end to the reference voltage in order to avoid large signal fluctuation that might require a long settling time. After the reset, the inner loop allows the voltage at the input of the ADC to settle before starting sampling and I-Q demodulation. Once the inner loop completes the sampling and I-Q demodulation state, the middle loop moves to the next state, which triggers a new cycle in the inner loop.

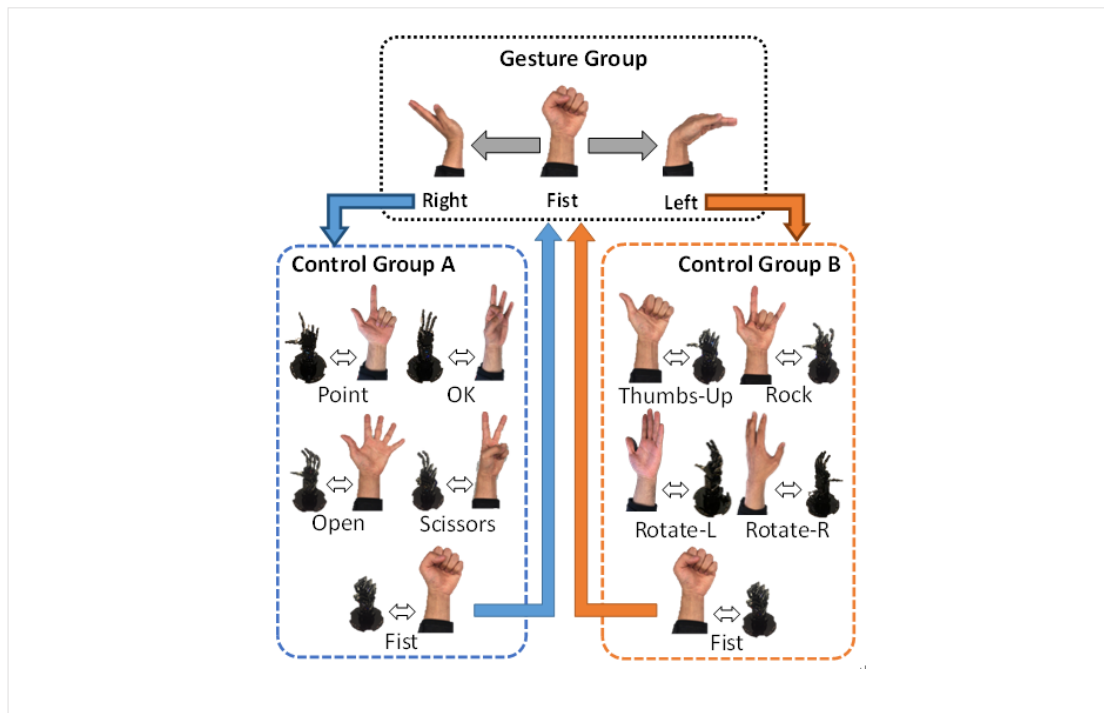


Figure 5.5: Hand prosthesis control with two sub-control groups with gesture enabled switching method.

5.2.4 Hand prosthesis motion control

A servo-motor based hand prosthesis is used in this study. It has six servo-motors of which five are inside the prosthesis arm and are responsible for finger movement and one underneath the holding station for rotating the whole prosthesis hand. The

servo-motor receives the PWM signal to control the angular position of each finger and rotation of the prosthesis arm mechanically according to the duty cycle of the received PWM signal. The PWM signal is generated by an Arduino-Nano microcontroller that is placed on the holding station. For six motors, six PWM signals are used, and their duty cycles are pre-stored inside the microcontroller. Each hand motion (see Figure 5.5) has its own six pre-stored PWM data. Upon receiving the command from the computer, the microcontroller sends out the signals to create the corresponding hand motion on the prosthesis arm.

Nine hand gestures divided into two sub-control groups are proposed that can be recreated by the hand prosthesis, and two other hand gestures (with no corresponding prosthesis motion) to implement the group selection without additional hardware. The control scheme is shown in Figure 5.5. The user can perform 'Left' or 'Right' gesture to select the desired sub-control group. Each sub-control group has five gestures that the user can perform, and 'Fist' is a shared gesture in all groups, to allow sub-group re-selection.

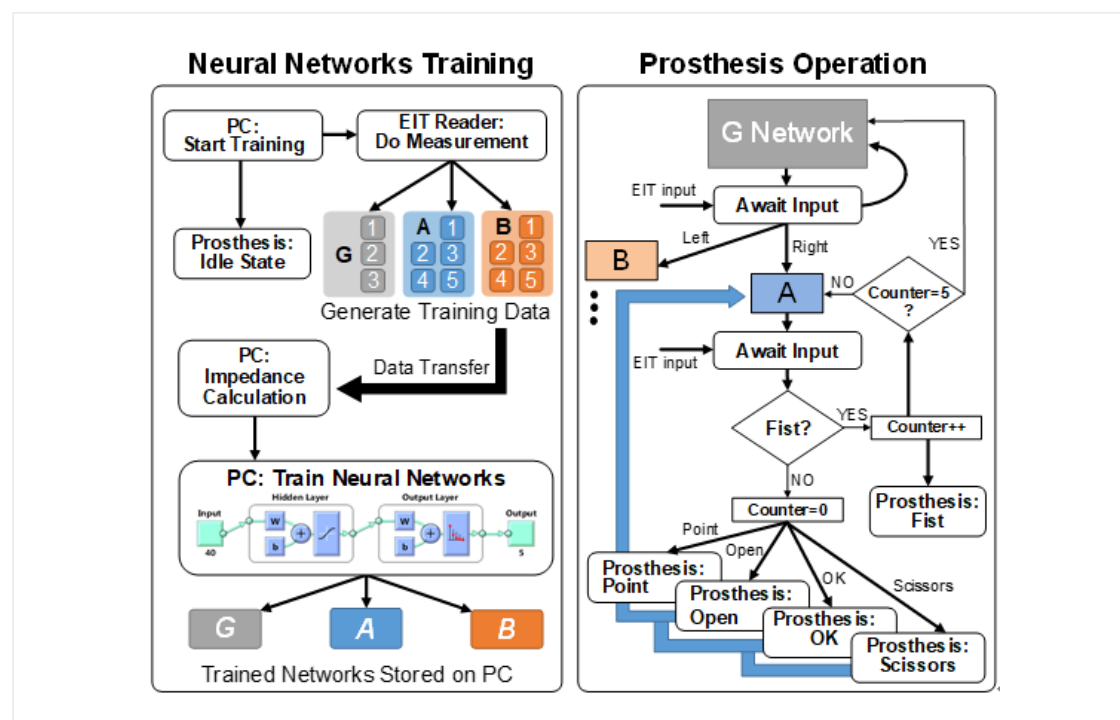


Figure 5.6: System control flow chart for training and prosthesis operation.

Due to individual differences, each user is required to train specific neural networks before their hand motion is recognizable by the system. Figure 5.6 shows the complete system control flow chart. It is divided into two main phases: the data training phase and the prosthesis operation phase. The system uses neural network to recognize the bio-impedance patterns measured by the EIT reader. The neural network is provided by MATLAB's neural network toolbox pattern recognition tool. During the training, the prosthesis hand is in the idle state. The user needs to hold the hand gesture while the EIT reader continuously carries out measurements until sufficient data is recorded.

The system records three sets of data for the 'Gesture' group and five sets of data for each sub-group A and B. Each time the EIT reader takes a measurement, it sends all demodulated I-Q data to the PC where the data is converted to forty bio-impedance values that are labelled and stored for training. Once the stored data is learnt, functions that represent the trained neural networks can be generated and used for classification during the prosthesis operation phase. There are three trained neural networks as shown: G for 'Gesture' group and A and B for the two sub-control groups. Only one neural network is online at a given time.

In the prosthesis operation phase, the EIT reader continuously takes measurements every 200 ms until the user terminates the operation. Measured data is passed to the trained neural network for classification. The system starts with G network as shown in Figure 5.6 and progresses to control group A or B if 'Left' or 'Right' gesture is recognized. The software gives indications as to which group is online and pauses for 3 s when entering a sub-control group, so that the user can re-gesture according to the selected groups. As the flow chart is identical for groups A and B, only A is shown in Figure 5.6. The system employs a counter return method so that when five consecutive 'Fist' gestures are detected, the online trained neural network returns to G with the prosthesis set in the 'Fist' gesture. Until such condition occurs, the system stays in the sub-control group. When another gesture is classified, the counter resets

and the microcontroller operates the hand prosthesis according to the classification output.

5.3 Measured results

5.3.1 Analog front-end ASIC

The ASIC is designed in 0.18- μm CMOS technology and operates from $\pm 1.65\text{ V}$ power supplies. The ASIC micrograph is shown in Figure 5.7 (The function modules occupies a die area of 0.07 mm^2) and the complete EIT reader system.

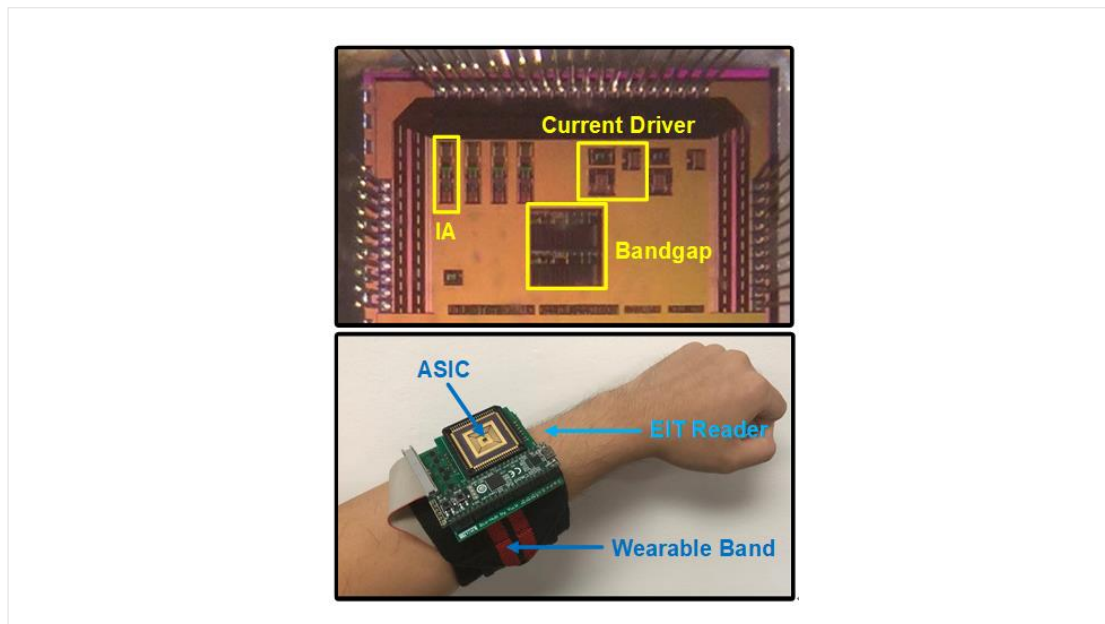


Figure 5.7: ASIC micrograph with individual blocks labelled and the complete EIT reader with the ASIC mounted on a daughter board and a FPGA stacked on top of the motherboard.

The ASIC performance is summarized in Table 5-1. The IA measured maximum differential input signal range is $100\text{ mV}_{\text{p-p}}$, and at 200 kHz the output has a THD of 53 dB . The measured input-referred voltage noise is $9\text{ }\mu\text{V}_{\text{rms}}$ from 25 kHz to 1 MHz . As shown in Figure 5.8 the IA has a gain of 20 dB up to 200 kHz and a CM gain of -60 dB (input CM signal of $1\text{ V}_{\text{p-p}}$), providing 80 dB CMRR at 200 kHz .

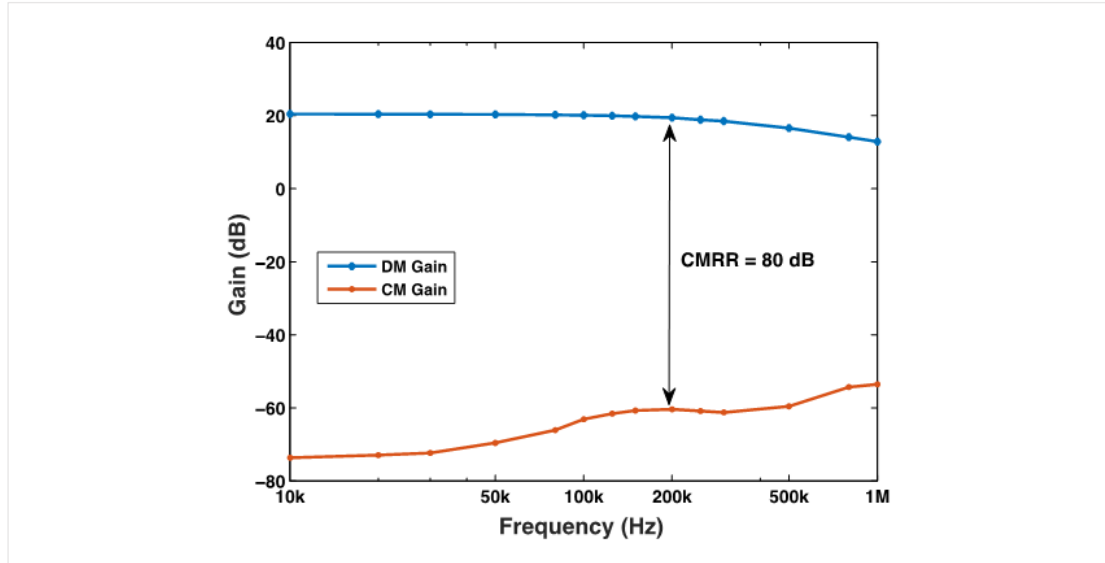


Figure 5.8: Measured common-mode and differential-mode gains of the IA.

The transconductance (and bandwidth) of the current driver was measured by outputting a 1 mA_{p-p} current into a 1 kΩ load; the results are shown in Figure 5.9. The transconductance is maintained at 3.98 mA/V at 200 kHz and with only a 0.5% drop from the initial value at 10 kHz. The measured THD is 42dB and the measured output impedance is 750 kΩ at 500 kHz.

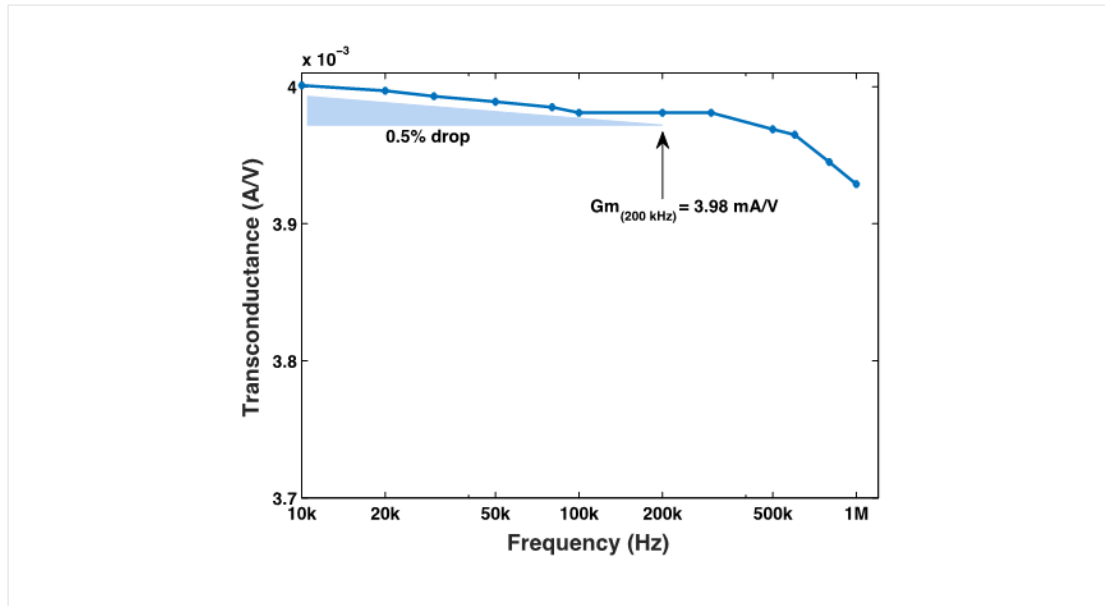


Figure 5.9: Measured transconductance and bandwidth of the current driver with a 1 kΩ load.

Parameter	Current Driver	IA
Gm/Gain	3.97mA/V	10 V/V
Bandwidth	500 kHz	200 kHz
Output current	Up to 1 mA _{p-p}	–
Output impedance	750 k Ω (at 500 kHz)	–
CMRR	–	80 dB (at 200 kHz)
Differential input signal range	–	100 mV _{p-p}
THD	42 dB	53 dB
Input-referred noise (25 kHz – 1MHz)	–	9 μ V _{rms}

Table 5-1: ASIC measured performance.

5.3.2 System testing and results

Five volunteers were recruited, two females and all right handed, for system testing. The wristband was worn on the left forearm and after applying a standard medical grade conductive ECG gel the training could begin (the gel moisturized the skin for better electrical contact). System testing started with gathering data for neural network training. Each volunteer was asked to perform the eleven gestures shown in Figure 5.5 with 150 datasets taken for each gesture. The collected data was then grouped as shown in Figure 5.5 for neural network training. After training was completed, the volunteer was asked to first perform all gestures, starting from group G and entering group A and performing all gestures in the group. Afterward, the volunteer could exit the control group and then re-enter group B to repeat the same procedure. Lastly, the volunteer returned to the ‘gesture’ group. Once this full cycle was completed, the volunteer could perform the gestures at will and the same hand grip pattern could be recreated by the hand prosthesis.

To illustrate how EIT could differentiate between gestures intuitively, a set of measured bio-impedance values were plotted and visually inspected together with a reconstructed EIT image. Shown in Figure 5.10 is the data from the first volunteer as an example. Forty measured bio-impedance values in 50 datasets were normalized and plotted with an EIT image reconstructed using the average of these datasets. By visual inspection, it can be seen that each gesture has its own distinctive patterns reflected on both the bio-impedance plots as well as the EIT images.

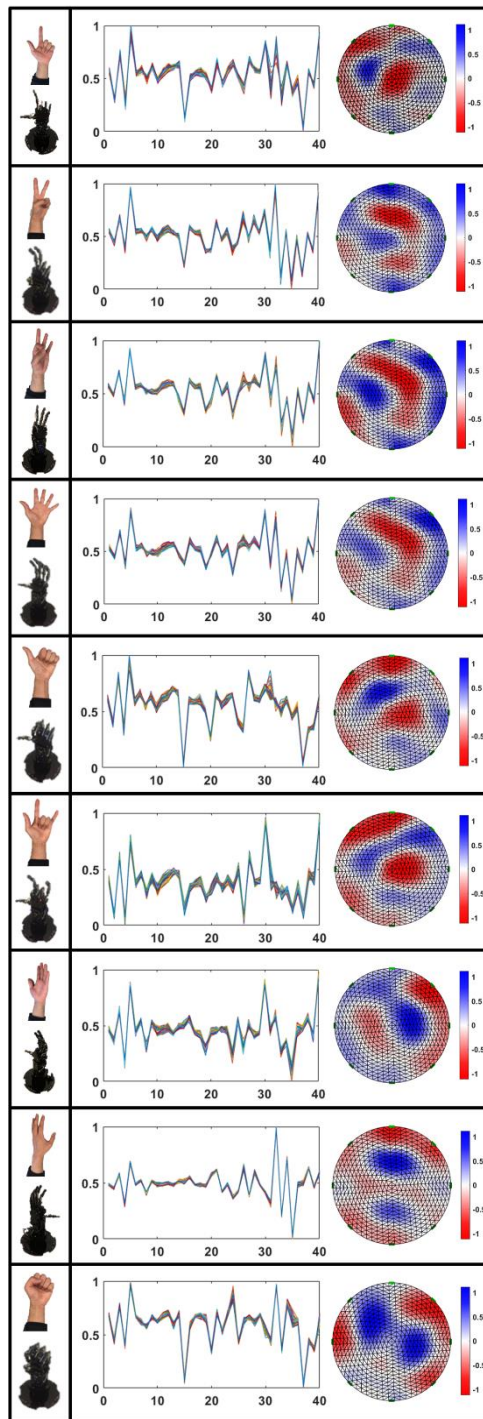


Figure 5.10: All gestures that has corresponding prosthesis motions; and 50 datasets of 40 measured impedance combinations plotted. Using the average of 50 datasets, a corresponding EIT image is produced, the colour bar shows normalized conductance.

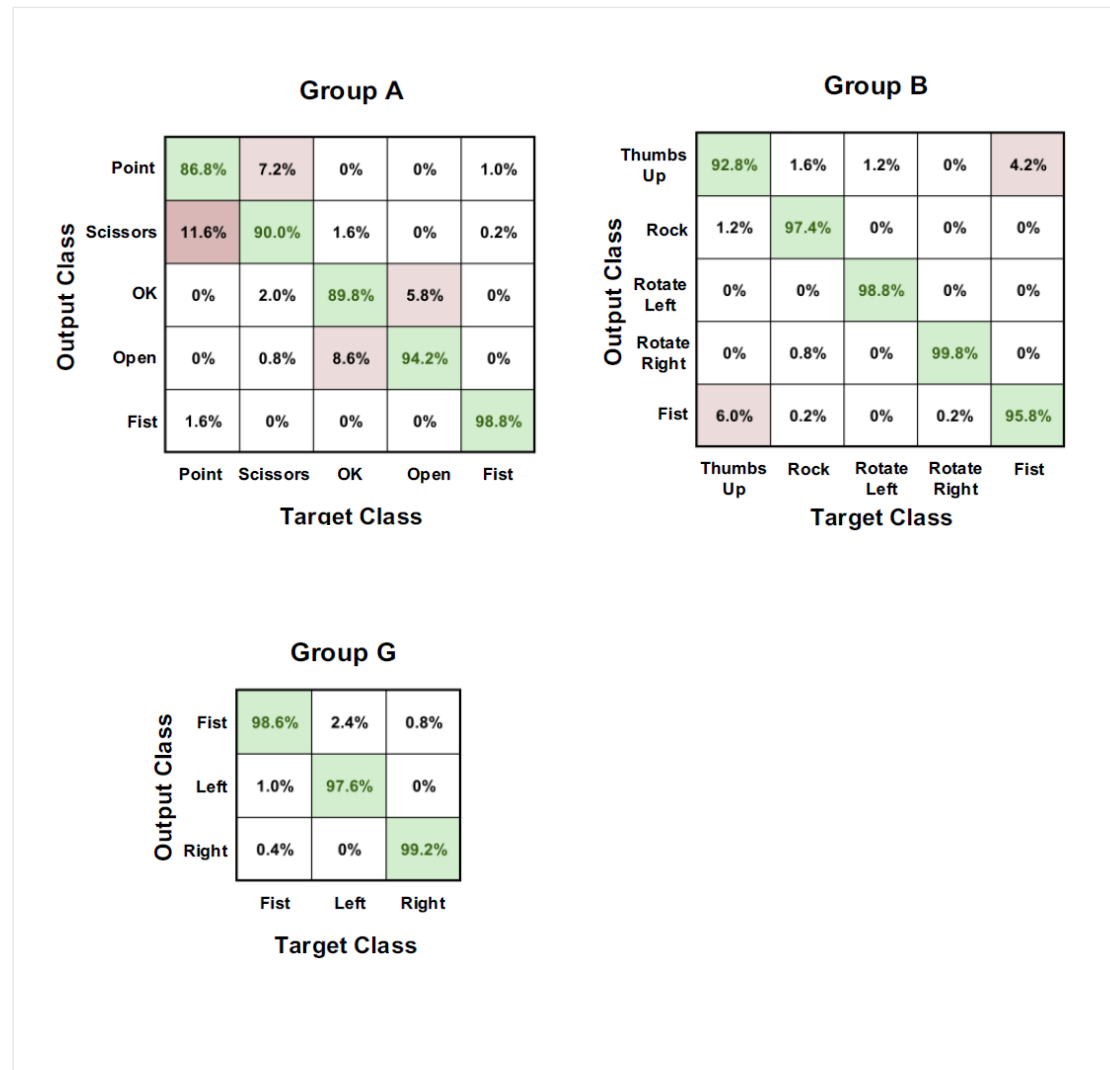


Figure 5.11: Confusion matrixes for the three gesture groups.

The system accuracy was evaluated with the cross-validation method using the 150 datasets previously captured. The first 50 datasets were used to train the neural network. Then an additional test was performed using the remaining 100 datasets. Each volunteer's data produced three confusion matrixes and by averaging the results, three overall confusion matrixes could be obtained as shown in Figure 5.11. G group achieved an accuracy of 98.5% (it is necessary that this group can provide the highest accuracy for sub-control group switching). group A achieved an overall accuracy of 92%, where confusion occurred between 'Point' and 'Scissors' and between 'OK' and 'Open'. Group B achieved an overall accuracy of 97% with little confusion occurring between 'Fist' and 'Thumbs-Up'. Overall, these two groups has an average accuracy

of 94.4%, and with the result of G group, it leads to an overall system accuracy of 95.8%.

Table 5-2 provides a comparison between HMI systems, both using sEMG and EIT, for hand gesture recognition and prosthesis control. For sEMG, the system that uses a similar number of acquisition channels (sEMG requires two electrodes per channel) was selected together with hand gesture pools for comparison. As shown, the HMI system reported in this work has achieved the highest bandwidth, and with the potential to be further integrated into a system-on-chip solution. In terms of classification accuracy, the system developed using EIT as a newly emerged HMI method, it is worthy of comparison to the long-studied sEMG method. Possible merit of using EIT for HMI application is further discussed in section 5.3.4.

Parameter	[89]	[90]	[93]	[22]	[23]	This Work
Channels ¹	6	8	8	8	8 – 32	8
Technique	sEMG	sEMG	sEMG	EIT	EIT	EIT
Hand Gestures	8	7	7	8 + 5 ²	11	5 + 5 + 3
Classifier	LDA	KNN	SVM	SVM	SVM	ANN
Real-Time	No	Yes	Yes	Yes	Yes	Yes
Accuracy	98%	89%	90%	87%	88.5 – 94.3%	95.8%
System Bandwidth	500 Hz	1 kHz	1 kHz	100 kHz	100 kHz	200 kHz

¹ Two EMG electrodes required for one channel recording.

² Gesture multi-groups used. 3 Linear discriminant analysis.

Table 5-2: Comparison with other work.

5.3.3 Preliminary medium-term performance

It was observed that for a single user even with the same pre-defined gesture, a gesture could be performed with differences (e.g. stretch open and relaxed open). As the system measures the bio-impedance alterations, such differences can reduce system accuracy. This behaviour tends to worsen over time as the user is more likely, but unintentionally, to perform the same gesture with differences. To maintain system accuracy, either data from multiple sessions could be used at the start of training or retraining of the neural network over time.

The reliability of the system accuracy was evaluated over multiple sessions. Fifty sessions were carried out by a volunteer; 50 datasets were taken for each gesture and 5 gestures were taken in one session using Group A gestures which had the lowest accuracy in the tests in section 5.3.2. Between sessions, there was a two-minute break. Using these datasets from fifty sessions, the system accuracy was evaluated using four different types of training method. The accuracy is shown in Figure 5.12. The training methods are distinguished by: a) total number of sessions trained; b) retraining used. Their details are listed in Table 5-3. The preliminary results in Figure 5.12 indicate that unintentional gesture variations, which are unavoidable during practical use, can reduce system accuracy. However, this variation could be compensated by using multiple sessions for initial training (occasional retraining also proved to be effective).

Method	Initial Training Sessions	Retraining (Sessions Used)	Total Sessions Trained
1	1 to 5	No	5
2	1 to 10	No	10
3	1 to 3	Once (26 & 27)	5
4	1 to 8	Once (26 & 27)	10

Table 5-3: Details of training methods.

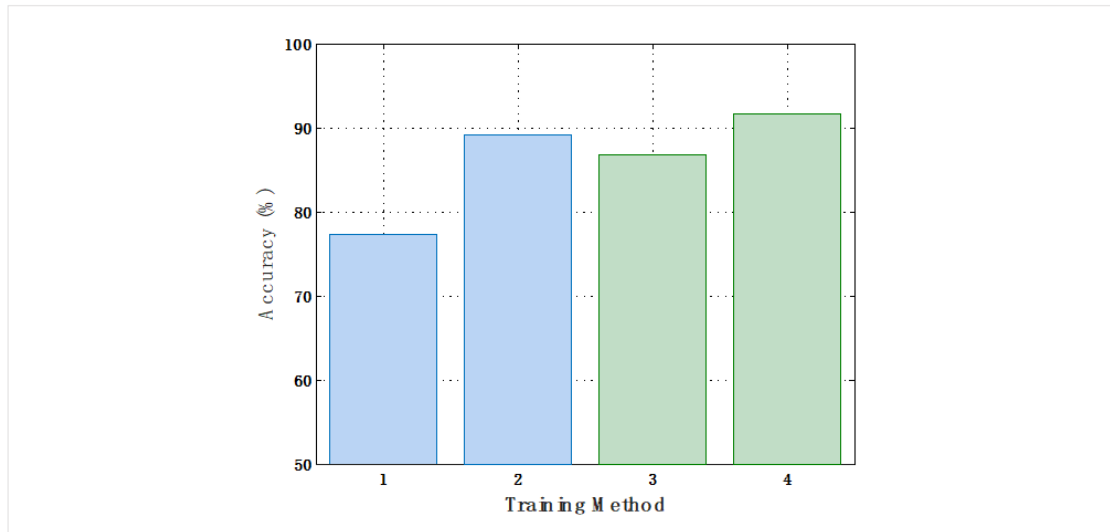


Figure 5.12: Single-user multi-session accuracy test results.

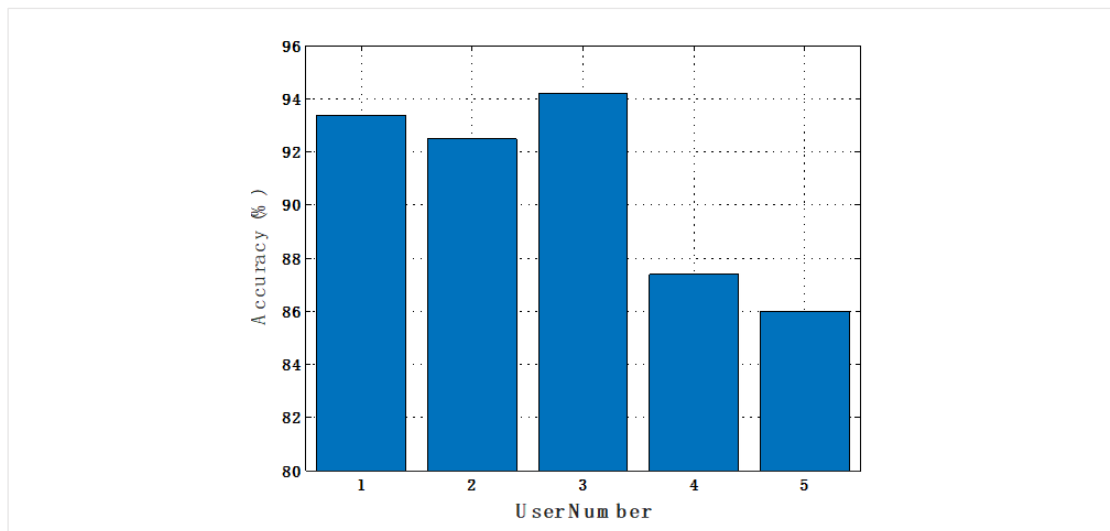


Figure 5.13: Multi-user accuracy reproducibility test results.

The reproducibility of the system was also examined. First, it was investigated whether the accuracy of the results in section 5.3.2 can be repeated over time. For this test, 6 sessions were carried out by 5 volunteers. In each session, 5 gestures were taken and for each gesture 50 datasets were captured for training and 100 datasets for testing, using Group A gestures. Sessions were evenly divided into 3 day intervals with at least 2 hours gap between each session. Using the data from each session for training and testing, the overall accuracy for each user can be plotted as shown in

Figure 5.13. The results suggest that the system performance of the testing in section 5.3.2 is reproducible.

Secondly, the correlation between these 6 sessions was also investigated by using the first 5 sessions as training data to test the last session. The results indicate that there is little correlation between the first 5 sessions and the last session. This suggests that initial training is required each time the user starts to wear the device.

Finally, using datasets from the reproducibility test, all data were combined and sent to 12 different machine learning algorithms for performance comparison using the Classification Learner APP in MATLAB in addition to the artificial neural network (ANN) algorithms. With the default setting, each algorithm was trained, and the test was done using an exported model. The results are summarized in Table 5-4. For each algorithm, the accuracy and computational time are listed. As shown both the support vector machine (SVM) and K-nearest neighbors (KNN) algorithms can reach an accuracy over 90%, but on average KNN tends to require a longer training time. Compared with ANN (with the default setting using 10 hidden neurons) it only takes 1 s for training while offering competitive accuracy; by increasing the neuron size to 100 its accuracy increased to 91.1% while requiring less training time compared with other algorithms. These preliminary results suggest that the EIT datasets are not particularly sensitive to any specific machine learning algorithm. However, it is possible that optimization of a specific algorithm will offer better accuracy with shorter training times in the future.

	Support Vector Machine (SVM)					
Method	Linear SVM	Quadratic SVM	Cubic SVM	Fine Gaussian	Medium Gaussian	Coarse Gaussian
Accuracy	87.3%	91.2%	91.4%	89.1%	89.8%	72.7%
Training Time	9.2 s	6.3 s	6.1 s	9.9 s	12.3 s	18.3 s
	K-Nearest Neighbors (KNN)					
Method	Fine KNN	Medium KNN	Coarse KNN	Cosine KNN	Cubic KNN	Weighted KNN
Accuracy	90.6%	89.7%	73.0%	89.3%	89.3%	89.6%
Training Time	8.5 s	8.3 s	9.0 s	8.1s	198.4 s	14.3 s
Method	Artificial neural network - 10 hidden neurons			Artificial neural network - 100 hidden neurons		
Accuracy	88.8%			91.1%		
Training Time	1.0 s			4.0 s		

Table 5-4: Comparison of machine learning algorithms.

5.3.4 Discussion

The proposed EIT HMI system differentiates hand gestures using the differences in bio-impedance. For the system to work reliably, it is essential that the impedance features measured from each gesture for training have good generality and remain unchanged from session to session. Based on the preliminary results in Section 5.3.3 impedance features can vary due to different ways of performing the same gesture. Fortunately, this alteration can be compensated for a single user. The other likely impedance feature alteration can be caused by different electrode wristband positioning.

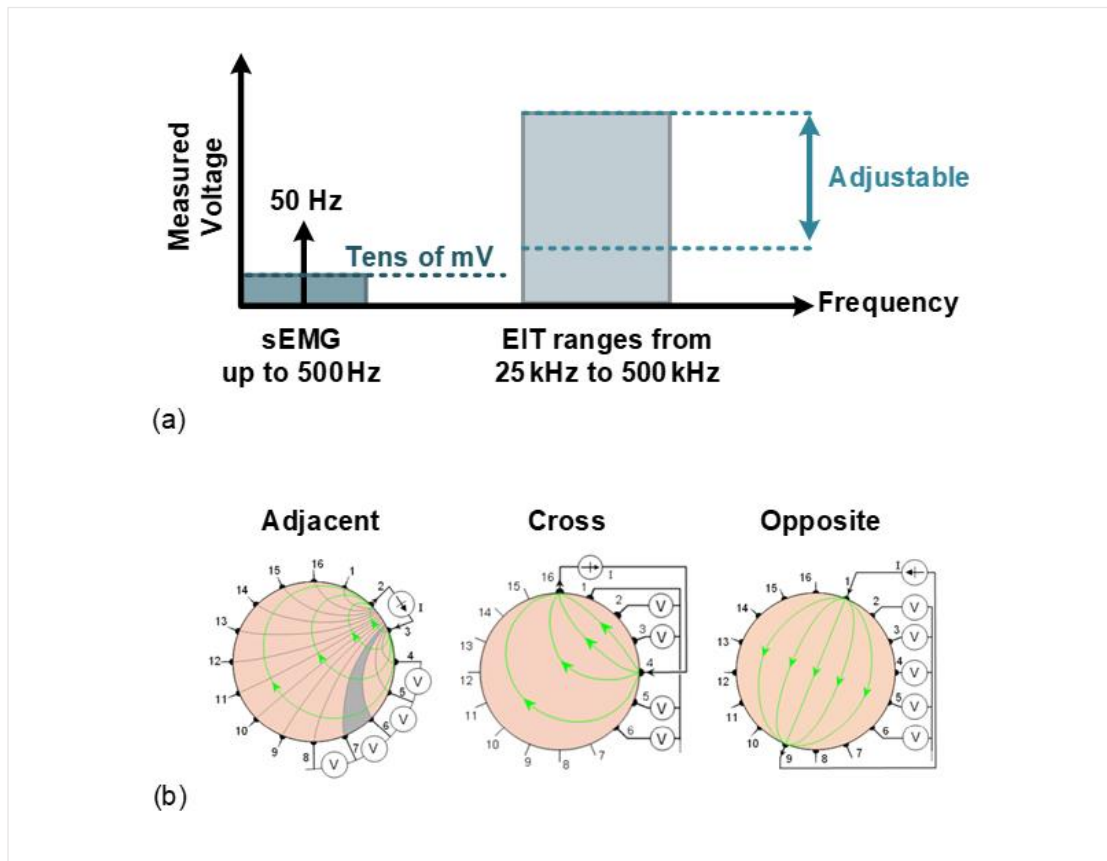


Figure 5.14: Advantages of EIT as an alternative HMI method for hand prosthesis control in terms of: (a) signal bandwidth and strength; (b) different measurement sequences.

For example, the electrodes 6 and 7 in Figure 5.14(b) measure the impedance over the grey shaded area in the first session. In a following session the wristband position will be different, and the position of electrodes is changed. The system

measures different tissue which may possess very different impedance values. Such alteration has been observed during the second part of the medium-term performance where the user not only took off the band from session to session, but also the electrode position was constantly adjusted to fit different users. As a result, even though the system is able to function properly within sessions, little correlation is found between sessions. This leads to an unavoidable initial training each time the band is worn.

Despite the training only requiring a few minutes, it is still a weakness of this HMI system. Given the limited number of sessions of this preliminary study, further work is needed to examine whether these feature alterations due to electrode band positioning could be improved. Similar issues are faced by the sEMG method where electrode position markers are used when carrying out chronic tests [101]. In addition, to improve the system chronic performances, adaptive algorithms [102] and feedback method [103] are also proposed towards solving this open challenge. These solutions may be considered to be transferrable when using the EIT method.

Compared to sEMG whose amplitude ranges up to tens of mV with frequencies up to about 500 Hz, as shown in Figure 5.14(a), the frequency and the amplitude of measurable voltages in EIT are directly related to the current drive which is user programmable in the range from hundreds of $\mu\text{A}_{\text{p-p}}$ to a few $\text{mA}_{\text{p-p}}$ and in a bandwidth from 50 kHz up to 1 MHz. This means the amplitude of the induced measurable signal is adjustable in favor of producing a higher signal-to-noise ratio. Also as the frequency of the signal is tunable, it can be moved away from the low-frequency interferences, such as the 50 Hz mains, which makes the system more robust. In addition, as different types of human tissue, e.g. bone, fat or muscles, feature different values of bio-impedance due to their biological structures, with EIT they can be differentiated at different frequencies [2]. Interrogation of tissues with a wide and tunable bandwidth could offer more information. EIT can also operate with different measurement sequences [104]. It could interrogate different or deep muscle groups with different

sequences for more in-depth analysis as shown in Figure 5.14(b). Finally, EIT could not only offer high-resolution electrode arrays but also multi-plane measurements [otherwise known as three-dimensional (3D)] EIT [105]) which could gather impedance variations at different arm positions simultaneously. Impedance frequency differentiation, exploring measurement sequences and high-resolution multi-plane (3D) EIT hardware upgrades, as well as a performance comparison between sEMG and EIT will be the subject of future investigation.

5.4 Summary

In this chapter, an HMI based on EIT technology has been developed. The EIT reader uses an integrated ASIC that consists of a fully differential current driver and a low noise, high CMRR IA. When integrated into the EIT reader, it can accurately capture the user's forearm inner bio-impedance redistribution, providing both real and imaginary impedance readings to the PC for pattern recognition and feature extraction using an artificial neural network. The system can recognize eleven hand gestures with a gesture enabled sub-grouping method to enlarge gesture pool sizes while ensuring recognition accuracy with minimum influence on user experiences. Experiments have shown that the system can achieve 98.5% accuracy with a grouping of three gestures and an accuracy of 94.4% with two sets of five gestures. A complete HMI system based on the EIT principle for hand prosthesis control has been presented, and its medium-term performance investigated including a preliminary analysis over different types of machine learning algorithm. The merits as well as the limits of EIT as an HMI system have also been discussed and future work proposed. Moreover, for hand prosthesis controls applications, with more sophisticated tools, in-depth studies can be carried out e.g. producing dextrous prosthesis hand for the amputees that could better-

reducing phantom pains [106], or possibly monitoring the muscle movement chronically as the indication for pathological progression.

Chapter 6

Conclusion and future work

6.1 Conclusion

In this thesis two important research topics have been pursued: 1) Development of a wearable and multi-functional EIT system for neonate lung respiration, breathing cycle, and heart-rate monitoring. 2) Using the EIT technique as a new bridge for human-machine interface.

For neonatal lung respiration research, a neonatal thorax vital multiple sign monitoring EIT system that is capable of monitoring lung respiration has been presented. The system features a highly integrated ASIC as active electrode for differential current drive and voltage recording. Unlike other active electrode EIT systems, this system has a novel IA based summation architecture which offers lower noise, and superior CMRR while reducing the complexity of wiring and digital control. The merit of such system architecture has been demonstrated. This system has a fast image frame rate of 122 fps, a wide bandwidth of 1 MHz, and multi-frequency capability. It can measure impedance with 98% accuracy within less than $0.5\ \Omega$ and 1° variations across all channels. The system also demonstrated the breathing cycle and heart rate functionality during in the *in-vivo* test along with lung exhalation and inhalation EIT images captured. The system can also track belt position and provide boundary shape information. A number of test shapes have been successfully reconstructed. Subject to further optimisation, this neonatal system will be tested in a paediatric hospital later in 2019.

For human-machine interface research, a wearable EIT device that uses an ASIC consisting of a fully differential current driver and a low noise, high CMRR IA has been developed. The system can accurately capture the user's forearm bio-impedance redistribution, providing both real and imaginary impedance readings to the PC for pattern recognition and feature extraction using an artificial neural network. The system achieves a recognition accuracy of 95.8%. The medium-term performance has been investigated, suggesting that the system has a reproducible accuracy over time, and re-training from period to period can improve the system reliability. Furthermore, a preliminary analysis has been carried out over different types of machine learning algorithms which suggested that the EIT data is not sensitive to a specific algorithm. Future work would entail examination whether the frequency features from bio-impedance measurements could provide more information for gesture differentiation, and whether combining different EIT scan patterns could lead to more reliable results.

The work presented in this thesis has focused on circuit integration using CMOS technology towards better and successful system performance while offering small size for applications in wearable devices. The work emphasizes the importance of system level integration, by not only proposing new circuit designs but also novel system architectures for EIT hardware. This work is application driven, and with further multi-disciplinary effort will enable its full *in-vivo* and *in-vitro* testing and system evaluation.

6.2 Novel CMOS circuits for future EIT systems

6.2.1 Power-efficient EIT current driver with PWMs

6.2.1.1 Motivation

The current driver designed in this work provides good performance, but it suffers from high power consumption due to multiple biasing current paths. For low power design, the H-bridge based current mirror topology is often implemented [107]. As shown in Figure 6.1, it uses two independent PMOS and NMOS current mirrors to source and sink the current across the load with a DAC control, this open loop topology suffers from current mismatch due to process variations [108].

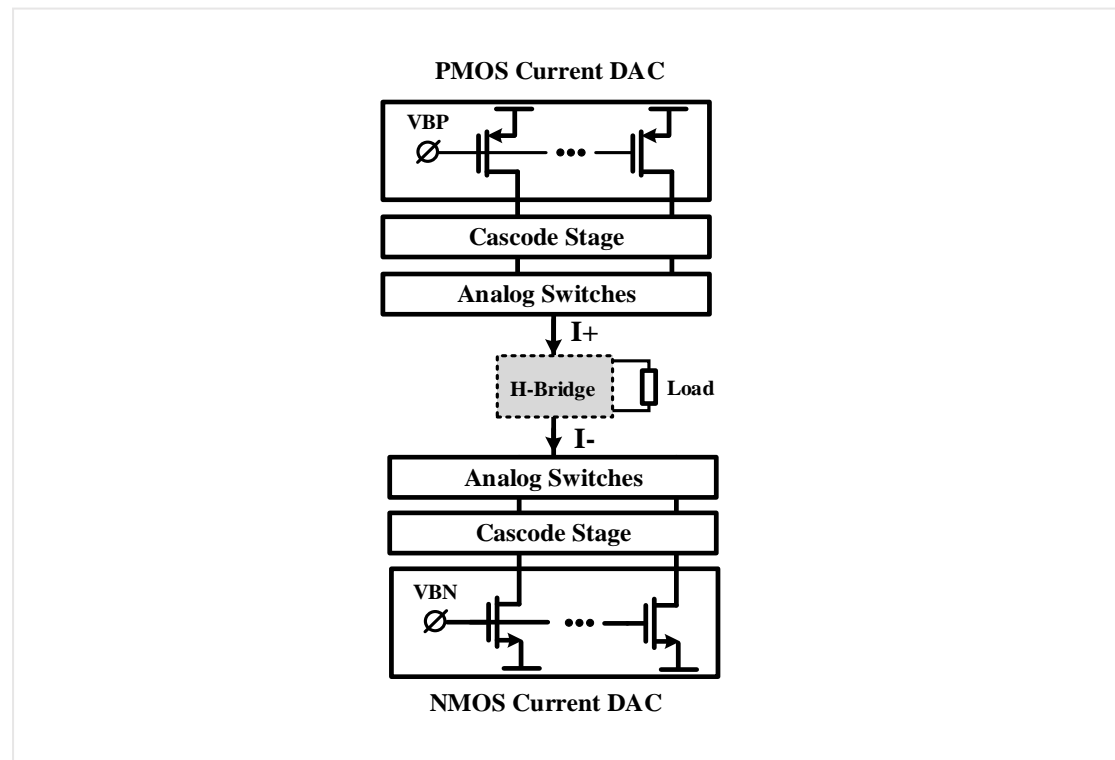


Figure 6.1: Conventional H-bridge based current generator with current mirror DAC.

In this section, a new design is proposed based on the H-bridge topology and features low power. Compared to the conventional H-bridge driver, it incorporates linear feedback while actively cancels CM signals. The current into the load is a PWM sinewave through the switched H-bridge.

6.2.1.2 Circuit design

The circuit implementation of the proposed current generator is shown in Figure 6.2. The source current is provided by a single PMOS transistor M0 in the current feedback loop. The IA measures the current through R_f and opamp-A provides feedback to adjust the gate voltage of M0 towards a 'virtual short' which causes the feedback voltage across R_f to be equal to V_{in} . The transconductance for the source current generator is:

$$G_{m_{source}} = \frac{A_{ol} \times G_{m_{M0}}}{1 + A_{ol} \times G_{m_{M0}} \times A_{IA} \times R_f} \approx \frac{1}{R_f \times A_{IA}} \quad (6.1)$$

where A_{IA} is the IA gain, A_{ol} is the open loop gain of opamp-A, and $G_{m_{M0}}$ is the transconductance of transistor M0. As a result of the feedback loop, the output impedance of the source current generator is $A_{ol} \times G_{m_{M0}} \times R_f \times r_{o_{M0}}$ which is much larger than a simple cascode current mirrors as (used in Figure 6.1) while offering a wider voltage compliance of $V_{cc} - V_{ov_{M0}} - I_{out} \times R_f$. The sink current is also provided by a single NMOS transistor M1 offering a voltage compliance of $V_{ss} - V_{ov_{M1}}$.

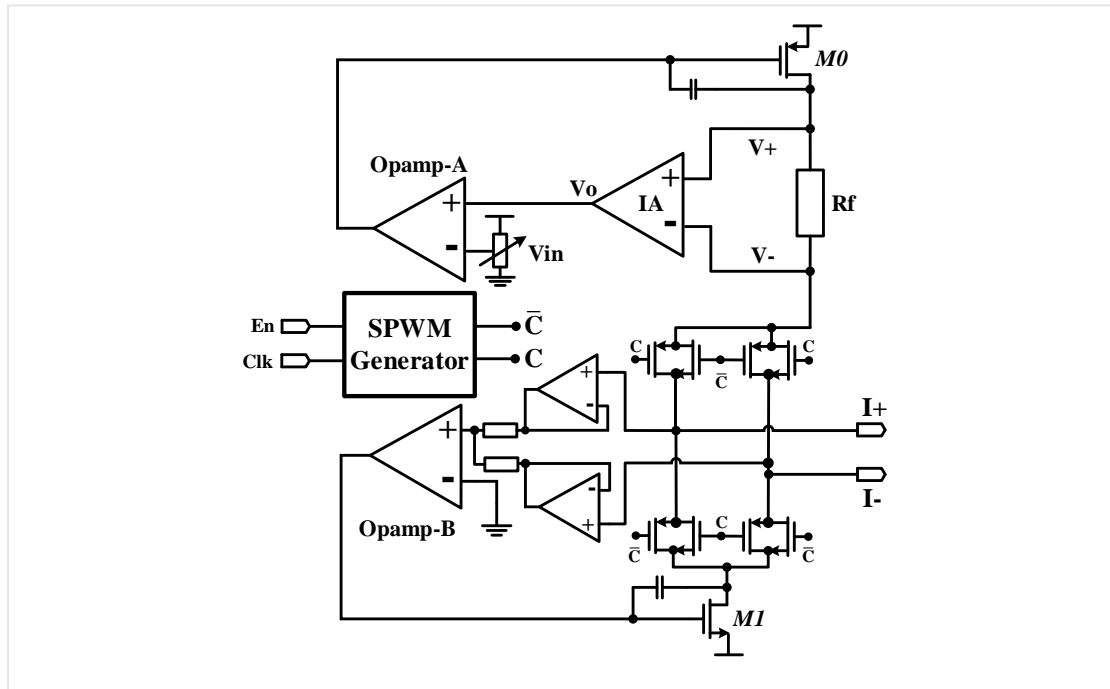


Figure 6.2: Circuit implementation of the proposed current generator.

The voltages across the load are measured by the buffer and summed into opamp-B for CMFB. When opamp-B achieves the ‘virtual short’, the CM voltage is effectively zero, hence the source and sink currents are made equal. The sizing of the output transistors M0 and M1 are chosen so that the desired maximum output current can be achieved within the maximum output voltage range of opamps A and B. In addition, the sizing should be optimized to ensure a small V_{ov} to maximize voltage compliance.

The feedback resistor R_f is set to $100\ \Omega$; the transconductance is $1\ \text{mA/V}$ providing a maximum $1\ \text{mA}$ output. The required maximum positive input linear range of the IA, which is defined as $I_{\text{bias}} \times R_1$, is $100\ \text{mV}$ and is achieved by setting $I_{\text{bias}} = 2\ \mu\text{A}$ and $R_1 = 50\ \text{k}\Omega$. The gain of the IA is set to 10 to minimize the error due to the input offset from opamp-A for small current outputs.

For feedback loop stability, opamps-A and B in Figure 6.2 are constructed using single-stage symmetrical OTA. The output transistors M0 and M1 are seen as the second stage which can be Miller compensated to improve loop stability (see Figure 6.2). To provide the full voltage compliance, the buffers at the inputs of opamp-B require rail-to-rail swings. The source and sink currents are connected to the load through the H-bridge controlled by a sine pulse width modulation (SPWM) generator [109].

Spectral purity of the SPWM output has been modelled in Matlab (R2014a, Mathworks). Its spectrum is shown in Figure 6.3 and is compared with spectra of a $98\ \text{kHz}$ pseudo-sinewave generated from a 4-bit DAC at 64 samples per cycle, and a $98\ \text{kHz}$ 50% duty-cycle square wave. As shown the injecting current contains harmonic noise in the high frequency band. Applying a second-order $300\ \text{kHz}$ low-pass filter at the measuring end, e.g. after the recording IA, to all three types of waveform, the high frequency harmonics can be suppressed.

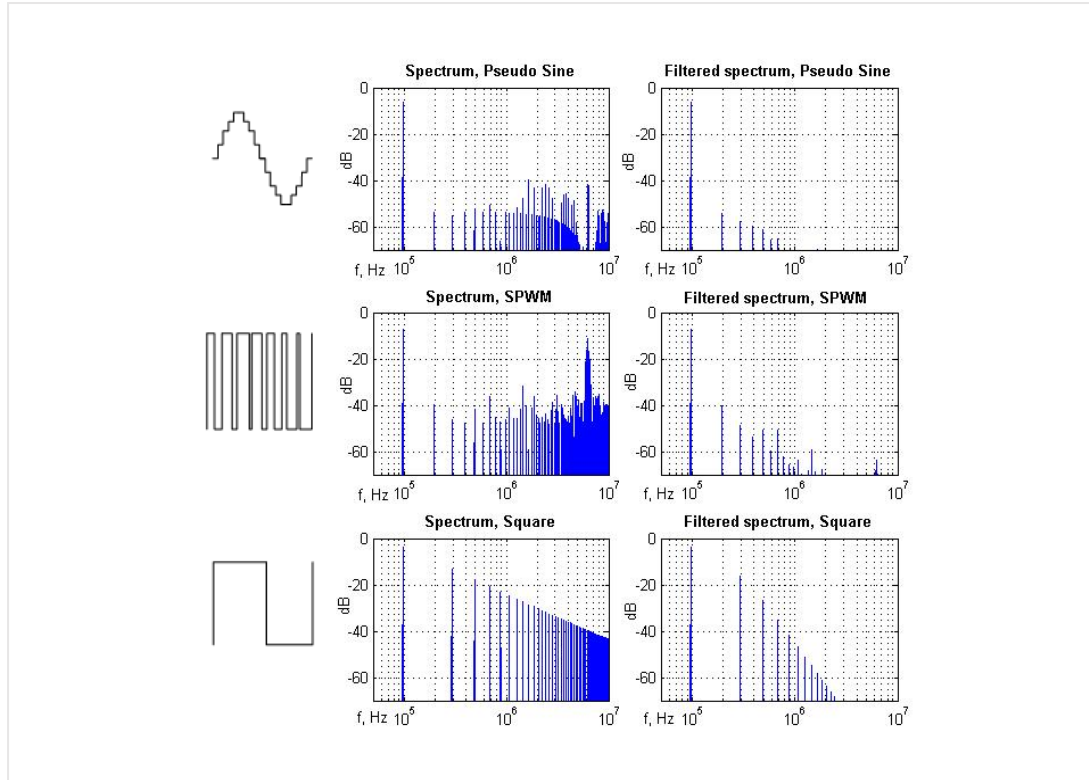


Figure 6.3: Spectra of 98 kHz pseudo sinewave (upper row), SPWM wave (middle row) and 50% duty cycle square wave (lower row), and their respective spectra after a 300 kHz second-order lowpass Butterworth filter.

The spurious-free dynamic range (SFDR) of the SPWM after filtering is 33.1 dB, compared to 48.2 dB for the pseudo-sine and 12.3 dB for the 50% duty cycle square wave. These results suggest that the SPWM achieves a good trade-off between signal quality and circuit simplicity. Compared with the pseudo-sine solution that has been widely used in EIT designs, SPWM provides acceptable SFDR with the advantage of eliminating the need of one or more multi-bit DAC implementations. The SPWM provides significantly better SFDR than the square wave, which is also used in bio-impedance measurement systems [108], [110].

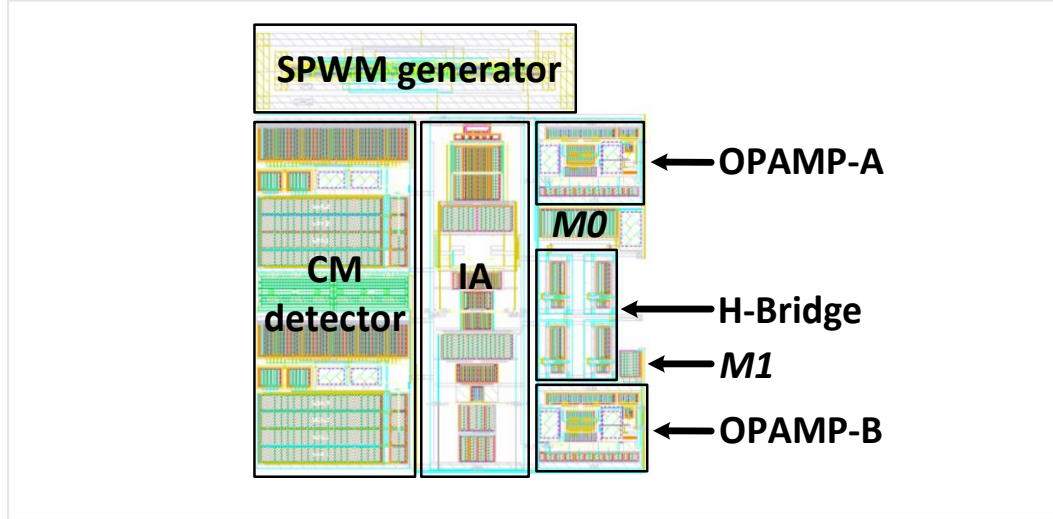


Figure 6.4: Layout of the current generator.

6.2.1.3 Simulation results

The current generator has been designed in a 0.18- μm CMOS process and operates from $\pm 1.65\text{ V}$ power supplies. The IA consumes $16\text{ }\mu\text{A}$ while other opamps consume $1\text{ }\mu\text{A}$ each to give a total current consumption of $I_{\text{out}} + 22\text{ }\mu\text{A}$, where I_{out} ranges from $50\text{ }\mu\text{A}$ to 1 mA . The digital circuit consumes $154\text{ }\mu\text{W}$ using a 1.8 V supply with $f_{\text{CLK}} = 50\text{ MHz}$, outputting a SPWM current at 98 kHz with 64 samples and 3 bits resolution.

The current generator has a maximum voltage compliance of $\pm 1.25\text{ V}$ that is limited to $V_{cc} - V_{ovM0} - V_{switch_{ds}} - I_{\text{out}} \times R_f$. For $I_{\text{out}} = 50\text{ }\mu\text{A}$, the current generator can drive a maximum load of up to $50\text{ k}\Omega$. At maximum current output, it can drive $2.4\text{ k}\Omega$.

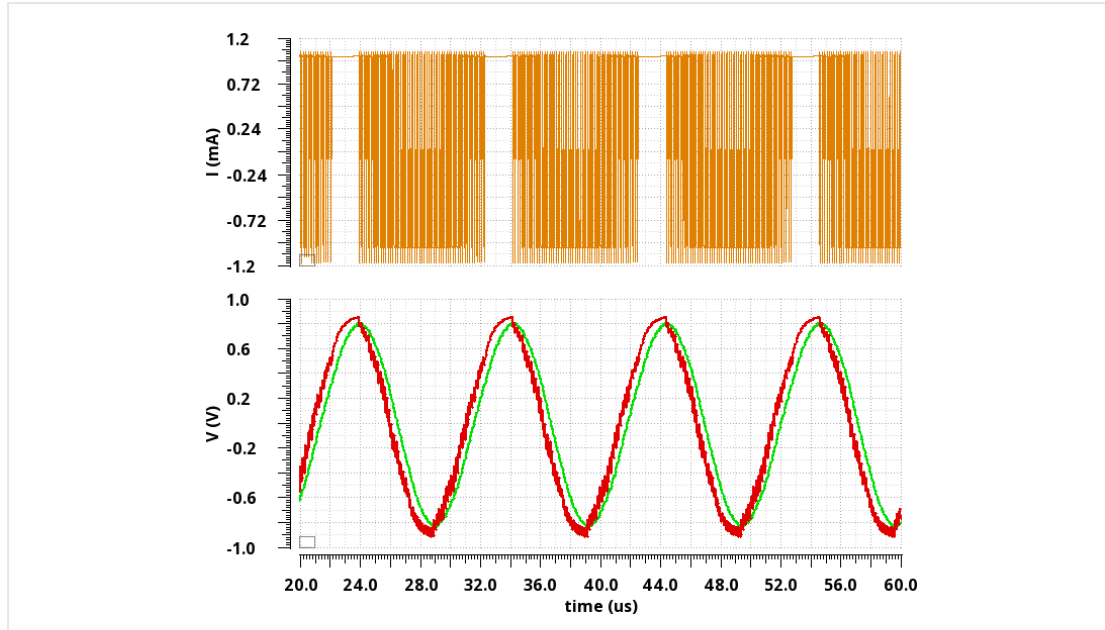


Figure 6.5: The PWM sine current output and voltage across a resistive load further filtered by a first-order (red) and second-order (green) low-pass filters.

Figure 6.4 shows the layout of the current generator; it occupies $350 \mu\text{m} \times 320 \mu\text{m}$. Compared with the DAC type current generator, the layout of the proposed current generator is less sensitive to mismatches. At 98 kHz, the post-layout simulation SPWM current output waveform is shown in Figure 6.5, alongside the voltage measured across a resistive load, after being further filtered by first- or second-order low-pass filters with a cut-off frequency at 300 kHz.

6.2.2 Concept on novel demodulation approaches using time-stamps

Conventional bio-impedance measurement uses magnitude and phase demodulation methods such as peak/phase detection, and coherence detection (I-Q demodulation). These require complex circuitry such as analog multiplier, peak & phase-detectors and analog to digital convertors.

The proposed method employs a novel time-stamp based magnitude and phase demodulation method as shown in Figure 6.6. On the left of Figure 6.6 shows a typical

4-electrode bio-impedance measurement. When an excitation signal V_{ref} is converted to current and injected into bio-tissue, a voltage V_m can then be measured by an IA using another pair of electrode. The measured voltage V_m has the same frequency as the original V_{ref} , but will be different in terms of signal amplitude and phase delay compared to the V_{ref} . The time-stamp demodulation method uses low power, fast-response comparator to check the zero crossing point of V_m , and V_{ref} . Once signals cross zero, a pulse is generated. T1 is when V_{ref} crosses zero and T2 when V_m crosses zero.

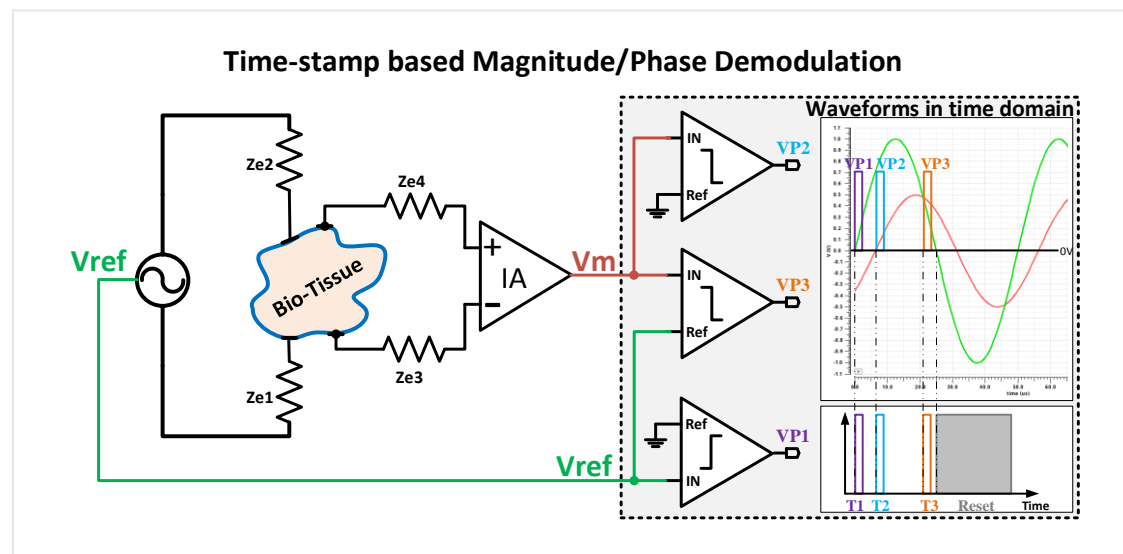


Figure 6.6: Time stamp demodulation method concept.

The time difference between T1 and T2 indicates the phase delays of the two signals. The phase between V_{ref} and V_m is measured by T1 and T2 using:

$$\theta = \frac{T_2 - T_1}{\frac{1}{f}} \times 2\pi \quad (6.2)$$

A third comparator is used to generate a pulse T3 when V_m crosses V_{ref} . As the amplitude of V_{ref} is always known, it is possible to calculate the amplitude level of V_m using time-stamp T3, T2 and T1 in a later signal processing stage.

First calculate voltage level at T3, using equation:

$$V_{at\ T3} = A_{Vref} \times \sin[2 \times \pi \times f \times (T_3 - T_1)] \quad (6.3)$$

where A_{Vref} is the know amplitude of V_{ref} and f is the excitation frequency.

With voltage at T3 known, the unknown amplitude of V_m can be then derived by using equation:

$$V_{at\ T3} = A_{Vm} \times \sin[2 \times \pi \times f \times (T_3 - T_2)] \quad (6.4)$$

Once the sinewave goes to negative polarity, a reset pulse will be generated.

Some system calibration is needed to take account of the system delays added the time-stamp pulse. To improve the accuracy of the system, averaging can also be used to average the read-out from a number of cycles.

Bibliography

- [1] B. H. Brown, D. C. Barber, and A. D. Seagar, "Applied potential tomography: Possible clinical applications," *Clin. Phys. Physiol. Meas.*, vol. 6, no. 2, pp. 109–121, 1985.
- [2] T. J. C. Faes, H. A. Van Der Meij, J. C. De Munck, and R. M. Heethaar, "The electric resistivity of human tissues (100 HZ-10 MHZ): A meta- analysis of review studies," *Physiological Measurement*, vol. 20, no. 4. 1999.
- [3] A. Adler *et al.*, "Whither lung EIT: Where are we, where do we want to go and what do we need to get there?," *Physiol. Meas.*, vol. 33, no. 5, pp. 679–694, 2012.
- [4] WHO, "Preterm birth," 2018. [Online]. Available: <https://www.who.int/news-room/fact-sheets/detail/preterm-birth>.
- [5] A. Hilgendorff, I. Reiss, H. Ehrhardt, O. Eickelberg, and C. M. Alvira, "Chronic lung disease in the preterm infant: Lessons learned from animal models," *American Journal of Respiratory Cell and Molecular Biology*. 2014.
- [6] J. Fawke *et al.*, "Lung function and respiratory symptoms at 11 years in children born extremely preterm: The EPICure study," *Am. J. Respir. Crit. Care Med.*, vol. 182, no. 2, pp. 237–245, 2010.
- [7] I. Frerichs *et al.*, "Chest electrical impedance tomography examination, data analysis, terminology, clinical use and recommendations: Consensus statement of the TRanslational EIT developmeNt stuDy group," *Thorax*, vol. 72, no. 1. pp. 83–93, 2017.
- [8] I. Frerichs *et al.*, "ONLINE SUPPLEMENT 8: Clinical use of EIT in neonatal and pediatric patients," *Thorax*, 2017.
- [9] A. Adler, B. Grychtol, and R. Bayford, "Why is EIT so hard, and what are we doing about it?," *Physiol. Meas.*, 2015.
- [10] A. McEwan, G. Cusick, and D. S. Holder, "A review of errors in multi-frequency EIT instrumentation," in *Physiological Measurement*, 2007, vol. 28, no. 7.
- [11] D. Djajaputra, "Electrical Impedance Tomography: Methods, History and Applications," *Med. Phys.*, 2005.
- [12] E. L. V Costa, R. G. Lima, and M. B. P. Amato, "Electrical impedance tomography," in *Yearbook of Intensive Care and Emergency Medicine*, Springer, 2009, pp. 394–404.
- [13] Swisstom, "Swisstom BB2 Product Information," *Rev.004*, 2013. [Online]. Available: http://www.swisstom.com/en/products/swisstom-bb2_en. [Accessed: 15-Apr-2019].

- [14] H. Wrigge *et al.*, "Electrical impedance tomography compared with thoracic computed tomography during a slow inflation maneuver in experimental models of lung injury," *Crit. Care Med.*, 2008.
- [15] J. M. Deibele, H. Luepschen, and S. Leonhardt, "Dynamic separation of pulmonary and cardiac changes in electrical impedance tomography," *Physiol. Meas.*, 2008.
- [16] H. Liu and L. Wang, "Gesture recognition for human-robot collaboration: A review," *Int. J. Ind. Ergon.*, no. ISSN 0169-8141, 2017.
- [17] S. S. Rautaray and A. Agrawal, "Vision based hand gesture recognition for human computer interaction: a survey," *Artif. Intell. Rev.*, vol. 43, no. 1, pp. 1–54, 2012.
- [18] P. Molchanov, S. Gupta, K. Kim, and K. Pulli, "Multi-sensor system for driver's hand-gesture recognition," in *2015 11th IEEE International Conference and Workshops on Automatic Face and Gesture Recognition, FG 2015*, 2015.
- [19] X. Li, R. Wen, Z. Shen, Z. Wang, K. D. K. Luk, and Y. Hu, "A Wearable Detector for Simultaneous Finger Joint Motion Measurement," *IEEE Trans. Biomed. Circuits Syst.*, vol. 12, no. 3, pp. 644–654, 2018.
- [20] T. Labs, "Myo- An wearable gesture control and motion control device," 2018. .
- [21] A. Fougner, O. Stavdahl, P. J. Kyberd, Y. G. Losier, and P. A. Parker, "Control of upper limb prostheses: Terminology and proportional myoelectric control a review," *IEEE Trans. Neural Syst. Rehabil. Eng.*, vol. 20, no. 5, pp. 663–677, 2012.
- [22] Y. Zhang and C. Harrison, "Tomo," in *Proceedings of the 28th Annual ACM Symposium on User Interface Software & Technology - UIST '15*, 2015, pp. 167–173.
- [23] Y. Zhang, R. Xiao, and C. Harrison, "Advancing Hand Gesture Recognition with High Resolution Electrical Impedance Tomography," in *Proceedings of the 29th Annual Symposium on User Interface Software and Technology - UIST '16*, 2017, pp. 843–850.
- [24] S. Russo, S. Nefti-Meziani, N. Carbonaro, and A. Tognetti, "A quantitative evaluation of drive pattern selection for optimizing EIT-based stretchable sensors," *Sensors (Switzerland)*, 2017.
- [25] W. R. B. Lionheart, "EIT reconstruction algorithms: Pitfalls, challenges and recent developments," in *Physiological Measurement*, 2004.
- [26] B. Sun, S. Yue, Z. Cui, and H. Wang, "A new linear back projection algorithm to electrical tomography based on measuring data decomposition," *Meas. Sci. Technol.*, 2015.
- [27] EIDORS, "EIDORS: Electrical Impedance Tomography and Diffuse Optical Tomography Reconstruction Software." [Online]. Available: <http://eidors3d.sourceforge.net/>. [Accessed: 03-Jul-2018].
- [28] Y. Zou and Z. Guo, "A review of electrical impedance techniques for breast cancer detection," *Medical Engineering and Physics*. 2003.

- [29] P. Åberg, I. Nicander, J. Hansson, P. Geladi, U. Holmgren, and S. Ollmar, "Skin cancer identification using multifrequency electrical impedance - A potential screening tool," *IEEE Trans. Biomed. Eng.*, 2004.
- [30] Y. A. Bhagat, I. Kim, A. Choi, J. Younghyun Kim, S. Jo, and J. Cho, "Mind Your Composition: Clinical validation of Samsung's pocket-based bioelectrical impedance analyzers may increase consumer interest in personal health management.," *IEEE Pulse*, 2015.
- [31] T. K. Bera, "Bioelectrical impedance methods for noninvasive health monitoring: A review," *Journal of Medical Engineering*. 2014.
- [32] M. F. A. Montagu and J. Brožek, *A handbook of anthropometry*. 2010.
- [33] S. Gabriel, R. W. Lau, and C. Gabriel, "The dielectric properties of biological tissues: II. Measurements in the frequency range 10 Hz to 20 GHz," *Phys. Med. Biol.*, 1996.
- [34] H. P. Schwan, "Electrical properties of tissues and cell suspensions: mechanisms and models," in *Proceedings of 16th Annual International Conference of the IEEE Engineering in Medicine and Biology Society*, 1994, vol. 1, p. A70–A71 vol.1.
- [35] H. Lee *et al.*, *In Vitro Evaluation of Finger's Hemodynamics For Vein Graft Surveillance Using Electrical Bio-Impedance Method*, vol. 8. 2014.
- [36] D. R. Merrill, M. Bikson, and J. G. R. Jefferys, "Electrical stimulation of excitable tissue: Design of efficacious and safe protocols," *Journal of Neuroscience Methods*. 2005.
- [37] N. Meziane, J. G. Webster, M. Attari, and A. J. Nimunkar, "Dry electrodes for electrocardiography," *Physiol. Meas.*, 2013.
- [38] M. Rahal, J. M. Khor, A. Demosthenous, A. Tizzard, and R. Bayford, "A comparison study of electrodes for neonate electrical impedance tomography," *Physiol. Meas.*, 2009.
- [39] V. Chitturi and N. Farrukh, "Spatial resolution in electrical impedance tomography: A topical review," *J Electr Bioimp*, 2017.
- [40] D. Djajaputra, "Electrical Impedance Tomography: Methods, History and Applications," *Med. Phys.*, 2005.
- [41] E. Huigen, A. Peper, and C. A. Grimbergen, "Investigation into the origin of the noise of surface electrodes," *Med. Biol. Eng. Comput.*, 2002.
- [42] M. M. Puurtinen, S. M. Komulainen, P. K. Kauppinen, J. A. V. Malmivuo, and J. A. K. Hyttinen, "Measurement of noise and impedance of dry and wet textile electrodes, and textile electrodes with hydrogel," in *Annual International Conference of the IEEE Engineering in Medicine and Biology - Proceedings*, 2006.
- [43] T. I. Oh *et al.*, "Nanofiber web textile dry electrodes for long-term biopotential recording," *IEEE Trans. Biomed. Circuits Syst.*, 2013.
- [44] R. Hölzel, "A Simple Wideband Sine Wave Quadrature Oscillator," *IEEE Trans. Instrum. Meas.*, 1993.

- [45] M. Takhti and K. Odame, "Structured Design Methodology to Achieve a High SNR Electrical Impedance Tomography," *IEEE Transactions on Biomedical Circuits and Systems*, vol. 13, no. 2, pp. 364–375, 2019.
- [46] I. E. Commission, "IEC60601-1, Safety and essential performance of medical electrical equipment." [Online]. Available: https://en.wikipedia.org/wiki/IEC_60601.
- [47] B. H. Brown, *Biological and Medical Physics , Biomedical Engineering*. 1999.
- [48] N. Neshatvar, P. Langlois, R. Bayford, and A. Demosthenous, "Analog integrated current drivers for bioimpedance applications: A review," *Sensors (Switzerland)*. 2019.
- [49] L. Constantinou, I. F. Triantis, R. Bayford, and A. Demosthenous, "High-power CMOS current driver with accurate transconductance for electrical impedance tomography," *IEEE Trans. Biomed. Circuits Syst.*, 2014.
- [50] Swsstom.AG, "ResistorPhantomManual 1ST504-103," Rev 000, 2013. [Online]. Available: http://www.swisstom.com/software/PDF/ResistorPhantomManual_1ST504-103_Rev_000.pdf. [Accessed: 03-May-2019].
- [51] H. Gagnon, M. Cousineau, A. Adler, and A. E. Hartinger, "A resistive mesh phantom for assessing the performance of EIT systems," *IEEE Trans. Biomed. Eng.*, vol. 57, no. 9, pp. 2257–2266, 2010.
- [52] G. Hahn, M. Beer, I. Frerichs, T. Dudykevych, T. Schröder, and G. Hellige, "A simple method to check the dynamic performance of electrical impedance tomography systems," *Physiol. Meas.*, 2000.
- [53] R. Pallás-Areny and J. G. Webster, "AC Instrumentation Amplifier for Bioimpedance Measurements," *IEEE Trans. Biomed. Eng.*, 1993.
- [54] J. Rosell and P. Riu, "Common-mode Feedback in Electrical Impedance Tomography," *Clin. Phys. Physiol. Meas.*, vol. 13, pp. 11–14, 1992.
- [55] P. J. Langlois, Y. Wu, R. H. Bayford, and A. Demosthenous, "On the application of frequency selective common mode feedback for multifrequency EIT," in *Physiological Measurement*, 2015, vol. 36, no. 6, pp. 1337–1350.
- [56] S. Grimnes and Ø. G. Martinsen, *Bioimpedance and Bioelectricity Basics*. 2008.
- [57] R. J. Yerworth, R. H. Bayford, B. Brown, P. Milnes, M. Conway, and D. S. Holder, "Electrical impedance tomography spectroscopy (EITS) for human head imaging," in *Physiological Measurement*, 2003.
- [58] T. I. Oh, E. J. Woo, and D. Holder, "Multi-frequency EIT system with radially symmetric architecture: KHU Mark1," in *Physiological Measurement*, 2007.
- [59] A. Worapishet, A. Demosthenous, and X. Liu, "A CMOS instrumentation amplifier with 90-db CMRR at 2-MHz using capacitive neutralization: Analysis, design considerations, and implementation," *IEEE Trans. Circuits Syst. I Regul. Pap.*, vol. 58, no. 4, pp. 699–710, 2011.
- [60] M. Takhti, Y. C. Teng, and K. Odame, "A 10 MHz Read-Out Chain for Electrical Impedance Tomography," *IEEE Trans. Biomed. Circuits Syst.*, vol. 12, no. 1, pp.

- 222–230, 2018.
- [61] R. Pallás-Areny and J. G. Webster, “Common Mode Rejection Ratio for Cascaded Differential Amplifier Stages,” *IEEE Transactions on Instrumentation and Measurement*. 1991.
 - [62] A. C. MettingVanRijn, A. P. Kuiper, T. E. Dankers, and C. A. Grimbergen, “Low-cost active electrode improves the resolution in biopotential recordings,” in *Proceedings of 18th Annual International Conference of the IEEE Engineering in Medicine and Biology Society*, 1996, vol. 1, pp. 101–102 vol.1.
 - [63] J. Xu, S. Mitra, C. Van Hoof, R. F. Yazicioglu, and K. A. A. Makinwa, “Active Electrodes for Wearable EEG Acquisition: Review and Electronics Design Methodology,” *IEEE Reviews in Biomedical Engineering*, vol. 10. pp. 187–198, 2017.
 - [64] J. H. Li, C. Joppek, and U. Faust, “In vivo EIT electrode system with 32 interlaced active electrodes,” *Med. Biol. Eng. Comput.*, 1996.
 - [65] B. Rigaud, Y. Shi, N. Chauveau, and J. P. Morucci, “Experimental acquisition system for impedance tomography with active electrode approach,” *Med. Biol. Eng. Comput.*, vol. 31, no. 6, pp. 593–599, 1993.
 - [66] J. H. Li, C. Joppek, and U. Faust, “Fast EIT data acquisition system with active electrodes and its application to cardiac imaging,” in *Physiological Measurement*, 1996, vol. 17, no. 4 SUPPL. A.
 - [67] P. O. Gaggero, A. Adler, J. Brunner, and P. Seitz, “Electrical impedance tomography system based on active electrodes,” *Physiol. Meas.*, vol. 33, no. 5, pp. 831–847, 2012.
 - [68] J. M. Khor, A. Tizzard, A. Demosthenous, and R. Bayford, “Wearable sensors for patient-specific boundary shape estimation to improve the forward model for electrical impedance tomography (EIT) of neonatal lung function,” *Physiol. Meas.*, vol. 35, no. 6, pp. 1149–1161, 2014.
 - [69] S. De Gelidi *et al.*, “Torso shape detection to improve lung monitoring,” *Physiol. Meas.*, 2018.
 - [70] T. I. Oh, H. Wi, D. Y. Kim, P. J. Yoo, and E. J. Woo, “A fully parallel multi-frequency EIT system with flexible electrode configuration: KHU Mark2,” in *Physiological Measurement*, 2011.
 - [71] R. A. Pease, “AN-1515 A Comprehensive Study of the Howland Current Pump,” *Texas Instruments*, 2013.
 - [72] A. Mahnam, H. Yazdanian, and M. Mosayebi Samani, “Comprehensive study of Howland circuit with non-ideal components to design high performance current pumps,” *Meas. J. Int. Meas. Confed.*, 2016.
 - [73] T. I. Oh, K. H. Lee, S. M. Kim, H. Koo, E. J. Woo, and D. Holder, “Calibration methods for a multi-channel multi-frequency EIT system,” *Physiol. Meas.*, vol. 28, no. 10, pp. 1175–88, 2007.
 - [74] Dräger, “Product brochure: PulmoVista 500,” 2011. [Online]. Available: https://www.draeger.com/en_aunz/Hospital/EIT-Lung-Monitoring. [Accessed:

- 03-Apr-2018].
- [75] H. Hong, M. Rahal, A. Demosthenous, and R. H. Bayford, "Comparison of a new integrated current source with the modified howland circuit for EIT applications," *Physiol. Meas.*, vol. 30, no. 10, pp. 999–1007, 2009.
 - [76] S. Heinrich, H. Schiffmann, A. Frerichs, A. Klockgether-Radke, and I. Frerichs, "Body and head position effects on regional lung ventilation in infants: An electrical impedance tomography study," *Intensive Care Med.*, 2006.
 - [77] A. J. Wilson, P. Milnes, A. R. Waterworth, R. H. Smallwood, and B. H. Brown, "Mk3.5: A modular, multi-frequency successor to the Mk3a EIS/EIT system," in *Physiological Measurement*, 2001, vol. 22, no. 1, pp. 49–54.
 - [78] A. McEwan, A. Romsauerova, R. Yerworth, L. Horesh, R. Bayford, and D. Holder, "Design and calibration of a compact multi-frequency EIT system for acute stroke imaging," in *Physiological Measurement*, 2006.
 - [79] S. Hong, J. Lee, J. Bae, and H. J. Yoo, "A 10.4 mW Electrical Impedance Tomography SoC for Portable Real-Time Lung Ventilation Monitoring System," *IEEE J. Solid-State Circuits*, vol. 50, no. 11, pp. 2501–2512, 2015.
 - [80] M. H. Lee *et al.*, "Portable multi-parameter electrical impedance tomography for sleep apnea and hypoventilation monitoring: Feasibility study," *Physiol. Meas.*, vol. 39, no. 12, p. 124004, 2018.
 - [81] M. Rapin *et al.*, "Wearable Sensors for Frequency-Multiplexed EIT and Multilead ECG Data Acquisition," *IEEE Trans. Biomed. Eng.*, vol. 66, no. 3, pp. 810–820, 2019.
 - [82] S. A. Santos, A. Robens, A. Boehm, S. Leonhardt, and D. Teichmann, "System description and first application of an FPGA-based simultaneous multi-frequency electrical impedance tomography," *Sensors (Switzerland)*, 2016.
 - [83] A. D. Waldmann *et al.*, "Performance of Novel Patient Interface for Electrical Impedance Tomography Applications," *J. Med. Biol. Eng.*, vol. 37, no. 4, pp. 561–566, 2017.
 - [84] E. Sánchez-Sinencio and J. Silva-Martínez, "CMOS transconductance amplifiers, architectures and active filters: a tutorial," *IEE Proc. - Circuits, Devices Syst.*, vol. 147, no. 1, p. 3, 2002.
 - [85] T. P. D. R. Design, "Noise Measurement Post Amp - Texas Instruments," 2013. [Online]. Available: <http://www.ti.com/lit/ug/tidu016/tidu016.pdf>. [Accessed: 11-Jul-2019].
 - [86] M. Kim *et al.*, "A 1.4-m Ω -Sensitivity 94-dB Dynamic-Range Electrical Impedance Tomography SoC and 48-Channel Hub-SoC for 3-D Lung Ventilation Monitoring System," *IEEE J. Solid-State Circuits*, vol. 52, no. 11, pp. 2829–2842, 2017.
 - [87] A. Adler, P. O. Gaggero, and Y. Maimaitijiang, "Adjacent stimulation and measurement patterns considered harmful," in *Physiological Measurement*, 2011, vol. 32, no. 7, pp. 731–744.
 - [88] S. De Gelidi, A. Bardill, Y. Wu, A. Demosthenous, A. Tizzard, and R. Bayford,

- “Torso shape detection to improve lung monitoring,” in *18th International Conference on Biomedical Applications of Electrical Impedance Tomography*, 2017.
- [89] G. Huang, Z. Zhang, D. Zhang, and X. Zhu, “Spatio-spectral filters for low-density surface electromyographic signal classification,” *Med. Biol. Eng. Comput.*, vol. 51, no. 5, pp. 547–555, 2013.
 - [90] C. Cipriani *et al.*, “Online myoelectric control of a dexterous hand prosthesis by transradial amputees,” *IEEE Trans. Neural Syst. Rehabil. Eng.*, vol. 19, no. 3, pp. 260–270, 2011.
 - [91] P. Geethanjali and K. K. Ray, “A Low-Cost Real-Time Research Platform for EMG Pattern Recognition-Based Prosthetic Hand,” *IEEE/ASME Trans. Mechatronics*, vol. 20, no. 4, pp. 1948–1955, 2015.
 - [92] S. L. Teng, R. Rieger, and Y. Bin Lin, “Programmable ExG biopotential front-end IC for wearable applications,” *IEEE Trans. Biomed. Circuits Syst.*, vol. 8, no. 4, pp. 543–551, 2014.
 - [93] S. Benatti *et al.*, “A Versatile Embedded Platform for EMG Acquisition and Gesture Recognition,” *IEEE Trans. Biomed. Circuits Syst.*, vol. 9, no. 5, pp. 620–630, 2015.
 - [94] A. Andrews, E. Morin, and L. McLean, “Optimal electrode configurations for finger movement classification using EMG,” in *Proceedings of the 31st Annual International Conference of the IEEE Engineering in Medicine and Biology Society: Engineering the Future of Biomedicine, EMBC 2009*, 2009, pp. 2987–2990.
 - [95] G. Li, Y. Geng, D. Tao, and P. Zhou, “Performance of electromyography recorded using textile electrodes in classifying arm movements,” in *Proceedings of the Annual International Conference of the IEEE Engineering in Medicine and Biology Society, EMBS*, 2011, pp. 4243–4246.
 - [96] M. a. Oskoei and H. H. H. Hu, “Support Vector Machine-Based Classification Scheme for Myoelectric Control Applied to Upper Limb,” *IEEE Trans. Biomed. Eng.*, vol. 55, no. 8, pp. 1956–1965, 2008.
 - [97] M. Atzori, M. Cognolato, and H. Müller, “Deep learning with convolutional neural networks applied to electromyography data: A resource for the classification of movements for prosthetic hands,” *Front. Neurobot.*, vol. 10, no. SEP, 2016.
 - [98] A. M. Simon, K. Stern, and L. J. Hargrove, “A comparison of proportional control methods for pattern recognition control,” in *Proceedings of the Annual International Conference of the IEEE Engineering in Medicine and Biology Society, EMBS*, 2011, pp. 3354–3357.
 - [99] C. Castellini and P. Van Der Smagt, “Surface EMG in advanced hand prosthetics,” *Biol. Cybern.*, vol. 100, no. 1, pp. 35–47, 2009.
 - [100] P. F. Pasquina *et al.*, “First-in-man demonstration of a fully implanted myoelectric sensors system to control an advanced electromechanical prosthetic hand,” *J. Neurosci. Methods*, vol. 244, pp. 85–93, 2015.

- [101] J. He, D. Zhang, N. Jiang, X. Sheng, D. Farina, and X. Zhu, "User adaptation in long-term, open-loop myoelectric training: Implications for EMG pattern recognition in prosthesis control," *J. Neural Eng.*, vol. 12, no. 4, 2015.
- [102] J. W. Sensinger, B. A. Lock, and T. A. Kuiken, "Adaptive pattern recognition of myoelectric signals: Exploration of conceptual framework and practical algorithms," *IEEE Trans. Neural Syst. Rehabil. Eng.*, 2009.
- [103] M. A. Powell, R. R. Kaliki, and N. V. Thakor, "User training for pattern recognition-based myoelectric prostheses: Improving phantom limb movement consistency and distinguishability," *IEEE Trans. Neural Syst. Rehabil. Eng.*, 2014.
- [104] J. Malmivuo and R. Plonsey, *Bioelectromagnetism - Principles and Applications of Bioelectric and Biomagnetic Fields, Chapter: 26*. Oxford University Press, 1995.
- [105] B. Grychtol, B. Müller, and A. Adler, "3D EIT image reconstruction with GREIT," *Physiol. Meas.*, 2016.
- [106] L. M., G. W., B. N., E. M., H. E., and F. H., "Does use of a myoelectric prosthesis prevent cortical reorganization and phantom limb pain?," *Nat. Neurosci.*, 1999.
- [107] L. Yan *et al.*, "A 13 μ a analog signal processing IC for accurate recognition of multiple intra-cardiac signals," *IEEE Trans. Biomed. Circuits Syst.*, 2013.
- [108] J. Xu *et al.*, "A 36 \times W 1.1 mm² Reconfigurable Analog Front-End for Cardiovascular and Respiratory Signals Recording," *IEEE Transactions on Biomedical Circuits and Systems*, 2018.
- [109] Y. Wu, D. Jiang, P. Langlois, R. Bayford, and A. Demosthenous, "A Power-Efficient Current Generator with Common Mode Signal Autozero Feedback for Bioimpedance Measurement Applications," in *2019 IEEE International Symposium on Circuits and Systems (ISCAS)*, 2019, pp. 1–4.
- [110] M. Min and T. Parve, "Improvement of lock-in electrical bio-impedance analyzer for implantable medical devices," *IEEE Trans. Instrum. Meas.*, vol. 56, no. 3, pp. 968–974, 2007.
- [111] Y. Wu, D. Jiang, A. Bardill, S. De Gelidi, R. Bayford, and A. Demosthenous, "A high frame rate wearable EIT system using active electrode ASICs for lung respiration and heart rate monitoring," *IEEE Trans. Circuits Syst. I Regul. Pap.*, 2018.